FOURIER TRANSFORM INFRARED ABSORPTION SPECTROSCOPY AND KINETICS STUDIES OF GAS PHASE SMALL MOLECULES

LI SHUPING
(MSc.Chem, Xiamen Univ.)

A THESIS SUBMITTED

FOR THE DEGREE OF DOCTOR OF PHILOSOPHY

DEPARTMENT OF CHEMISTRY

NATIONAL UNIVERSITY OF SINGAPORE

2006

Acknowledgement

First of all I would like to take this opportunity to express my sincere and deep appreciation towards my supervisor, Dr Fan Wai Yip who gave me the much-needed help, advice and guidance. Thank you for your patience, effort as well as teaching me how to use good English during the course of my PhD.

I am grateful to my group members; Li Peng, Tan Yen Ling, Jason Yang Jiexiang, Tan Hua, Zhan Tong, Christian Lefföld, Lim Kok Peng, Lee Wei Te, Wong Lingkai, Toh Ee Chyi, Ng Choon Hwee,Bernard, Tan Sze Tat, Tang Hui Boon. Thank you for your help and support for these past few years.

I wish to thank Mr Conrado Wu of the Chemistry Department Glassblowing workshop for fabricating all the glassware equipment for my experiments; Mr Tan Choon Wah from Physics Department workshop and Mr Rajoo and Mr Guan from the Chemistry Department workshop for their technical support.

I also appreciate the support from Mr Teo Leong Kai, Mr Sim Hang Whatt and Mr Lee from the Chemistry Department Lab Supply room and Mdms Adeline Chia and Patricia Tan from the Physical Chemistry laboratory.

Lastly I wish to acknowledge the National University of Singapore for offering me the research scholarship and providing me the chance to pursue my degree here.

Table of Contents

Acknowledgement i

Table of Contents ii

Summary v

CHAPTER 1 Introduction 1

1.1 Gas phase kinetics 2

1.2 Reactions of O(^{3}P) atoms with CS_2 2

1.3 Photolysis of nitrite and atmospheric chemistry of alkoxy radicals 6

1.3.1 Photolysis of nitrite 6

1.3.2 Atmospheric chemistry of alkoxy radicals 9

1.4 Hydrogen atom abstraction reactions 15

1.4.1 General features of hydrogen abstractions 15

1.4.3 Abstraction reactions by t-butoxy radical 18

1.4.4 Reactions of Chlorine atoms (^{2}P $_{3/2}$) with hydrocarbons 21

1.5 Main Objectives 24

Reference 26

CHAPTER 2 O (^{3}P) atom reactions with CSe_2, SCSe and OCSe 32

2.1 Introduction 32

2.2 Experimental section 34

2.2.1 Synthesis of CSe_2 and SCSe 34

2.2.2 Experimental setup 35

2.3 Results 37

2.3.1 Concentration Analysis 37

2.3.2 Reactions of O (^{3}P) with CS_2 and OCS 40

2.3.3 Reactions of O (^{3}P) atoms with CX_1X_2 (X_1=Se, X_2=O, S or Se) 42

2.3.4 Reaction of CSe with O (^{3}P) and O_2 51

2.4 Discussion **54**

2.5 Computational studies **57**

2.6 Summary **66**

Reference **68**

CHAPTER 3 Laser-induced decomposition of fluoronitrites **70**

3.1 Introduction **70**

3.2 Experimental section **72**

3.2.1 Synthesis of nitrites 72

3.2.2 UV spectrum of CF_3CH_2ONO 73

3.2.3 FTIR setup 74

3.3 Photolysis of trifluoroethylnitrite **76**

3.3.1 IR band of CF_3CH_2ONO 76

3.3.2 Photolysis of CF_3CH_2ONO 77

3.3.3 Effect of NO 82

3.3.4 Photolysis of CF_3CD_2ONO 83

3.3.5 Computational work 85

3.3.6 Reaction of CF_3CH_2ONO with O_2 87

3.4 Photolysis of other fluoronitrites **91**

3.5 Conclusion **92**

Reference **94**

CHAPTER 4 Hydrogen atom abstraction kinetics by t-butoxy radical **96**

4.1 Introduction **96**

4.2 Experimental section **97**

4.3 Results and discussion **99**

4.3.1 Concentration Analysis 99

4.3.2 Reaction of t-butoxy radical with hydrogen donors 100

4.3.3 Computational work 106

4.4 Conclusion **109**

Reference **110**

CHAPTER 5 Reaction of O (^{3}P) and Cl ($^2P_{3/2}$) atoms with $CF_3CHOHCF_3$ and CF_3CH_2OH **112**

5.1 Introduction **112**

5.2 Experimental section **113**

5.3 Computational studies **115**

5.4 Results and discussion **115**

5.4.1 Relative rate studies 115

5.4.2. Stable product analysis 122

5.5 Conclusion **133**

Reference **143**

Summary

The work in this thesis is directed towards understanding the kinetics of elementary gas-phase reactions of small molecules using Fourier-Transformed Infrared (FTIR) absorption techniques. The small molecules investigated here are deemed to be important intermediates in atmospheric and combustion chemistry. Thus it is of relevance to understand the kinetics and reaction mechanism involving these molecules.

The literature review of all the reactions investigated here is presented in Chapter 1. In Chapter 2, the overall rate coefficients of the reactions of CSe_2, SCSe and OCSe with $O(^3P)$ atom have been determined to be $k_{CSe2} = (1.4 \pm 0.2) \times 10^{-10}$ cm^3 $molecule^{-1}$ s^{-1}, $k_{SCSe} = (2.8\pm 0.3) \times 10^{-11}$ cm^3 $molecule^{-1}$ s^{-1} and $k_{OCSe} = (2.4\pm 0.3) \times 10^{-11}$ cm^3 $molecule^{-1}$ s^{-1} at 301-303K using Fourier-Transformed Infrared (FTIR) absorption spectroscopy. The measurements have been accomplished by calibrating against the literature value of the rate coefficient for O (^3P) with CS_2 (4 x 10^{-12} cm^3 $molecule^{-1}$ s^{-1}). A product channel giving OCSe in (32.0 ± 4.2)% yield has been found for the O + CSe_2 reaction. The corresponding reaction for O + SCSe gives OCS and OCSe as observable products, with their yields determined to be (32.2 ± 4.5) and (30.2 ± 3.3) %, respectively. Computational studies using UB3LYP/aug-cc-PVTZ methods have been used particularly to determine the reaction pathways, transition state, intermediate for the channels from which OCS or OCSe is produced.

In Chapter 3, the unimolecular decomposition of alkoxy radicals, in particular the trifluoroethoxy CF_3CH_2O radical, generated from 355 nm pulsed nanosecond laser photolysis of its parent nitrite in the gas phase has been studied. The radical preferentially

dissociates via its C-H bond cleavage to yield CF_3CHO (trifluoroacetaldehyde) as the major product. The infrared spectrum of formaldehyde, one of the products of C-C bond dissociation of CF_3CH_2O was not observed under a range of nitrite and argon buffer gas pressures. Similar results were obtained when thermal heating and broadband xenon lamp irradiation of the nitrite were carried out. The addition of high pressures of NO further decreased the production of CF_3CHO since recombination of NO with the trifluoroethoxy radical competes with the unimolecular dissociation process. Surprisingly, CF_3CDO was also the only product observed when the deuterated species CF_3CD_2ONO was photolysed by the 355 nm laser. These observations contradicted MP2/aug-cc-pVTZ calculations which were found to favour the C-C bond dissociation channel. However, 355 nm photolysis of CF_3CH_2ONO in the presence of O_2 yielded trifluoroethylnitrate, $CF_3CH_2ONO_2$ as the main product while CF_3CHO and CF_2O were also observable at much lower yields.

In Chapter 4, the rate coefficients in the range of 10^{-16}-10^{-14} $cm^3molecule^{-1}s^{-1}$ have been determined for the hydrogen atom abstraction reactions by t-butoxy radical of several substrates in gas phase using FTIR Absorption Spectroscopy. The substrates include halogenated organic compounds and amines. Arrhenius parameters for selected reactions have been measured in the temperature range 299-318K. Transition states and activation barriers for such reactions have been computed. The abstraction reaction is believed to be elementary in nature.

In Chapter 5, the rate coefficients at 295±2K for the reactions of $O(^3P)$ atoms with $(CF_3)_2CHOH$ and CF_3CH_2OH have been determined to be $(5.6 \pm 0.4) \times 10^{-14}$ and $(6.6 \pm 0.5) \times 10^{-14}$ cm^3 $molecule^{-1}s^{-1}$while the rate coefficients for the reactions of $Cl(^2P_{3/2})$ with

the same fluoroalcohols, $(CF_3)_2CHOH$ and CF_3CH_2OH have been determined to be $(4.9 \pm 0.15) \times 10^{-13}$ and $(7.5 \pm 0.6) \times 10^{-13}$ cm^3 $molecule^{-1}s^{-1}$. Stable products formed during the reactions have been detected by Fourier-Transform Infrared (FTIR) Absorption Spectroscopy. The reaction of $Cl(^2P_{3/2})$ and CF_3CH_2OH has the most products; HCl, CF_3CClO, CF_3CHO, HClCO, CCl_2O and CO. We have also tentatively assigned some new IR bands to an important chloroalcohol intermediate, CF_3CCl_2OH. *Ab initio* calculations in Gaussian 03 have been extensively used to provide a better understanding of the various reaction pathways leading to the generation of the stable products in the $Cl(^2P_{3/2})$ and CF_3CH_2OH system.

– CHAPTER 1 –

Introduction

1.1 Gas phase kinetics

The study of elementary gas-phase reaction kinetics, a venerable area of chemical investigation, continues to play a prominent role in our understanding of fundamental chemistry and of large chemical systems [1-2]. High-precision laboratory measurements of gas-phase radical reactions are responsible for much of the kinetic data especially on combustion modeling [3] and atmospheric chemistry [4-5]. Optical inspection of change in concentration of reactants and products following pulsed photolytic initiation has become standard techniques in gas-phase radical reaction kinetics over the past several decades. Due to the vast number of studies conducted, we can only focus on some of the work which have been carried out for a few of these important gas phase kinetic systems. In later chapters, we will extend the work on these particular areas using either flash laser photolysis or broadband light irradiation for generation of the reactive species such as O or Cl atoms. Fourier-Transform Infrared (FTIR) absorption spectroscopy is then used for the detection and monitoring of the vibrational bands of both reactants and products.

1.2 Reactions of $O(^3P)$ atoms with CS_2

Reactions of oxygen atoms are very important in basic chemical kinetics and dynamics and are of relevance in practical applications in atmospheric and combustion chemistry [6]. In particular, the oxidation of naturally-occurring small sulfur-containing compounds by oxygen atoms can produce SO radicals that lead to SO_2 and ultimately yield acid rain in the atmosphere [7]. Oxygen atom reactions with sulfur compounds are also crucial in the combustion chemistry of sulfur-containing fuels [8].

Chapter 1 Introduction

Carbon disulfide is one of the most common sulfur-containing species and the reaction of oxygen (^3P) atom with carbon disulfide, CS_2 has received considerable attention for its role in atmospheric chemistry especially in the elucidation of global sulfur cycle leading to acid rain [7, 9]. The reaction kinetics is also of primary interest in the understanding of the CS_2 laser [10]. Three product channels have been observed for this reaction [11];

$$O\ (^3P) + CS_2 \rightarrow CS + SO\ (^3\Sigma^-) \qquad \Delta_fH° = -80.7\ kJ\ mol^{-1} \qquad 1(a)$$

$$\rightarrow CO + S_2\ (^3\Sigma^-_g) \qquad \Delta_fH° = -347.8\ kJ\ mol^{-1} \qquad 1(b)$$

$$\rightarrow OCS + S\ (^3P) \qquad \Delta_fH° = -227.4\ kJ\ mol^{-1} \qquad 1(c)$$

There are several determinations of the total rate coefficient of this reaction at 298K using a variety of techniques. Hsu *et al* studied the reaction of $O(^3P)$ with CS_2 at 298 K by means of a CO laser resonance absorption technique [12]. Figure 1.1 shows the total populations and rates determined for the two mixtures in which one of them contained C_2H_2 as reference. The measured ratio of the production rate of CO(υ) from the $O(^3P)$ with CS_2 versus the production rate of CO(υ) from the $O(^3P)$ with C_2H_2 reaction, based on the extrapolation as shown in the upper part of Figure 4 is 0.373±0.048. The rate constant for reaction 1(b) was detected to be $(5.8\pm 0.5) \times 10^{-14}$ cm^3 $molecule^{-1}$ s^{-1} and (1.4 ± 0.2) % of O + CS_2 reaction preceded via this channel. Based on this value, the overall rate constant of O + CS_2 was calculated to be $(4.2 \pm 0.2) \times 10^{-12}$ cm^3 $molecule^{-1}$ s^{-1}.

Gutman *et al* [13] studied the same reaction by employing molecular beams and the overall rate constant was obtained from first order decay of CS_2 since the O atom concentration was kept in large excess during the whole experiment. The average rate

constant was k= (4.0 ±0.3) × 10^{-12} cm^3 $molecule^{-1}$ s^{-1} at 302 ± 2 K. The branching ratio for route 1(c) was determined using the expression: $R_2 = k_2 / k = \Delta[OCS]_t / \Delta[CS_2]_t$ with the the linear relationship of $\Delta [OCS]_t$ vs $\Delta [CS_2]_t$ shown in Figure 1.3. From the slope, the branching ratio of 1(c) was determined to be 0.093 ± 0.008.

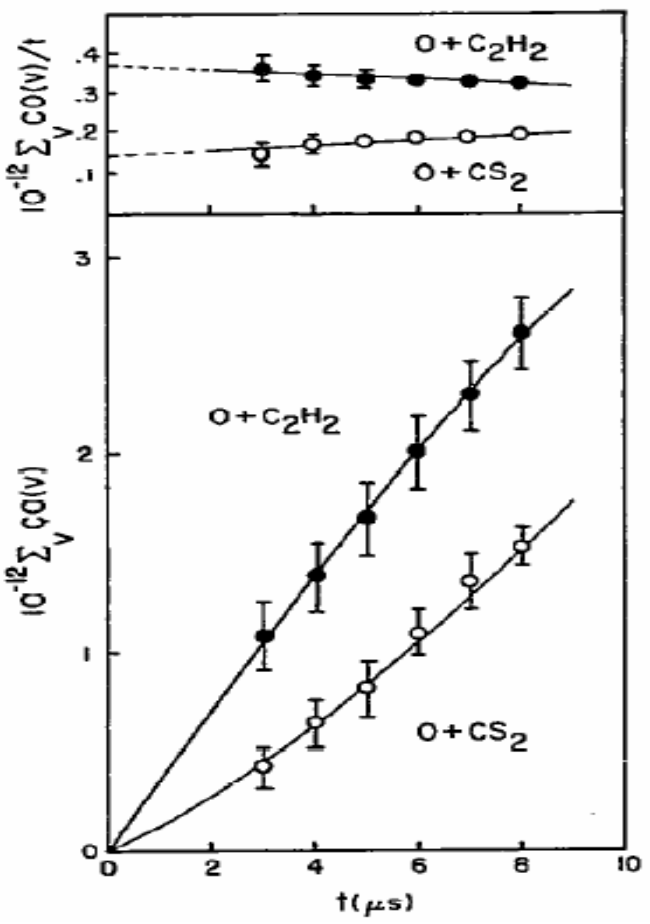

Figure 1.1 Absolute CO yields from the reaction of O(^{3}P) atoms with CS_2 and C_2H_2 under identical conditions

The initial evidence for channel 1(a) was the detection of CS and SO in a kinetic-flash-spectroscopy study of O + CS_2 reaction [14]. The most direct evidence for the existence of channel 1 was the detection of SO in a crossed-beam study of the reaction of O + CS_2 [15] with indications that reaction 1 is the dominant pathway. Cheng *et al.* has

studied the dynamics of the dominant channel 1(a) by examining the vibrational state distributions of CS ($X^1\Sigma^+$) and SO($X^3\Sigma^-$) using laser-induced fluorescence spectroscopy on the SO ($B^3\Sigma^-$ - $X^3\Sigma^-$) and CS ($A^1\Pi$- $X^1\Sigma^+$) (Figure 1.2)[16]. The resulting CS and SO vibrational state distributions have revealed rather high vibrational temperatures of 1230 and 1312 K respectively. Westenberg *et al.* used electron spin resonance (ESR) spectroscopy to monitor the O(^{3}P) decay rates in the presence of CS_2 at three different temperatures [17]. They detected SO($X\ \Sigma^-$) to confirm that the reaction did indeed take place and further extracted an activation energy, E_a = 0.25 kJ mol^{-1} for the process. A later study by Wei *et al.* is consistent with the first study, reporting an E_a = 0.31 kJ mol^{-1} for reaction 1(a) over the temperature range of 218-293 K [18].

Cooper *et al.* [11] used tunable infrared diode laser absorption spectroscopy (TDLAS) to study the reaction of ground state oxygen atoms with CS_2. The CO and OCS products were probed under vibrationally-relaxed conditions for the precise determination of their branching ratio. Results showed that the OCS + S channel contributes 8.5 ± 1.0% to the total reaction rate, and CO + S_2 channel contributes 3.0±1.0%. The undetected CS + SO channel was then assumed to have contributed to the balance.

Many other related studies have also been conducted such as the oxidation of CS_2 at high temperatures for the determination of the explosion limits of CS_2/O_2 mixture, reactive scattering using crossed molecular beams and chemiluminescence where the S_2 product of 1(b) was identified [19-22]. In addition, the kinetics of the reaction of carbon monosulfide, CS with O(^{3}P) atoms was also carried out [23] and the rate constant was detected to be 2.06×10^{-11} cm^3 molecule^{-1} s^{-1}.

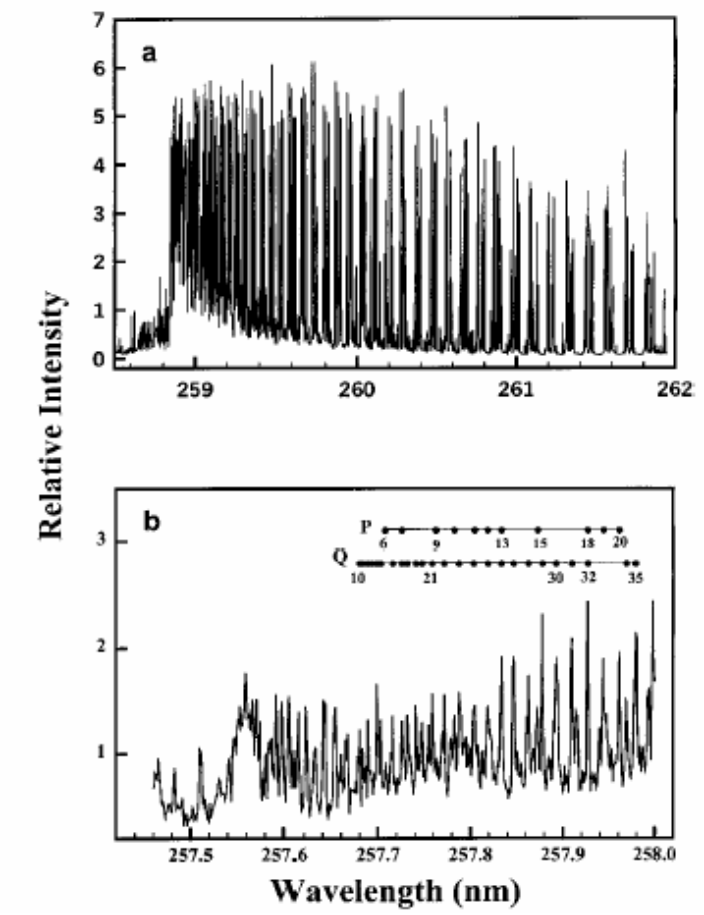

Figure 1.2 Rotationally resolved LIF spectra of (a) SO ($B^3\Sigma^-$, υ' = 1 – $X^3\Sigma^-$, υ '' =3) transition (b) CS ($A^1\Pi$, υ' = 0 – $X^1\Sigma^+$, υ '' =0) transition

1.3 Photolysis of nitrite and atmospheric chemistry of alkoxy radicals

1.3.1 Photolysis of nitrite

It has been known that photolysis of nitrite species results in the formation of OH radical [24] and hence their uses as precursors of OH radicals in the studies of kinetics and mechanisms of the reactions of OH radicals with organic compounds [25]. All the alkyl nitrites show a similar UV absorption spectrum. In the range 300-400 nm, a well-resolved vibrational progression is seen, corresponding to the A ^{1}A"← X^{1}A' (π*←n)

transition of N=O [26-27]. The UV absorption spectra of methyl nitrite and t-butyl nitrite are shown in Figure 1.3 [27].

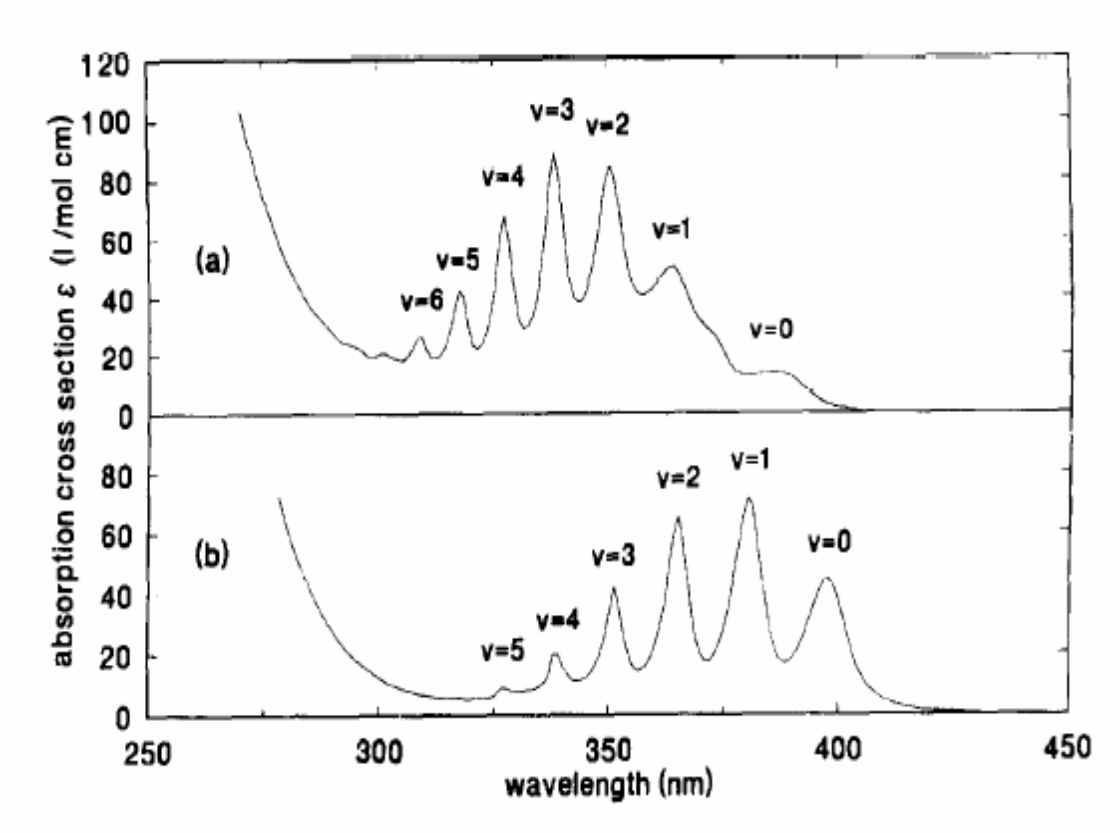

Figure 1.3 Electronic absorption spectra of (a) methyl and (b) t-butyl nitrite in the gas phase at room temperature

In previous work, [28-29] the final products of photolysis of alkyl nitrites in gas phase have been investigated. A general mechanism proposed for the primary process of nitrite decomposition was that the HNO split off, usually together with either an aldehyde or ketone. The H atom of NOH group can come from α, β or γ carbon atom of the nitrite. For the detachment of α hydrogen atom, the equation is represented by:

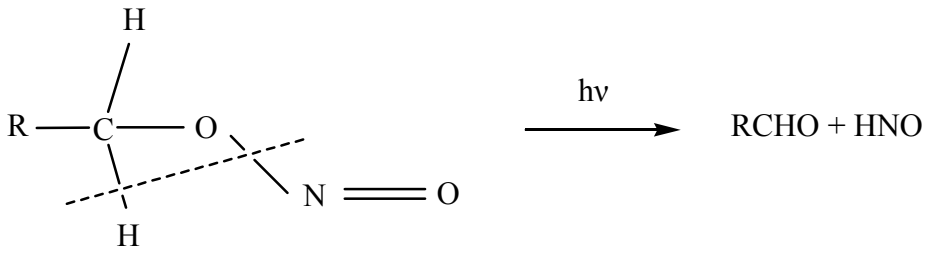

However Calvert and Pitts concluded that no unambiguous evidence was available on this channel [30]. Later, considerable evidence proved that the primary process for dissociation of nitrites in 300-400 nm is the homolytic cleavage of the RO-NO bond yielding NO and alkoxy radicals [31-32]. So, it appears that nitrites could be used as the precursor for alkoxy radicals and hence facilitating the studies on their unimolecular decomposition and reactions with O_2, NO and NO_2 for the last few years [33]. More recent work is focused on the quantum-state resolved probing of the NO photofragment by laser spectroscopy. The approach adopted most frequently in recent studies of the dissociation dynamics of HONO and its alkyl derivatives is pulsed photolysis and delayed probing of the nascent NO in its electronic ground state ($X\ ^2\Pi_i$) by laser-induced fluorescence (LIF) methods [34-35].

In the liquid phase, Townley *et al* have investigated the photolysis of primary, secondary and aromatic alkyl nitrites. The corresponding hydroxynitroso dimers were detected to be the products. The formation of the dimers was explained by the alkoxy radical decomposition mechanism as well as the alkoxy radical rearrangement mechanism [36-37].

1.3.2 Atmospheric chemistry of alkoxy radicals

Volatile organic compounds (VOCs) are emitted into the atmosphere from anthropogenic and biogenic sources [38-39] and they may also be formed *in situ* in the atmosphere as products of atmospheric transformations of other VOCs. The effects of these VOCs on the environment have generated intensive scientific and public concern due to possible harm on human, plant, and animal life. VOCs could undergo a number of physical and chemical processes leading to their removal from the atmosphere [40-41].

The photochemical production of OH radicals in the troposphere leads to the oxidative degradation of organic compounds emitted into atmosphere, thus limiting their accumulation, which would lead to disruption of biogeochemical cycles and detrimental effects on the environment. The initial attack of OH on the VOCs usually leads to the formation of peroxy radicals, RO_2. These radicals react with NO, other peroxy radicals or via self-reactions to generate the corresponding alkoxy radicals. So it is not surprising to find that alkoxy radicals are important intermediates in the chemical mechanism of atmospheric oxidation of many classes of VOCs [42]. In addition, the conversion of NO to NO_2 provides the net source of ozone as subsequent photolysis of NO_2 is followed by the recombination of the $O(^3P)$ photoproduct with O_2. The general oxidation scheme for the VOCs is outlined in Figure 1.4 [43-44].

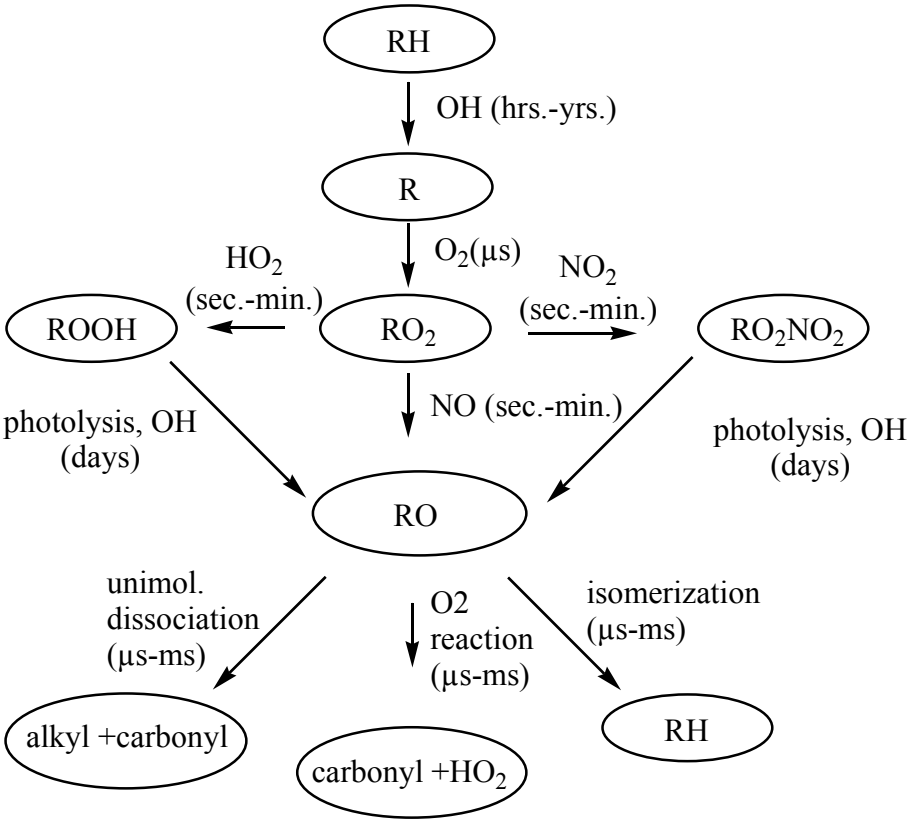

Figure 1.4 General hydrocarbon oxidation schemes

Once formed in the atmosphere, the alkoxy radicals can potentially undergo three different competing reaction pathways [40-41]: (1) unimolecular decomposition, which usually occurs through C-C bond fission to produce a carbonyl compound and alkyl radical. The rate constant is denoted by k_d. (2) Reaction with O_2, which occurs via α-hydrogen abstraction to form a carbonyl compound and HO_2 radical. The rate constant is donated by k_{O2}. (3) Unimolecular isomerization [45-46] by intramolecular H atom transfer (only effective for alkoxys which have four carbons) to generate a hydroxyl-substituted alkoxy radical. The rate constant is donated by k_{isom}. These competing pathways are illustrated for 2-pentoxy radical in Figure 1.5.

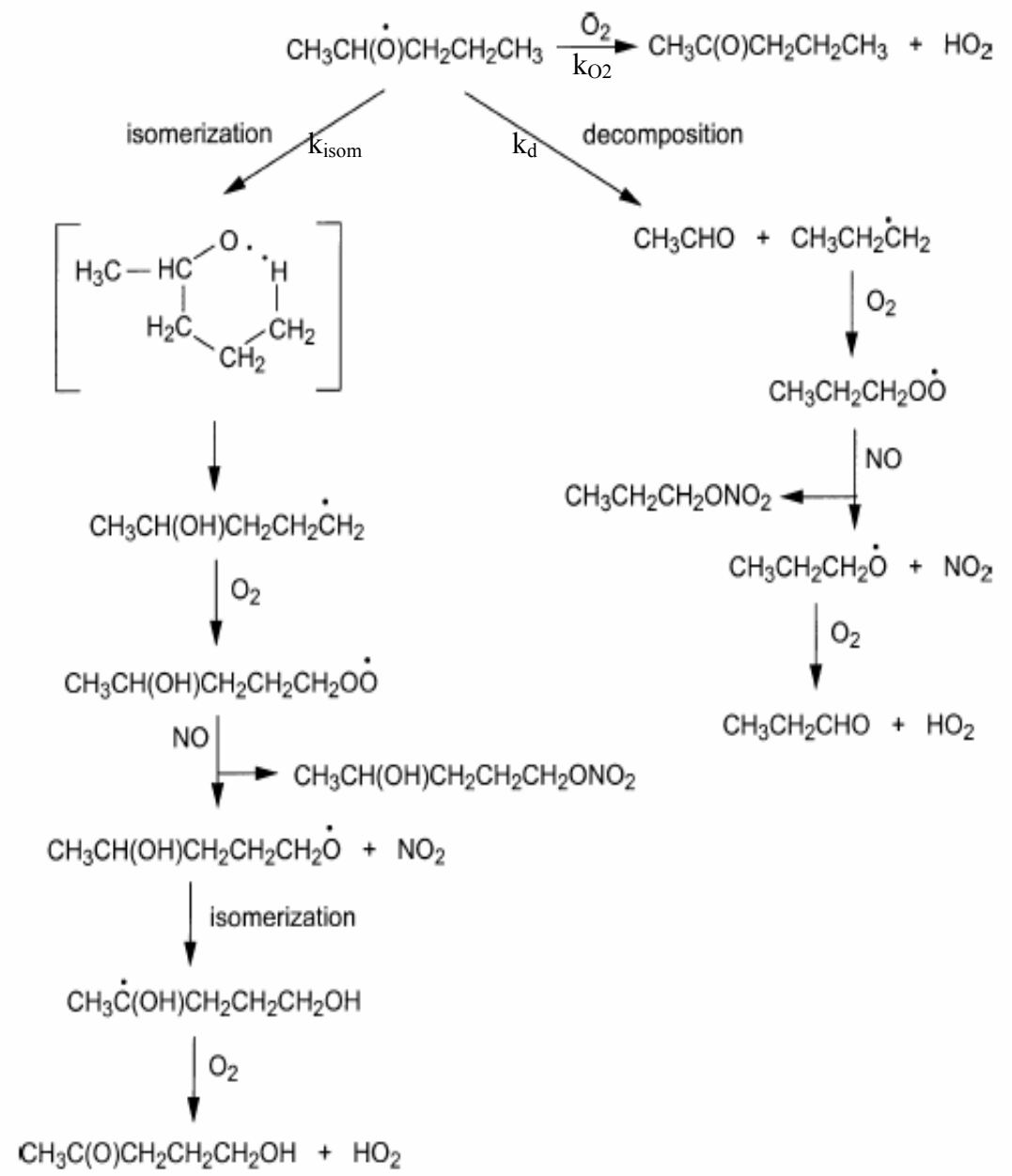

Figure 1.5 Chemistry of the 2-pentoxy radical, illustrating potential reaction pathways for a typical alkoxy radical [47]

It is the competition between the various potential alkoxy radical reaction pathways that determines the distribution of the eventually oxidized stable products in a particular oxidation scheme, and thus this in turn may influence the propensity of the parent organic compounds to generate ozone. In general, unimolecular decomposition

leads to a more rapid breakdown of the carbon chain and generates more reactive short chain carbonyl compounds which have a large potential for photochemical ozone formation [44]. On the other hand, reaction with O_2 and unimolecular isomerization leads to a preservation of the carbon chain with less reactive products and more highly substituted oxygenated species, hence dampening the potential for local ozone generation. Furthermore, the highly oxygenated species are more soluble and less volatile than short chain species and thus they are more prone to participate in aerosol nucleation and growth processes as well as aqueous-phase chemistry.

The importance of alkoxy radicals in the atmosphere has prompted the study of their chemistry via a number of different approaches: (1) Pyrolysis or photolysis of static gas mixtures and final-product analyses is used to determine relative rates for competing alkoxy radical reactions which provide information on the relative importance of alkoxy radical reaction pathways. (2) Time-resolved studies, using pulse laser-induced fluorescence for direct detection of the alkoxy radicals themselves. (3) Theoretical methods are now being applied to the determination of rate coefficients for unimolecular reactions of alkoxy radicals.

In the 1970s, the reaction of various alkoxy radicals were investigated by several groups to determined the unimolecular decomposition rates using relative rate method [48-50]. Normally, the nitrite or peroxide was used as the precursor and the end products were analyzed in the present of O_2 and NO_x to obtain the rates. Relative rate studies of alkoxy radical rate coefficients under conditions more relevant to the atmosphere have generally been conducted using “smog” or “environmental” chamber methodologies [51-53] and the final products are monitored via FTIR spectroscopy, GC

or GC/MS techniques, or chemical-ionization mass spectroscopy. The rate coefficients of alkoxy radical reactions are shown in Table 1.1, 1.2 and 1.3.

Table 1.1 Alkoxy decomposition rate constant (Adopted from reference [54])

	$k_{d,atm}/k_{O2}$ (molecule cm^{-3})	T (K)	$k_{d,atm}$(room temperature) (s^{-1})
2-butoxy	$(2.6\pm 0.35) \times 10^{18}$ 3.15×10^{18}	296 298	(3.9×10^{12}) exp(-47.1kJ mol^{-1}/RT)[a]
3-pentoxy	$(3.6 \pm 0.6) \times 10^{18}$	298	2.9×10^{4}
1-propoxy	$(3.8 \pm 0.41) \times 10^{16}$	298	300
2-propoxy	$(2.9 \pm 0.3) \times 10^{16}$	298	230

The same value of $k_{O2} = 8\times10^{-15}$ cm^{-3} $molecule^{-1}$ s^{-1} is adopted for all alkoxy radicals to derive $k_{d,atm}$ from relative measurements. a. Variable temperature experiments (280-313K) at 1 bar.

Table 1.2 Summary of the available data regarding the chemistry of halogenated alkoxy radicals [44]

Radicals	Dominant reaction pathway(s)	Products	Approximate rate (s^{-1})
CH_2FO	reaction with O_2	$HFCO + HO_2$	N.A.
CH_2ClO	reaction with O_2	$HClCO + HO_2$	N.A.
CH_2BrO	unimolecular decomposition	$CH_2O + Br$	$>1 \times 10^{7}$
CHFClO	unimolecular decomposition	HCOF + Cl	N.A.
CF_3CH_2O	reaction with O_2	$CF_3CHO + HO_2$	N.A.
CF_3CF_2O	unimolecular decomposition	$CF_2O + CF_3$	5×10^{6}
CF_3CFHO	unimolecular decomposition Reaction with O_2	CF_3+CFHO $CF_3CFO + HO_2$	N.A N. A

Table 1.3 Absolute rate constants for reactions of O_2 with alkoxy radicals [47]

RO• radical	$10^{15} \times k(298K)$ (cm^3 $molecule^{-1}s^{-1}$)	$10^{15} \times A$ (cm^3 $molecule^{-1}s^{-1}$)	Temperature range (K)
Methoxy	1.9	7.2	298-610
Ethoxy	8.1	2.4	295-354
1-propoxy	11	2.4	223-381
2-propoxy	7.1	1.5	218-384
1-butoxy	14 ± 7		293
2-butoxy	6.5 ± 2 12 ± 4 7.7	 0.133 0.12	293 223-311 221-266
3-pentoxy	7.2 ± 3.5 12 ± 6	 0.41	293 220-285

Until recently, direct studies of alkoxy radical chemistry have predominantly been carried out using pulsed laser-induced fluorescence [55-62]. This recent work has led to an extension of the database of reactions of larger alkoxy radicals with O_2 and NO, and more importantly is that it has led to the first direct determination of the dissociation processes [52-55, 62]. In parallel to these LIF studies, Carr and co-workers [63-64] have developed a flash photolysis/mass spectrometer system which they have applied to the time-resolved study of halogenated alkoxy radical reactions.

1.4 Hydrogen atom abstraction reactions

1.4.1 General features of hydrogen abstractions

Ever since the early 1930s when chemists recognized the important role of free radicals in many chemical processes, much effort has gone into measurements of the rates of elementary steps involving atom and molecular radicals [65]. The reactions can be classified as either unimolecular (decomposition or isomerization) or bimolecular ones. The latter reactions have two possible pathways; firstly, there are addition processes when the reactant is unsaturated since as alkenes and alkynes. Secondly, there are homolytic cleavages of a single bond by radicals. An atom transfer occurs from the reactant to the radical to form a new radical from the reactant. Normally, the atom most commonly transferred is hydrogen as shown below;

$$R^{\cdot} + H\text{-}X \longrightarrow R\text{-}H + X^{\cdot} \qquad (3)$$

Hydrogen atom abstraction reactions by organic radicals are ubiquitous in organic chemistry [66]. The reactivities of differently bonded hydrogen atoms are significantly different. The reactivity of reaction 3 is mainly determined by the difference in the stability of the reactant ($R^{\cdot}$) and product ($X^{\cdot}$) radicals. If the stability of $R^{\cdot}$ is decreased, while keeping the same H-X compound, the rate constant will be larger [67]. Keeping the $R^{\cdot}$ and changing the reactant in order to form a more stable product radical will also give rise to a larger rate constant. Since the fundamental factor in determining radical stability results from the delocalization of the lone electronic spin, it can be expected that resonance factors will be of major importance for radical reactivity.

In some studies, the hydrogen abstraction reaction is applied as a standard process in competition with other radical steps to be studied. The reactivity of the compounds investigated is usually expressed by the rate constant ratio of the competing reactions. The superiority of this method lies in the comparison of elementary steps of the same kinetic order with respect to the radical.

A good way for exploiting the advantages of competing radical reactions of the same kinetic order is offered by chain reactions. Although the concentration of the chain carrier radicals is low, owing to their high reactivity and short lifetime, they can produce easily-measured macroscopic changes in the amount of molecular reactants and products of the chain process. Any species which is able to bring about reaction 3 with the chain carrier radical and produces another radical of lower reactivity will affect the propagation step, and hence reduces the rate of the chain process. This species will then be called an inhibitor and the procedure to evaluate rate constants is known as the inhibition method.

In every radical process studied to date, the rates of hydrogen abstractions from aliphatic hydrocarbons increase in the order of primary < secondary < tertiary structure [68]. This order is independent of the nature of the attacking radical and is most easily explained as due to the strengths of the C-H bonds being broken. Table 1.4 gives the data for four radicals which follow the trend.

Table 1.4 Relativity of aliphatic hydrogens toward various radicals [68]

$X\cdot + RH \rightarrow HX + R\cdot$				
Type of hydrogen	$CH_3\cdot$(455K)	O·(333K)	t-BuO·(313K)	Cl· (298K)
Primary	1	1	1	1
Secondary	7	9.3	8	3.6
Tertiary	50	44	44	4.2
Cyclohexane	-	8.3	15	2.5

1.4.2 Abstraction of hydrogen by alkoxy radicals

Alkoxy radicals may be generated in a variety of ways, including the decomposition of alkyl nitrites, alkyl peroxides and hypohalites. When alkoxy radicals are formed in the presence of a hydrogen-containing substrate R'H, hydrogen atoms can be abstracted from the substrate by the radical to yield an alcohol according to the equation:

$$RO\cdot + R'H \longrightarrow ROH + R' \qquad (4)$$

For most alcohols, the bond dissociation energy D (RO-H) is approximately constant at about 102 kcal mol^{-1} for any given substrate molecule, reaction 4 will have roughly equal exothermicity for many alkoxy radicals [69].

Most of the available information indicates that alkoxy radicals are appreciably more reactive than alkyl radicals and the differences in reactivity arise from a lowered energy of activation rather than from differences in pre-exponential factors. It appears also that when various types of hydrogen atoms are present in a substrate, the order of

increasing ease of removal is primary hydrogen < secondary hydrogen < tertiary hydrogen, the same as that of diminishing C-H bond strength.

Various peroxydicarbonates [70-71] have been decomposed in solution, and the decreasing tendency of alkoxy radicals to react by hydrogen atom abstraction reported to be in the order,

$$CH_3O\cdot > C_2H_5O\cdot > \text{tert-}C_4H_9O\cdot$$

The high yields of methanol observed in such systems where methoxy radicals are produced both in gaseous [72] and liquid phase [73] and over a wide range of temperatures, demonstrated the great potential of $CH_3O\cdot$ radical reacting by hydrogen abstraction. However, more complex alkoxy radicals usually react in more than one way. For example, the t-butoxy radical can either abstract a hydrogen atom from hydrogen donor RH or undergo β-scission to form acetone.

1.4.3 Abstraction reactions by t-butoxy radical

Because of the availability of di-tert-butyl peroxide and its ease of thermal and photochemical decompositions to produce tert-butoxy radicals, it has been the most extensively studied alkoxy radical, particularly regarding its reactivity in the liquid phase. In general the relative abstraction reactivity of the tert-butoxy radical towards organic compounds has been measured by competitive method where two substrates (R_1H and R_2H) react with tert-butoxy and the radicals then form products such as organic chlorides by reaction with CCl_4 solvent [65]. The ratio of rate constants may be determined indirectly by comparing ROH/ ketone ratios on reaction with each substrate, separately or directly, and by determining the relative yields of R_1Cl and R_2Cl or the consumption of

reactants in competitive experiments. Both competitive methods give fairly reliable relative rate constants in most cases.

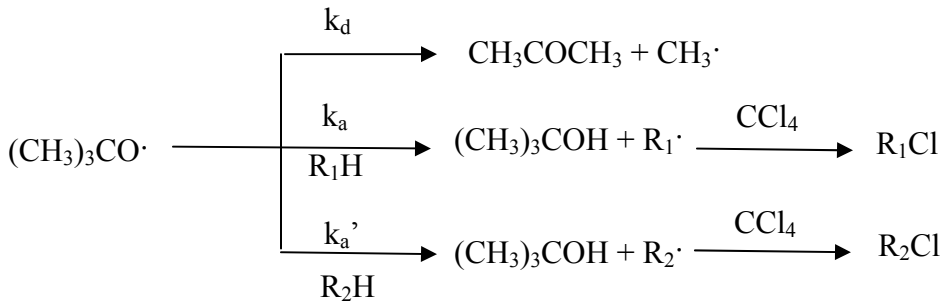

In the gas phase, hydrogen atom abstraction has been demonstrated for a variety of substrates such as alcohol [74], esters [75], ether [76] and alkanes [77-78]. However accurate quantitative kinetic data are available for only a few compounds. On the other hand, the reactions of tert-butoxy radicals with liquid hydrocarbons in the liquid phase have received much more attention. Williams, Oberright and Brooks [79] have measured the ratio of abstraction reaction over decomposition at 135°C for a variety of hydrocarbons. The trend in abstraction rates in order of increasing rate is:

Primary < secondary < tertiary, relative rates being 1: 7: 28

Walling and Jacknow [80] have studied the relative rate constants of hydrogen abstraction by tert-butoxy from primary, secondary and tertiary C-H bonds in n-butane and 2, 3-dimethylbutane. At 40°C the ratio was primary: secondary: tertiary = 1: 8: 44.

An extensive investigation [81] of the reactivity of derivatives of methane, ethane and toluene towards hydrogen atom attack by tert-butoxy radicals at 135°C has also been reported and the results indicate that the reactivities are greatly influenced by conjugation and polar effects. Wallace and Gritter [82] have shown that the reactivities of cyclic ethers and epoxides towards tert-butoxy radicals depend on the ring size, relative

reactivities being in the order: 5 ≈ 6 > 4 > 3. Table 1.5 summarized the rates constants, logA and calculated E of abstraction from various substrates.

Johnston and Williams [83] have shown that the influence of substituents on the reactivity of substrate molecules is determined by their polar character, abstraction being assisted by electron-repelling groups and hindered by electron-attracting groups. The reactivity of various sulfur-containing compounds [84-85] towards tert-butoxy radical generated thermally and photochemically has been studied with the reactivities towards hydrogen atom abstraction being in the order:

$ArNMe_2 > ArNMe > ArSMe \approx ArOMe$

Griller *et al* [86] determined the absolute rate constants for reaction of tert-butoxy radical with amines in liquid phase at low temperature using ESR and laser photolysis. They showed that the hydrogen abstraction took place at the carbon atom adjacent to the nitrogen and these reactions are much faster than hydrogen abstractions from hydrocarbons. This can be explained if such C-H bonds are relatively weak [87-88] as a result of the large stabilization of the α-aminoalkyl radical afforded by delocalization of the unpaired electron onto nitrogen. The reactivity order of different type of amines is tertiary ≈secondary > primary.

Table 1.5 Tert-butoxy radical-organic compounds: summary of absolute rate constants and parameters at 313 K per active hydrogen [65]

RH bond	K ($M^{-1}s^{-1}x10^{-4}$)	log($A/M^{-1}s^{-1}$) (±0.5)	E (kJ mol^{-1})
Alkane			
pri	0.28	9.0	33.3
sec	3.6	9.2	27.8
tert	12.6	9.4	25.8
Alkene			
pri	5.3	8.0	19.6
sec	24	8.2	16.9
tert	52	8.4	16.1
Ethers(α CH)			
pri	10	8.7	22.2
sec	31	8.7	19.2
Alkyl-X(α CH)			
chloro	1.4	9.0	29.1
cyano	0.18	9.0	34.4
acetoxy	0.81	9.0	30.5
Ketone(α CH)			
pri	0.074	8.7	34.9
sec	0.6	8.5	28.3
cyclo	1.0	8.7	28.2

1.4.4 Reactions of Chlorine atoms ($^2P_{3/2}$) with hydrocarbons

Recent impetus for investigating chlorine chemistry has come from the discovery that Cl atoms arising from the solar photolysis of man-made chlorinated compounds, especially chlorofluorocarbons (CFCs), contribute to the depletion of

stratospheric ozone [89-90]. The reaction of Cl atoms with hydrocarbons constitutes one of the chain terminating reactions in the ozone destruction cycle. Further, it has also been proposed that atomic Cl is an important oxidizing species in the troposphere, especially in the marine boundary layer [91-92].

The reactions of Cl atoms with alkanes are prototypical atom abstractions. Generation of alkyl radicals by Cl-atom reaction with hydrocarbons is also widely used in laboratories for initiating oxidation and thus studying the mechanisms of reactions of great importance in combustion [93]. The reactions of Cl atoms can be used to gain thermochemical information about hydrocarbon radicals via the Cl+ RH ↔HCl+ R reaction, using the well-known thermochemistry of Cl, HCl and many stable hydrocarbons [94].

The reactions of Cl with alkenes and alkynes display a richer chemistry because of the possibility of addition to form a chlorinated hydrocarbon radical. Alkenes and alkynes reacting with Cl proceed largely by addition at low temperatures. The rule that addition forms the more stable radical would predict, in general, terminal additions to double bonds. Addition of Cl to an unsaturated hydrocarbon is the reverse of the thermal dissociation of the corresponding chlorinated radical. Therefore, the addition reactions can be used to gain thermochemical information about the radical adduct. The kinetic data for reaction of Cl with hydrocarbon was shown in Table 1.6.

However, kinetic studies of the reactions of Cl atoms with oxygenated molecules are less extensive than those of the corresponding alkanes, and remain a subject of active current investigation, largely because of environmental concerns. Typically, the reactions

of small alcohols and ethers are rapid and have been found to be effectively independent of temperature, where investigated [95-98]. Attention is then turned to the reactions of Cl atoms with functionalized organic molecules such as alcohols, ethers, amines and methyl halides to unravel the consequences of the addition of a functional group.

Table 1.6 Temperature dependence of rate coefficients for reaction of Cl with hydrocarbon [96]

Reaction (temperature)	A(cm^3 $molecule^{-1}$ s^{-1})	E_a (kJ mol^{-1})
Cl + CH_4 (200-500 K)	1.37×10^{-12} $(T/298)^{1.96}$	0.36
(200-300K)	9.6×10^{-12}	0.64 ± 0.12
Cl + C_2H_6 (292-600K)	$(8.6 \pm 0.5) \times 10^{-11}$	0.041 ± 0.012
(292-800K)	$(3.4 \pm 1.4) \times 10^{-11}(T/298)^{(0.7\pm0.3)}$	-0.072 ± 0.53
(200-300K)	7.7×10^{-11}	0.043 ± 0.043
(200-600K)	8.2×10^{-11}	0.048 ± 0.048
Cl + C_2H_4 (500-800K)	$(6.2 \pm 1.4) \times 10^{-11}$	1.63 ± 0.22
Cl + C_3H_8 (292-700K)	$(1.38 \pm 0.03) \times 10^{-10}$	0.00 ± 0.024
(220-600K)	1.2×10^{-10}	0.019 ± 0.096
(200-300K)	1.2×10^{-10}	0.019 ± 0.12
Cl + C_3H_6 (290-800K)	$(4.9 \pm 0.5) \times 10^{-11}$	0.041 ± 0.024
Cl + propyne (400-800K)	$(3.7 \pm 1.0) \times 10^{-11}$	0.33 ± 0.072
(292-800K)	$(1.25 \pm 0.21) \times 10^{-12}(T/298)^2$	0.041 ± 0.024
Cl + allene (292-800K)	$(3.7 \pm 1.7) \times 10^{-10}$	0.79 ± 0.14
	$(1.25 \pm 0.68) \times 10^{-11}(T/298)^2$	0.25 ± 0.15
Cl + isoprene	$(8.2 \pm 5.1) \times 10^{-11}$	0.053 ± 0.084

1.5 Main Objectives

The kinetics and dynamics of the reaction between $O(^3P)$ and CS_2 are very important not only in basic research but also in atmospheric and combustion chemistry. However, no kinetic data and reaction mechanisms are available for the reactions of $O(^3P)$ with CSe_2, SCSe and OCSe. These three compounds have the same linear structure as CS_2, but the bond length for the C=S is different from C=Se and C=O. In order to compare their chemistry, branching ratio and rate coefficient so that we can understand how does it affect on the reaction mechanism by changing sulfur to oxygen or selenium, the reactions between $O(^3P)$ and CSe_2, SCSe and OCSe will be carried out using uv lamp photolysis Fourier Transform Infrared (FTIR) absorption spectroscopy, as described in Chapter 2. The measurements of overall rate coefficients will be accomplished by calibrating against the literature value of the rate coefficient for O (^3P) with CS_2 (4×10^{-12} cm^3 $molecule^{-1}$ s^{-1}). The different reaction pathways and branching ratios for above reactions will also be discussed.

Hydrofluorocarbons (HFCs) and hydrochlorofluorocarbons (HCFCs) have been widely used as replacements for chlorofluorocarbons (CFCs). The halogenated alkoxy radicals are key intermediates for the tropospheric removal of HFCs and HCFCs. It is important that laboratory measurements should establish the pathways and rates of the reactions by which the HFC's are oxidised in the atmosphere to ensure that their breakdown leads to no undesirable environmental consequences. There are different ways for the further decomposition of alkoxy radicals in the oxygen-rich atmosphere although its unimolecular decomposition is also important and not yet well-studied. In Chapter 3,

the unimolecular decomposition of alkoxy radicals, especially the trifluoroethoxy radical, which is the oxidation product from HFC-143a under atmospheric environment, generated from 355 nm pulsed nanosecond laser photolysis of its parent nitrite in the gas phase will be investigated using FTIR Spectroscopy. The aim of this project is to detect the decomposition products of different alkoxy radicals so that we can not only understand the preferred unimolecular decomposition way of different alkoxy radicals but also shed light on the possible environmental effect of these compounds.

Hydrogen atom abstraction reactions by free radicals represent a significant area of free radical research. The objective of Chapter 4 is to extend the kinetic data for the hydrogen abstraction reactions by t-butoxy radical to substrates such as amines, halogenated organic compounds and some nitriles. In this work, rate constants and Arrhenius parameters will be determined for several hydrogen donors using relative rate method. The reactivity of the donors will be discussed.

Fluoro alcohols are proposed to be the new generation of CFC alternative in certain industrial applications. In order to determine the environmental impact of FAs released into the troposphere, the atmospheric lifetimes and the nature and fate of the resulting oxidation products are needed. This, in turn, requires kinetic data for the atmospheric oxidation processes and information on the degradation mechanism. In Chapter 5, the reactions of $O(^3P)$ and Cl ($^2P_{3/2}$) atoms with $CF_3CHOHCF_3$, CF_3CH_2OH and CCl_3CH_2OH will be studied. The reaction rate constants will be measured and degradation products of these alcohols will be recorded in order to understand possible reaction pathways of these alcohols.

Reference

1. E. Hirota and K. Kawaguchi, Annu. Rev. Phys. Chem., 36, 53, 1985

2. C. A. Taatjes and J. F. Hershberger, Annu. Rev. Phys. Chem., 52, 41, 2001

3. D. L. Baulch, C. J. Cobos, R. A. Cox, P. Frank and G. Hayman, et al., J. Phys. Chem. Ref. Data 23, 847, 1994

4. R. Atkinson, D. L. Baulch, R. A. Cox, R. F. Jr. Hampson and J. A. Kerr, et al., J. Phys. Chem. Ref. Data 26, 521, 1997

5. W. B. DeMore, S. P. Sander, D. M. Golden, R. F. Hampson and M. J. Kurylo, et al. Chemical Kinetics and Photochemical Data for Use in Stratospheric Modeling. Pasadena, CA: Jet Propulsion Lab., 266, 1997

6. M. C. Lin, Advan. Chem. Phys., 42, 13, 1980

7. G. S. Tyndall and A. R. Ravishankara, Int. J. Chem. Kinet. 23, 483, 1991

8. Z. Farago, Combust. Sci. Technol., 79, 73, 1991

9. Y. Murakami, M. Kosugi, K. Susa, T. Kobayashi and N. Fujii, Bull. Chem. Soc. Japan., 74, 1233, 2001

10. S. J. Arnold and H. Rojeska, Appl. Opt., 12, 169, 1973

11. W. F. Cooper and J. F. Hershberger, J. Phys. Chem. 96, 5405, 1992

12. D. S. Y. Hsu, W. M. Shaub, T. L. Burks and M. C. Lin, Chem. Phys., 44, 143, 1979

13. I. R. Slagle, J. R. Gilbert and D. Gutman, J. Chem. Phys., 61, 704, 1974

14. W. M. Smith, Trans. Faraday Soc., 64, 378, 1968

15. P. L. Moore, P. N. Clough and J. Geddes, Chem. Phys. Lett., 17, 608, 1972

16. Y. Cheng, J. Han, X. Chen, Y. Ishikawa and B. R. Weiner, J. Phys. Chem. A. 105, 3693, 2001

17. A. A. Westenberg and N. deHaas, J. Chem. Phys., 50, 707, 1969

18. C. N. Wei and R. B. Timmons, J. Chem. Phys., 62, 3240, 1975

19. Y. Murakami, M. Kosugi, K. Susa, T. Kobayashi and N. Fujii, Bull. Chem. Soc. Japan 74, 1233, 2001

20. C. N. Wei and R. B. Timmons, J. Chem. Phys. 62, 3240, 1975

21. J. J. Rochford, L. J. Powell and R. Grice, J. Phys. Chem. 99, 15369, 1995

22. P. D. Naik, U. B. Pavanaja, A. V. Sapre, K. V. S. Ramarao and J. P. Mittal, Chem. Phys. Lett. 186, 565, 1991

23. I. W. M. Smith, Faraday Soc. Discuss. 43-44, 194, 1967

24. J. Mack and J. R. Bolton, J. Photochem Photobio A: Chemistry, 128, 1, 1999

25. M. P. S. Andersen et al, Int. J. Chem. Kinet., 35(4), 159, 2003

26. B. A. Keller, P. Felder and J. R. Huber, Chem Phys. Lett., 124, 135, 1986

27. M. Hippler, F.A. H. Al-Janabi and J. Pfab, Chem. Phys. Lett., 192, 173, 1992

28. H. W. Thompson and F. S. Dainton, Trans. Faraday Soc., 33, 1546, 1937

29. C. H. Purkis and H. W. Thompson, Trans. Faraday Soc., 32, 1466, 1936

30. J. G. Calvert and J. N. Pitts, Jr., Photochemistry, John Wiley and Sons, Inc., New York, N. Y., 480, 1966

31. B. E. Ludwig and G. R. McMillan, J. Am. Chem. Soc., 91, 1085, 1969

32. H. A. Wiebe and J. Heicklen, J. Am. Chem. Soc., 95, 7, 1973

33. P. Morabito and J. Heicklen, Int. J. Chem. Kinet., 17, 535, 1985

34. R. N. Dixon and H. Rieley, J. Chem. Phys., 91, 2308, 1989

35. M. P. Docker, A. Ticktin, U. Briihlmann and J.R. Huber, J. Chem. Soc. Faraday Trans II, 85, 1169, 1989

36. P. Kabasakalian and E. R. Townley, J. Am Chem. Soc., 20, 2711, 1962

37. P. Kabasakalian, E. R. Townley and M. D. Yudis, J. Am Chem. Soc., 84, 2716, 1961

38. A. Guenther, C. Geron, T. Pierce, B. Lamb, P. Harley and R. Fall, Atmos. Environ., 34, 2205, 2000

39. M. Placet, C. O. Mann, R. O. Gilbert and M. J. Niefer, Atmos. Environ., 34, 2183, 2000

40. R. Atkinson, Atmos. Environ, 34, 2063, 2000

41. R. Atkinson and J. Arey, Chem Rev., 103, 4605, 2003

42. R. Atkinson, Int. J. Chem. Kinet., 29, 99, 1997

43. R. Atkinson and W. P. L. Carter, J. Atmos. Chem., 13, 195, 1991

44. J. J. Orlando and G. S. Tyndall, Chem. Rev., 103, 4657, 2003

45. R. Atkinson, Int. J. Chem. Kinet., 29, 99, 1999

46. E. S. C. Kwok, J. Arey and R. Atkinson, J. Phys. Chem., 100, 214, 1996

47. R. Atkinson and J. Arey, Chem. Rev., 103, 4605, 2003

48. L. Batt and R. T. Milne, Int. J. Chem. Kinet., 6, 945, 1974

49. L. Batt and R. T. Milne, Int. J. Chem. Kinet., 8, 59, 1976

50. L. Batt, Int. J. Chem. Kinet., 11, 977, 1979

51. S. M. Aschmann, A. A. Chew, J. Arey and R. Atkinson, J. Phys. Chem. A, 101, 8042, 1997

52. M. Blitz, M. J. Pilling, S. H. Robertson and P. W. Seakins, Phys. Chem. Chem. Phys., 1, 73, 1999

53. F. Caralp, P. Devolder, C. Fittschen, N. Gomez, H. Hippler, R. Me´reau, M. T. Rayez, F. Striebel and B. Viskolcz, Phys. Chem. Chem. Phys., 1, 2935, 1999

54. P. Devolder, J. Photochem. Photobio. A: Chemistry, 157, 137, 157

55. P. Devolder, Ch. Fittschen, A. Frenzel, H. Hippler, G. Poskrebyshev, F. Striebel and B. Viskolcz, Phys. Chem. Chem. Phys., 1, 675, 1999

56. C. Fittschen, H. Hippler and B. Viskolcz, Phys. Chem. Chem. Phys., 2, 1677, 2000

57. W. Deng, C. Wang, D. R. Katz, G. R. Gawinski, A. J. Davis and T. S. Dibble, Chem. Phys. Lett., 330, 541, 2000

58. W. Deng, A. J. Davis, L. Zhang, D. R. Katz and T. S. Dibble, J. Phys. Chem. A, 105, 8985, 2001

59. C. Fittschen, A. Frenzel, K. Imrik and P. Devolder, Int. J. Chem. Kinet., 31, 860, 1999

60. H. Hein, A. Hoffmann and R. Zellner, Phys. Chem. Chem. Phys., 1, 3743, 1999

61. F. Wu and R. W. Carr, Chem. Phys. Lett., 305, 44, 1999

62. F. Wu and R. W. Carr, J. Phys. Chem. A, 105, 1423, 2001

63. F. Wu and R. W. Carr, J. Phys. Chem. A, 100, 9352, 1996

64. O. J. Nielsen, E. Gamborg, J. S. Timothy, J. Wallington and M. D. Hurley, J. Phys. Chcm., 98, 9518, 1994

65. D. G. Hendry, T. Mill, L. Piszkiewicz, J. A. Howard and H. K. Eigenmann, J. Phys. Chem. Ref. Data, 3, 944, 1974

66. H. Tachikawa, N. Hokari and H. Yoshida, Chem. Phys. Lett., 241, 7, 1995

67. M. Simonyi and F. Tüdős, Adv. Phys. Org. Chem., 9,127, 1971

68. W. A. Pryor, free radicals, 1966

69. P. Gray, R. Shaw and J. C. J. Thynne, Progress in Reaction Kinetics, 4, 63, 1967

70. G. R. McMillan, J. Am. Chem. Soc., 82, 2422, 1960

71. H. C. Mcbay, O. Tucker and A. Milligan, J. Org. Chem., 19,1003, 1954

72. F. F. Rust, F. H. Seubold and W. E. Vaughan, J. Am. Chem. Soc., 72, 228, 1950

73. W. H. Urry and E. W. R. Steacie, J. Am. Chem. Soc., 75, 250, 1953

74. J. H. Raley, F. H. Seubold and W. E. Vaughan, J. Am. Chem. Soc., 70, 3258,1948

75. R. L. Huang and S. S. Singh, J. Chem. Soc., 891, 1958

76. Y. E. Lee and K. Y. Choo, Int. J. Chem. Kinet., 18, 267, 1986

77. M. I. Sway and D. J. Waddington, J. Chem. Soc. Perkin Tran., II, 63, 1984

78. A. L. William, E. A. Oberright and J. W Brooks, J. Am. Chem. Soc., 78, 1190, 1956

79. C. Walling and B. B. Jackson, J. Am. Chem. Soc., 82, 6108, 1960

80. K. Schwetlick, R. Karl and J. Jentzsch, J. Prakt. Chem., 22, 113, 1963

81. T. J. Wallace and R. J. Gritter, Tetrahedron, 19, 657, 1963

82. K. M. Johnston and G. H. Williams, J. Chem. Soc., 1446, 1960

83. H. B. Henbest, J. A. W. Reid and C. J. M. Stirling, J. Chem. Soc., 1217, 1964

84. H. B. Henbest, J. A. W. Reid and C. J. M. Stirling, J. Chem. Soc., 1220, 1964

85. D. Griller, J. A. Howard, P. R. Marriott and J. C. Scaiano, J. Am. Chem. Soc., 103, 619, 1981

86. P. E. Elford and B. P. Roberts, J. Chem. Soc. Perkin Trans. 2, 1413, 1998

87. M. A. Gela and A. J. Colussi, J. Phys. Chem., 88, 5995, 1984

88. T. J. Burkey, A. L. Castelhano, D. Griller and F. P. Lossing, J. Am. Chem. Soc., 105, 4701, 1983

89. F. S. Rowland, A. Rev. Pys. Chem., 42, 731, 1991

90. M. J. Molina, L. T. Molina and C. E. Kolb , A. Rev. Phys. Chem., 47, 327, 1996

91. B. J. Finlayson -Pitts, Res. Chem. Intermediates, 19, 235, 1993

92. C. W. Spicer, E. G. Chapman, B. J. Finlayson -Pitts, R. A. Plastridge, J. M. Hubbe, J. D. Fast and C. M. Berkowitz, Nature, 394, 353, 1998

93. J. D. DeSain, S. J. Klippenstein, C. A. Taatjes, M. D. Hurley and T. J. Wallington, J. Phys. Chem. A., 107, 1992, 2003

94. J. Berkowitz, G. B. Ellison and D. Gutman, J. phys. Chem., 98, 2744, 1994

95. C. A. Taatjes, Intern. Rev. Phys. Chem.18, 419, 1999

96. P. W. Seakins, J. J. Orlando and G. S. Tyndall, Phys. Chem. Chem. Phys., 6, 2224, 2004

97. F. Taketani, K. Takahashi, Y. Matsumi and T. J. Wallington, J. Phys. Chem. A, 109, 3935, 2005

98. S. Rudíc, C. Murray, J. N. Harvey and A. J. Orr-Ewing, J. Chem. Phys., 120, 186, 2004

– CHAPTER 2 –

O (^{3}P) atom reactions with CSe_2, SCSe and OCSe

2.1 Introduction

The reaction of oxygen (^{3}P) atom with carbon disulfide, CS_2 has received considerable attention for its role in atmospheric chemistry especially in the elucidation of global sulfur cycle leading to acid rain [1]. Three main product channels have been identified for this reaction [2];

$$O(^3P) + CS_2 \rightarrow CS + SO(^3\Sigma^-) \qquad \Delta_fH° = -80.7 \text{ kJ/mol} \qquad 1(a)$$

$$\rightarrow CO + S_2(^3\Sigma^-_g) \qquad \Delta_fH° = -347.8 \text{ kJ/mol} \qquad 1(b)$$

$$\rightarrow OCS + S(^3P) \qquad \Delta_fH° = -227.4 \text{ kJ/mol} \qquad 1(c)$$

Cheng *et al*. has studied the dynamics of the dominant channel 1(a) by examining the vibrational state distributions of CS($^1\Sigma$) and SO($^3\Sigma$) using laser-induced fluorescence spectroscopy [3]. Cooper et al. used tunable infrared diode laser absorption spectroscopy (TDLAS) to determine a value of 2.8 for the branching ratio of 1(c)/1(b) [2]. Other related studies include a study of the oxidation of CS_2 at high temperatures, temperature-dependent kinetics for the determination of the activation energy of 1(a), reactive scattering using crossed molecular beams and chemiluminescence where the S_2 product

of 1(b) was identified [4-7]. In addition, the kinetics of the reaction of carbon monosulfide, CS with O(^{3}P) atoms were also carried out [8].

However we found that oxygen atom reactions with carbon chalcogenide species such as carbon diselenide (CSe_2) and carbon selenide sulfide (SCSe) have not been explored. Only one related investigation where the vibrational distribution of highly excited CO products after UV photolysis of a mixture containing nitrogen dioxide, NO_2 and CSe_2 was measured [9]. In this chapter, FTIR absorption spectroscopy is used to extend the scope of O(^{3}P) atom reactions to CSe_2 and SCSe under static cell conditions. Although these Se-containing species are not observed in the atmosphere, it is still of fundamental interest to compare and contrast the effect of chalcogen substitution in CX_1X_2 (X = S, Se or O) on their reactions with O(^{3}P) atom. FTIR spectroscopy is ideal for broadband monitoring of the changes in the chalcogenide precursor and product concentrations upon O atom reactions. The generation of O (^{3}P) atoms is accomplished by using UV xenon lamp photolysis of NO_2 [2]. Apart from examining the primary reactions, some secondary processes such as the reactions of O atoms with the product OCSe and CSe with O_2 will be studied as well. Computational studies of the vibrational frequencies and band strengths of the species involved and the energies and geometries of reactive intermediates and transition states in these reactions will be determined. However, the assumed dominant channel of the O/CSe_2 system which produces CSe and SeO could not be directly investigated under static cell conditions. Its importance will be inferred by measuring and then subtracting out the contributions from other product channels. Such reactions would be best conducted using flow cell reactors but the difficulty of obtaining large amount of CSe_2 and SCSe precludes their study here.

2.2 Experimental section

2.2.1 Synthesis of CSe_2 and SCSe

CS_2 (99%) was purchased from Ajax Chemicals and distilled before use. Cylinders of, NO (99%), NO_2 (99%), OCS (97%) and SF_6 (99.9%) gases were available from Linde gas and CO (20% in Argon) from Messer used without further purification. $AgNO_3$ (99%), KNCSe (99%) and AgNCS (97%) were purchased from Sigma-Aldrich.

Because of the difficulty of obtaining commercial CSe_2 and SCSe samples, their syntheses have to be carried out. A literature search revealed that CSe_2 could be produced by passing dichloromethane vapor over hot selenium powder at 700^{o}C while SCSe was made by passing CS_2 over iron (II) selenide at 650^{o}C [10-11]. However attempts using these methods often resulted in severe contamination by CH_2Cl_2 or CS_2 despite careful steps taken for sample purification. Therefore an alternative method was devised in order to obtain gaseous samples of the chalcogenides from silver selenocyanate salts. AgNCSe was synthesized from an equimolar reaction of potassium selenocyanate, KNCSe with $AgNO_3$ aqueous solution.

Typically, CSe_2 was generated from the vacuum decomposition (250-300^{o}C) of AgNCSe (1-2 grams) in a 15 cm-long, 3 cm-diameter glass cell equipped with CaF_2 windows for passage of the FTIR beam. Upon inspection by FTIR spectroscopy, the main decomposition product was CSe_2 (ν = 1300 cm^{-1}) with a little amount of HCN (ν = 3314 cm^{-1}, <1% o CSe_2). The latter presumably arose due to reactions with hydrogen contaminants on the wall of the gas cell. Due to the differences in boiling points, HCN could be gradually removed after CSe_2 was collected in a dry ice/acetone trap. It was

estimated that during each synthesis, about 15-20 Torr of CSe_2 could be generated in a total volume of 500 cm^3; this amount was sufficient for a few kinetic runs in the static cell. For the production of SCSe, AgNCSe (0.5-3 grams) and silver thiocyanate, AgNCS (0.5-3 grams) were mixed and decomposed together at similar temperatures yielding vapors containing the three expected products, CS_2 (ν = 1520 cm^{-1}), SCSe (ν = 1435 cm^{-1}) and CSe_2 [12]. The production of exclusively SCSe was attempted by varying the ratio of the salt precursors but it was unsuccessful because the resulting vapor contained either copious amount of CS_2 at high ratios of AgNCS to AgNCSe or very little SCSe at low ratios of AgNCS to AgNCSe. However, contamination with CSe_2 could easily be removed by UV photodissociation at 254 nm [13]. Reddish solids attributed to selenium and carbon deposits were produced upon photolysis. Unfortunately, CS_2 could not be eliminated using the same method or by cold traps, so experiments carried out on SCSe always contained some amount of CS_2. Despite this, the simple method of decomposing the silver salts using their cyanate salts offered a very convenient way of generating CSe_2 or SCSe vapour.

2.2.2 Experimental setup

A typical photolysis experiment would begin with the addition of carbon chalcogenide (3-10 Torr), NO_2 (3-20 Torr) and the buffer gas, SF_6 (≈ 1 bar) into the gas cell placed in the sample compartment of a Nicolet Nexus 870 FTIR spectrometer in a dark room. A capacitance gauge (MKS, range 0.01 Torr to 1000 Torr; accuracy ≈ 0.005 Torr) was used for gas pressure determination. O(^{3}P) atoms were generated by a broadband Xenon lamp (350-380nm, 100W) irradiation of NO_2. The lamp was fixed at 2

cm away from the main body of the glass cell. The temperature recorded by a thermocouple attached onto the outer wall of the cell showed an increase of 0.1-0.2 K during irradiation. However the laboratory temperature variation was larger (≈2 K) and hence the reaction temperature was quoted as occurring in the range 301-303 K. A fiber optic cable placed at a fixed position of 1 cm away from the cell was used to direct a small portion of the radiation into an Acton Research monochromator (30 cm focal length) for monitoring the lamp output. The photolysis of the reaction mixture would only be initiated once a constant output of radiation from the lamp could be maintained, as monitored using the fiber optic cable. Unlike a laser, the broadband radiation is not expected to induce multiphoton and secondary processes which might affect the kinetic measurements. Nevertheless, the progress of the reactions under strong and weak irradiation could be easily compared by reducing the lamp power five times (≈20W) but at the expense of a much longer irradiation time. We found that different irradiation power gave the same results for the kinetic runs hence multiphoton processes were kept to a minimum in our experiments. For experiments that required a mercury (Hg) lamp of 254 nm radiation, a quartz cell of similar size (15 cm long, 2.5 cm diameter) was used instead while all other conditions were maintained as usual.

FTIR spectroscopy was used to record the decay and appearance of vibrational bands of reactants and products upon NO_2 photolysis. An IR spectrum (range 1000 to 3500 cm^{-1}; resolution 1 cm^{-1}; average 16 scans) was collected every 1 minute interval. The absorbances of the reactants were kept low (<20%) by adjusting their vapour pressures such that Beer-Lambert's Law could be reliably used to form a linear relationship between absorbance and concentration. Purging of the spectrometer with N_2

was carried out to reduce interference from water and CO_2. This is especially important in experiments for which the appearance rate of CO_2 in the gas cell was to be measured accurately. Whenever possible, we used initial rate measurements to probe the kinetics during the early stages of irradiation. Typically this duration ranged from 0 – 5 minutes or slightly longer if the irradiation power was reduced. Initial rates measurements also served to minimize contributions from secondary reactions caused by product buildup. Each experiment was repeated 4 to 6 times and uncertainty in the rate coefficient or branching ratio was quoted to 3σ deviation.

2.3 Results

2.3.1 Concentration Analysis

Since the measured infrared absorbance, Abs (ν) was related to concentration, c via the Beer-Lambert's Law (Abs(ν) = ε(ν)cℓ for small absorbances, ℓ = 15 cm pathlength), the molar absorptivities, ε(ν) of the molecular vibrational bands need to be known or estimated, especially for studying the main products of the reactions. Although the total vibrational band intensities, I_{vib} values for each vibration of CS_2, CO and OCS have been determined [14], literature search reveals scarce data for the corresponding values for other species under investigation here such as SCSe, OCSe and CSe_2. The lack of data for these species may be due to the difficulty of obtaining pure samples; nevertheless, we have embarked on the calculation of I_{vib} of all relevant species using density functional method B3LYP and a fairly large basis set aug-cc-pvtz in Gaussian 98 [15]. Molecular geometries were also optimized at this level of theory in order to obtain a

good match between the experimental and calculated bond lengths and bond angles. Table 2.1 shows the calculated vibrational frequencies and band intensities as well as the previously determined experimental values, if any, for the molecules under study here. By comparing the experimental and computed intensities, excellent agreement could be found for CO, CS_2 and OCS if an arbitrary scaling factor of 0.81 is applied to the calculated values with a 4.6% discrepancy [$=(1/N)\Sigma(I_{cal}-I_{exp}) / I_{cal}$; N = 4]. A scaling factor of <1 is typical of those used to scale vibrational frequencies as well [14]. The good match gives some confidence in using the scaling factor for molecules for which the I_{vib} have not been determined yet. The band intensity is related to the molar absorptivity, $\varepsilon(\nu)$ by $I_{vib} = \int \varepsilon(\nu)\, \delta\nu$, where $\delta\nu$ is the vibrational bandwidth. Since a typical bandwidth of the molecules here is 20-40 cm^{-1}, we have omitted the small linewidth contributions from the 1 cm^{-1} spectral resolution of the FTIR spectrometer. Thus the concentration can be estimated using the formula,

$$c = (I_{vib}.\ \ell)^{-1} \int Abs(\nu)\, \delta\nu$$

where the integral represents the area under the vibrational band.

TABLE 2.1: The experimental and calculated vibrational frequencies and band intensities (after scaling) for the various molecules investigated here. All the bands here have been used as spectroscopic probes for measurement of rates of reaction

Molecule	Expt. ν* (cm^{-1})	Calc ν (cm^{-1})	Expt I_{vib}** (km mol^{-1})	Calc I_{vib}*** (km mol^{-1})
CO	2143	2207	62	80 (65)
CO_2	2349	2401	530	675 (547)
CS_2	1535	1550	597	684 (554)
CSe_2	1300	1322	-	546 (442)
SCSe	1435	1453	-	626 (507)
OCS	2062	2108	634	763 (618)
OCSe	2034	2075	-	769 (623)

*Except for CO, these values represent the asymmetric stretching vibrational frequencies.
**Reference 14
*** Scaled intensities in parentheses (Factor = 0.81)

For consistency purposes, we have used either the actual experimental value if possible or the scaled calculated values for all molecules in the determination of the rate constants in this work. As discussed later, the determination of many of the rate coefficients were carried out using pseudo first-order approximations which requires only a change in the concentration rather than the absolute value themselves. Hence the error incurred in the band intensity calculations is small except in cases where the branching ratio between molecules such as OCSe and CO is required. The minimum detectable concentration change of a molecular species could also be obtained by monitoring its absorbances as the reaction progressed and converting the values into concentrations using Beer-Lambert's law. Not surprisingly, molecules possessing intense vibrational

bands such as OCS and OCSe have the lowest detection limit of concentration changes of ≈ 0.001 Torr or 3 x 10^{13} molecules cm^{-3}.

As mentioned, experimental errors were quoted to 3σ deviation. However for measurements that required the calculated intensity values such as product yields of OCSe, the error or discrepancy between the calculated and experimental values should be included. For example, the relationship between the errors is given by $(\Delta Z/Z)^2 = (\Delta A/A)^2 + (\Delta B/B)^2$, where ΔZ = overall error in the OCSe yield; Z= average yield; $\Delta A/A$= experimental error in OCSe; and $\Delta B/B$ =0.046, which is the error/discrepancy in calculated intensity.

2.3.2 Reactions of O (^{3}P) with CS_2 and OCS

The reaction of O (^{3}P) with CS_2 was first carried out to test whether our apparatus could be used to obtain reliable rate measurements. It is known that uv photolysis of NO_2 around 360-380 nm gives unit quantum yield of O (^{3}P) atoms [2]. Using flash kinetic infrared spectroscopy, Cooper et al found the [OCS]/ [CO] ratio produced in this reaction to be 2.7 [2]. We have used FTIR spectroscopy to measure the relative rate of appearance of these species by monitoring the evolution of CO (v_{co} = 2143 cm^{-1}) and OCS (v_{ocs} = 2062 cm^{-1}) absorptions. The [OCS] / [CO] ratio was obtained from the relation,

$$R_{CO} = k_{CO} / k_{CS2} = \Delta [CO]_t / \Delta [CS_2]_t$$

$$R_{OCS} = k_{OCS} / k_{CS2} = \Delta [OCS]_t / \Delta [CS_2]_t$$

The linear plot was shown in Figure 2.1. Our initial rate measurements gave an average [OCS]/ [CO] ratio of 2.8 ± 0.2 over a range of NO_2 and CS_2 pressures (5 to 10 Torr each); this is in good agreement with the above literature value.

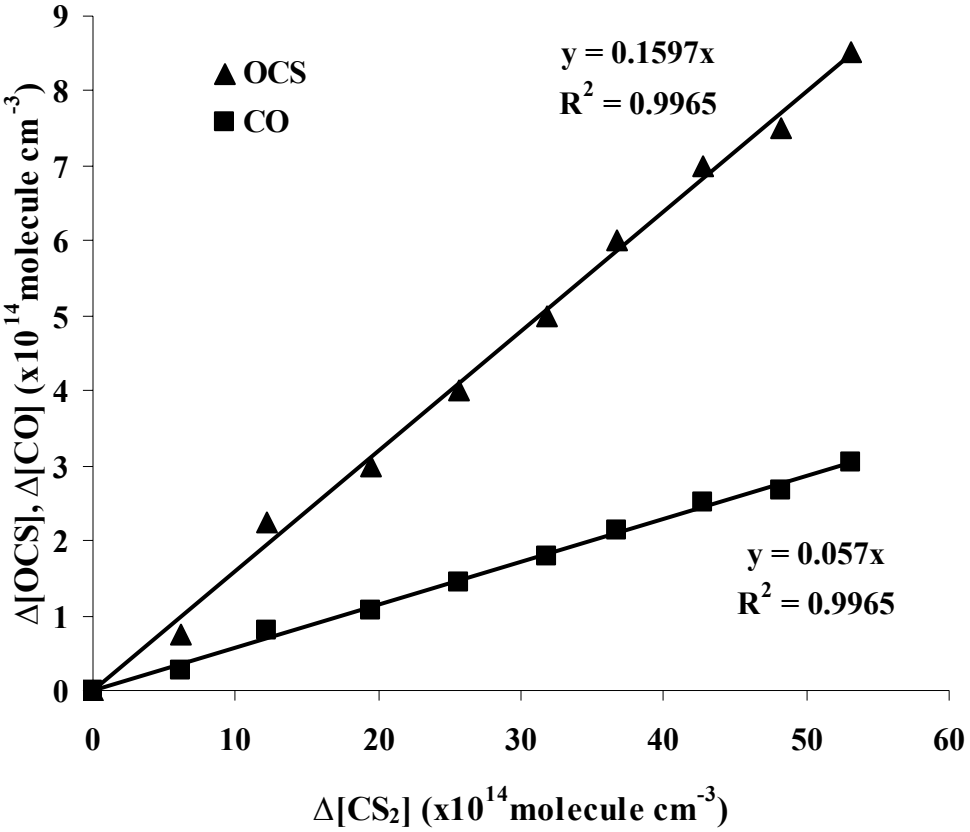

Figure 2.1 Plot of OCS and CO productions vs CS_2 loss during early stages (5-10 minutes) of 360 nm uv lamp photolysis of O/CS_2

In addition, we have also investigated the reaction of O with OCS to determine if CO might have been produced from this reaction. The small value of its rate coefficient (<1 x 10^{-16} $cm^3molecule^{-1}s^{-1}$) [12] implies that CO is not expected to be observed over a short irradiation time. A large pressure of OCS was therefore used with the possibility of generating more CO molecules for detection. However, the CO transitions were still

unobservable despite a few hours of photolysis of 5 Torr NO_2 and 30 Torr of OCS. From these findings, we found that the data collected were consistent with previous studies of these reactions, thus lending support to the reliability of our system for extending the scope of similar reactions.

2.3.3 Reactions of O (^{3}P) atoms with CX_1X_2 (X_1=Se, X_2=O, S or Se)

Upon thermal decomposition of AgNCSe and/or AgNCS, all three carbon chalcogenides could be produced. The production of CS_2 was the most facile and hence its IR signal was generally observed to be the strongest of the three species while SCSe and CSe_2 tend to have similar intensities. Depending on the amount of silver salts used, it was possible to saturate the IR signals of all three chalcogenides. The absorbances of all three infrared bands remained unchanged even after 2 to 3 days indicating their stability towards self and wall decompositions.

Having produced sufficient amount of CSe_2, the reaction of O (^{3}P) atoms with CSe_2 can be subsequently studied in the static cell. A few control experiments were carried out initially to investigate the effect of interference from unwanted reactions. First, the xenon lamp radiation (360-380nm) was directed into a sample containing only CSe_2 but no photodissociation resulted from the process. Second, when NO_2 was added to CSe_2 (5 Torr) in the cell in the absence of photolysis, the IR spectra of CO and OCSe could not be detected or did not increase implying that the reaction of NO_2 with CSe_2 was very slow under our experimental conditions. Since NO is the product of NO_2 photolysis, the effect of mixing an excess of NO (10 Torr) with CSe_2 (5 Torr)) was also examined but no reaction was observed. It was only upon xenon lamp photolysis in the presence of

both NO_2 and CSe_2 that IR signals of CO and OCSe began to increase in intensity with respect to the irradiation time. This observation indicated that it was indeed the O atoms produced from NO_2 photolysis that were responsible for generating CO and OCSe. Figure 2.2 shows a typical IR spectrum taken of the reaction mixture before and after photolysis showing the decay of CSe_2 and appearance of CO and OCSe upon O (^{3}P) atom reactions. The relative rate of appearance of OCSe to CO was measured over a range of NO_2 and CSe_2 pressures, similar to the measurements performed for the O and CS_2 reaction. The linear plots of CO and OCSe production versus CSe_2 loss are shown in Figure 2.3a. It was found that after six sets of experiments, the yields of [OCSe] and [CO] were determined to be (23.0± 4) % and (9.0 ± 1.1)% during the initial stages of irradiation.

The overall reaction rate constants of CSe_2 with O atom could also be measured relative to the reaction between CS_2 and O atom. This was accomplished by deliberately adding CS_2 into the cell containing NO_2 and CSe_2 and allowing both CSe_2 and CS_2 to react competitively with O atoms. Since the rate coefficient of the latter reaction is known previously, the rate coefficient of the former reaction could then be determined. The relative rate k_{CSe2}/k_{CS2} was obtained by observing the logarithmic disappearance of CSe_2 and CS_2 during the initial stages of irradiation. Since the amount of O atoms produced was far less than CS_2 or CSe_2, the reaction proceeds via pseudo-first order kinetics;

$$-\frac{d[CSe_2]}{dt} = k_{CSe2}[O][CSe_2]$$

$$-\frac{d[CS_2]}{dt} = k_{CS2}[O][CS_2]$$

$$\frac{\ln([CSe_2]_0/[CSe_2])}{\ln([CS_2]_0/[CS_2])} = k_{CSe2}/k_{CS2}$$

$$\frac{\ln[(A_{0CSe2}/\varepsilon_{CSe2}l)/(A_{CSe2}/\varepsilon_{CSe2}l)]}{\ln[(A_{0CS2}/\varepsilon_{CS2}l)/(A_{CS2}/\varepsilon_{CS2}l)]} = k_{CSe2}/k_{CS2}$$

$$\frac{\ln(A_{0CSe2}/A_{CSe2})}{\ln(A_{0CS2}/A_{CS2})} = k_{CSe2}/k_{CS2}$$

where the subscript 0 denotes the concentration [X] or absorbance A of species X at time zero (before photolysis). A linear relationship was indeed observed between ln (A_{0CSe2}/A_{CSe2}) and ln (A_{0CS2}/A_{CS2}) and the ratio k_{CSe2} / k_{CS2} was estimated from the initial linear slope of the plots shown in Figure 2.3(b). A value for the overall reaction rate of O with CSe_2, was then determined to be $k_{CSe2} = (1.4 \pm 0.2) \times 10^{-10}$ cm^3 molecule^{-1} s^{-1} after substituting the value for $k_{CS2} = 4.0 \times 10^{-12}$ cm^3 molecule^{-1} s^{-1}[6]. When the rates of change of the three species (CSe_2, OCSe and CO) were compared, a ratio of (100± 2): (23± 4.0): (9.0± 1.1) was obtained for CSe_2: OCSe: CO respectively (with the negative sign indicating a signal decay).

(a)

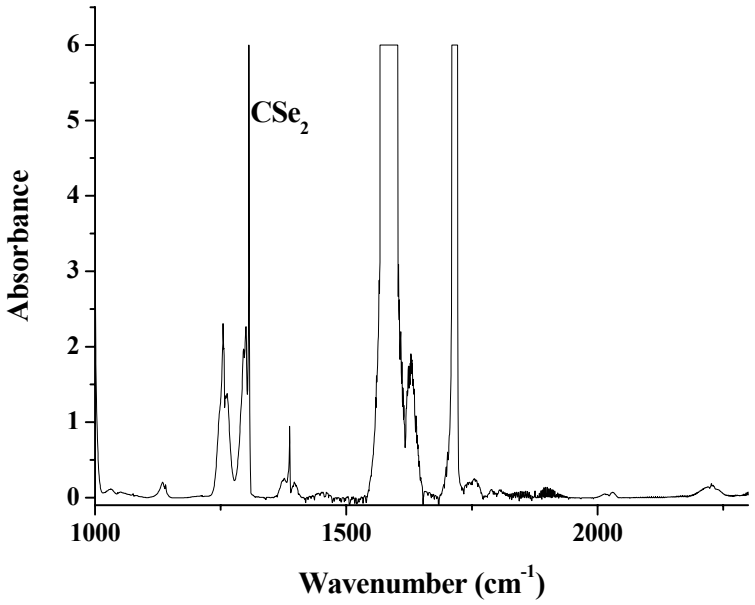

(b)

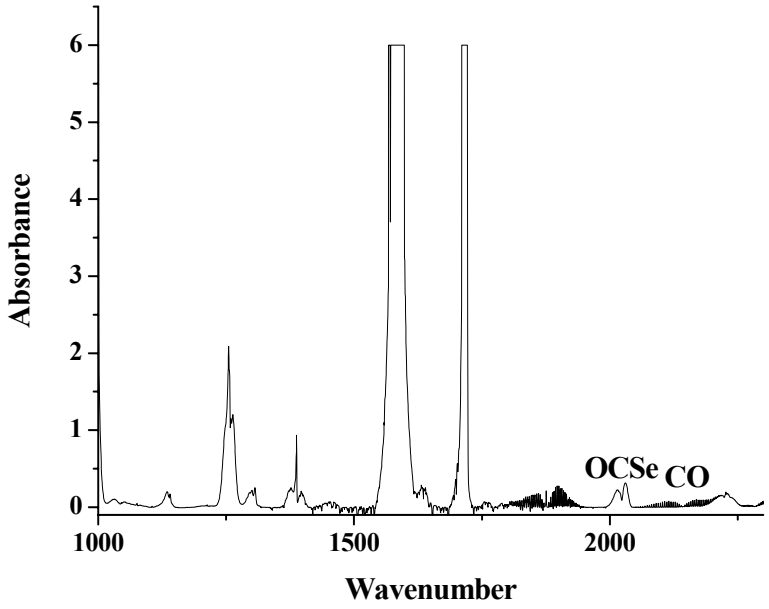

Figure 2.2 FTIR spectrum of CSe_2 (10 Torr) + NO_2 (20 Torr) in SF_6 buffer gas (≈1 bar) before photolysis (a) and after photolysis (b) The CSe_2 infrared signal showed depletion while the appearance of small signals of OCSe and CO could be observed. The intense bands around 1600-1750 cm^{-1} belong to SF_6 and NO_2

(a)

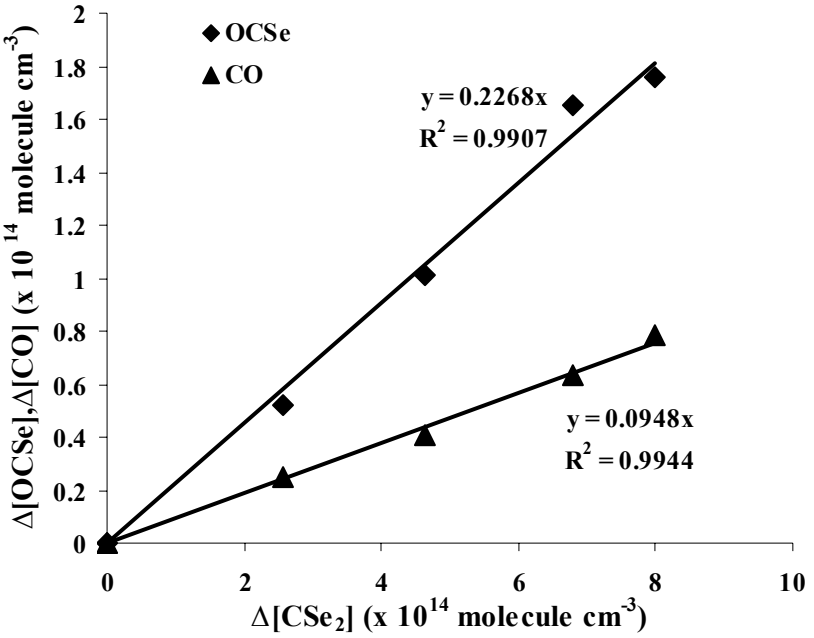

(b)

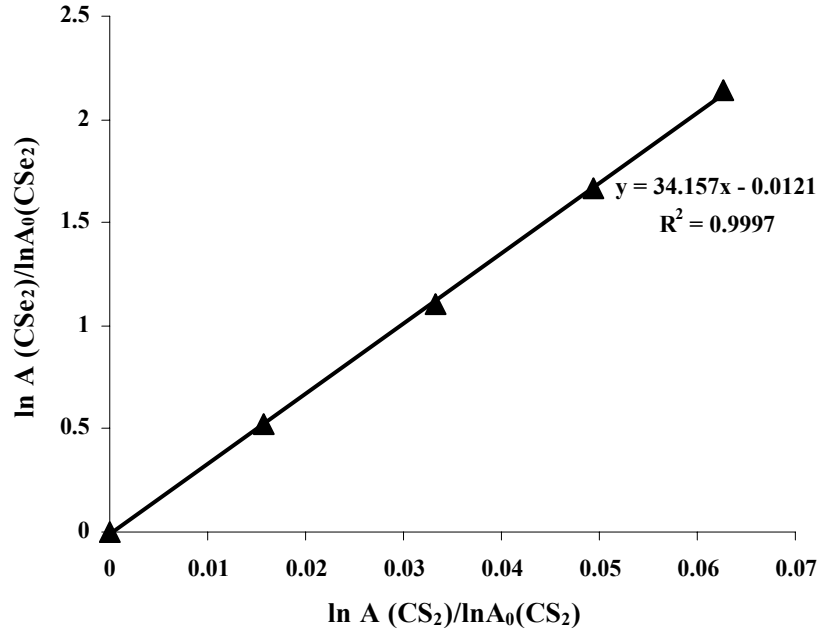

Figure 2.3 (a) Plot of OCSe and CO productions vs CSe_2 loss during early stages (5-10 minutes) of 360 nm uv lamp photolysis of O/CSe_2; (b) Plot of ln A(CSe_2) versus ln A(CS_2) during uv lamp photolysis of O/CSe_2. A linear relationship (denoted by the triangular points) was observed until all the CSe_2 has been completely reacted

The control experiments described earlier for the O/CSe_2 system were also performed for the O/SCSe/CS_2 system. Similar results were obtained whereby it was only upon photolysis of NO_2 in a mixture of CS_2 and SCSe that CO, OCS and OCSe first appeared. Although the production of SCSe was always accompanied by the presence of CS_2, this is advantageous because the competitive reaction of O (^{3}P) with CS_2 may again be used as the internal standard for determining the overall rate coefficient of O (^{3}P) with SCSe.

The decays of equal pressures of SCSe and CS_2 (5 Torr) signals were compared and it was found that SCSe reacted 7 times faster with O atoms, hence with an overall rate constant of $k_{SCSe} = (2.8 \pm 0.3) \times 10^{-11}$ cm^3 molecule^{-1}s^{-1} (Figure 2.4(a)). The unsymmetrical SCSe molecule may react with O (^{3}P) to form either OCS or OCSe. The rate for the production of OCS, OCSe and CO were measured to be about 3, 5 and 10 times slower respectively, if compared against the decay rate of SCSe during the initial stages of irradiation (Figure 2.4(b)). In other words, the [SCSe]: [OCS]: [OCSe]: [CO] ratio could also be expressed as (100 ± 2.2) %: (39.2 ± 5.0) %: (20.2 ± 3.0) %: (12.0 ± 1.0) %. However OCS could also be generated from the reaction of O with CS_2 albeit with a different rate. Since it has been determined that CS_2 decays 7 times slower than SCSe and if the branching ratio for the production of OCS from CS_2 or SCSe is similar, then the OCS contributions from the O/CS_2 system to be ≈14% of the total amount. However it was possible in our experiments to synthesize about 50% more SCSe than CS_2, this reaction mixture was usually used for a better differentiation of the OCS branching ratio. We further estimate the contributions to OCS by CS_2 or SCSe by increasing the ratio of CS_2 to a fixed amount of SCSe in the reaction mixture and remeasuring the OCSe/OCS

ratio again. If the O/CS_2 reaction contributes significantly, the signals of OCS will also increase correspondingly compare to OCSe, which comes only from SCSe. From the

(a)

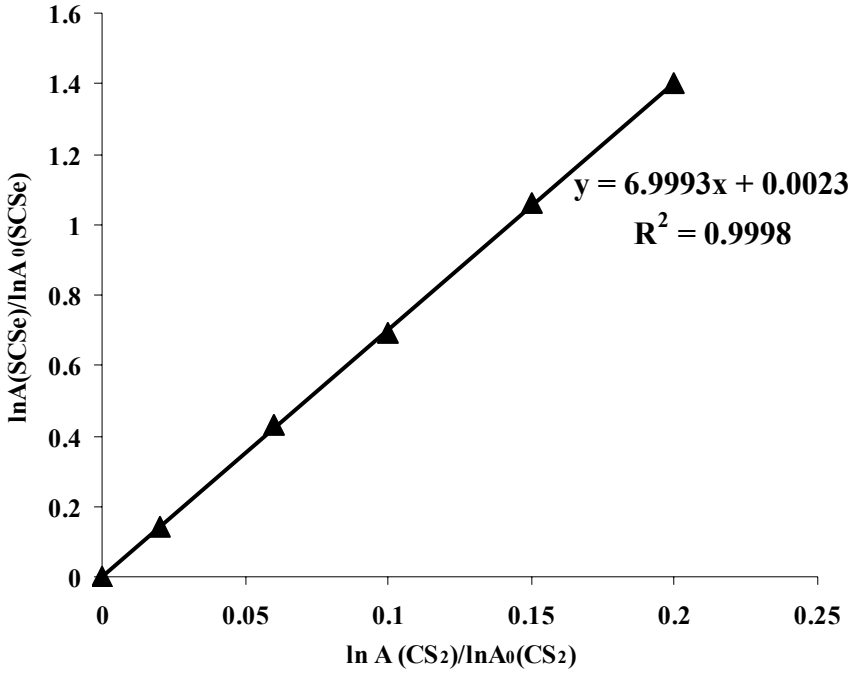

(b)

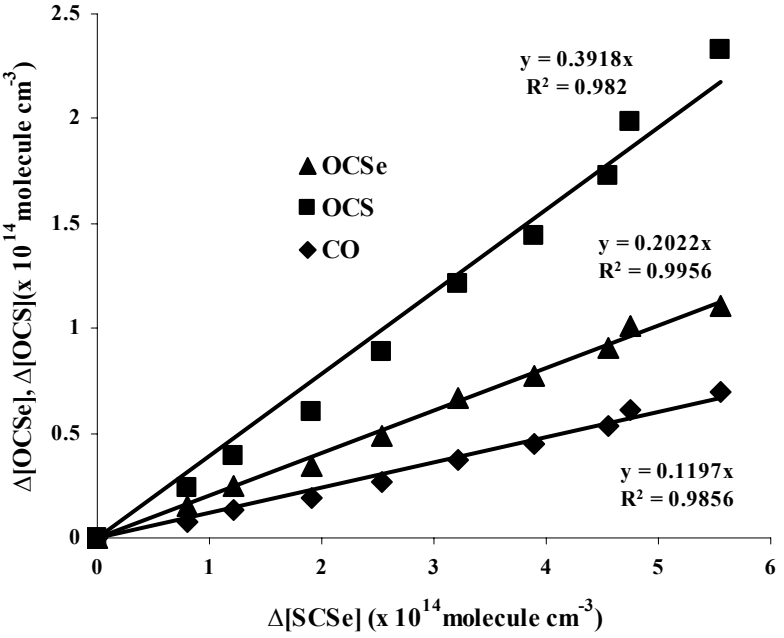

Figure 2.4 (a) Plot of ln A (SCSe) versus ln A (CS_2) during 360nm UV lamp photolysis of O/SCSe. A linear relationship was observed until all the SCSe has been completely reacted. (b) Plots of OCSe, OCS and CO formation vs SCSe decay for the reaction of O + SCSe in the presence of CS_2 during photolysis

results of varying the reactant ratios ranging from [SCSe]/ [CS_2] = 1.5:1 to 1:4, we could revise the overall [SCSe]: [OCS]: [OCSe]: [CO] ratio to be (100 ± 2.2) %: (32.2 ± 4.5) %: (20.2 ±3.0) %: (10 ± 1.0) %.

The importance of secondary reactions involving OCSe was also considered since they could contribute to the generation of CO and perhaps CO_2 upon subsequent reactions with O atoms. The preparation of OCSe free from CSe_2 or SCSe contamination could be carried out in this manner. Starting from a reaction mixture containing CSe_2 and excess NO_2, 254 nm UV irradiation of the sample over time would result in OCSe being formed and CSe_2 being completed reacted. The major components of the gas mixture at the end of the 254 nm irradiation would be NO_2, NO, CO and OCSe. Further photolysis of NO_2 would then allow the reaction of O with OCSe to proceed and its products to be monitored. A known pressure of CS_2 could also be added into the reaction mixture in a separate experiment run so that the rate coefficient of the reaction could be calibrated against k_{CS2}. It was found that the OCSe IR signal decreased further upon reactions with O atoms but at a rate of about 5.8 times slower compared to O and CSe_2 reactions. This resulted in a rate coefficient for the O and OCSe reactions to be $k_{OCSe} = (2.4 \pm 0.3) \times 10^{-11}$ cm^3 $molecule^{-1}s^{-1}$ (Figure 2.5(a)). In addition, only the increase of CO infrared signals (subtracted from CO already present in the mixture) was registered without any detectable formation of CO_2. Interestingly the magnitude of the decay rate of OCSe appeared to be very close to the appearance rate of CO, judging from a near-unity value (0.94) for the gradient of Figure 2.5(b).

(a)

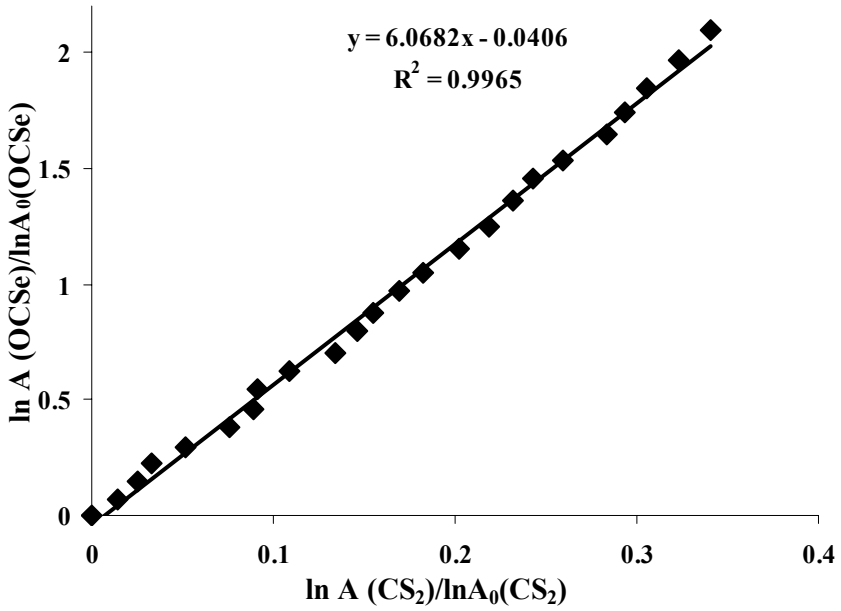

(b)

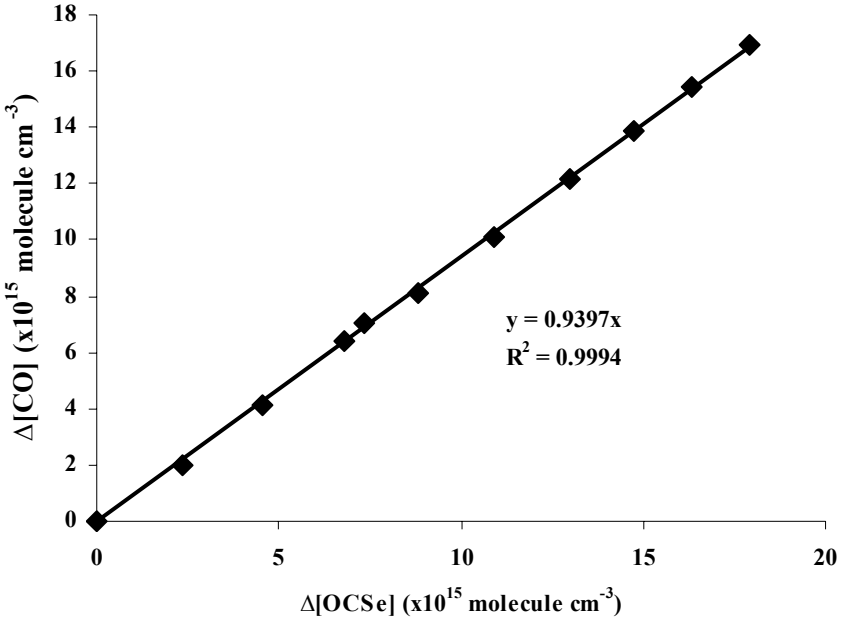

Figure 2.5 (a) Plot showing the decay of OCSe against decay of CS_2 signals upon O atom reactions. (b) Plot of CO production vs OCSe loss during UV lamp photolysis (360-380 nm) of an O/OCSe mixture. No CO_2 was observed during the reaction

2.3.4 Reaction of CSe with O (^{3}P) and O_2

The reactions of CSe between O (^{3}P) and O_2 were investigated too since CSe_2 can be decomposed upon 254 nm light to give CSe and Se atom. For the reaction of CSe with O (^{3}P), about 5 torr CSe_2 and 5 torr NO_2 were photolyzed in SF_6 buffer gas with total pressure about 1 bar. The branching ratios for the production of OCSe and CO were measured to be about (25 ± 3) % and (16 ± 2) % (Figure 2.6(a)). In other words, the [CSe]: [OCSe]: [CO] ratio could also be expressed as (58.9 ± 6) %: (24.7 ± 2) %: (16.4 ± 2) %. The results demonstrate that the production of CO and OCSe is faster than that during the ratios of 360 nm photolysis. In order to check out the contribution from CSe, only the pure CSe_2 was photolyzed at the same condition. The decay curve of CSe_2 was shown in Figure 2.6(b). With NO_2 inside, the decay of CSe_2 is only about 3.5 times faster than that of without NO_2. That may be because there are two kinds of reactions (CSe_2 + O; CSe + O) to contribute the faster decay of CSe_2 and formation of CO and OCSe in the system of 254nm lamp photolysis.

a)

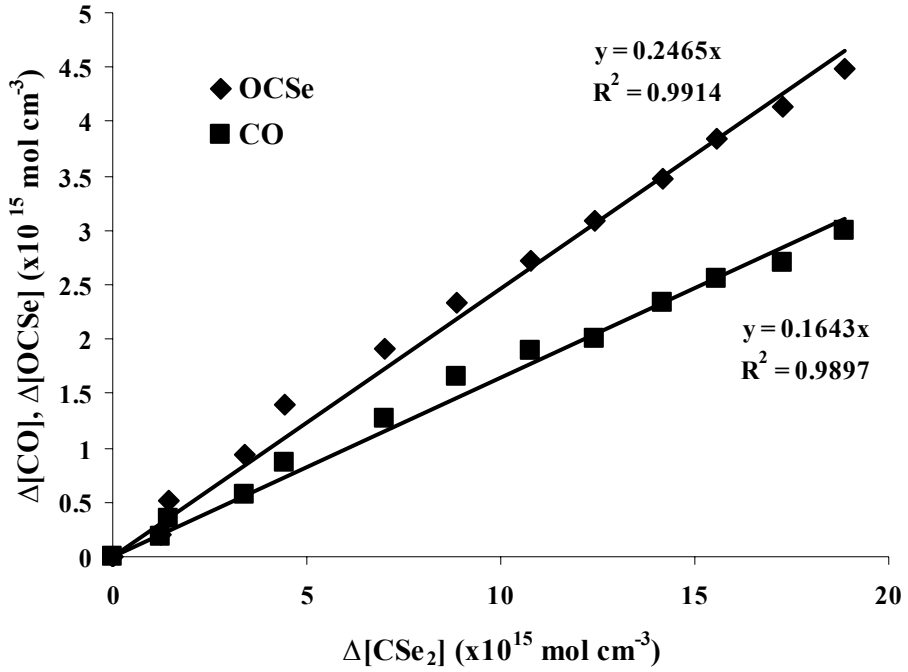

b)

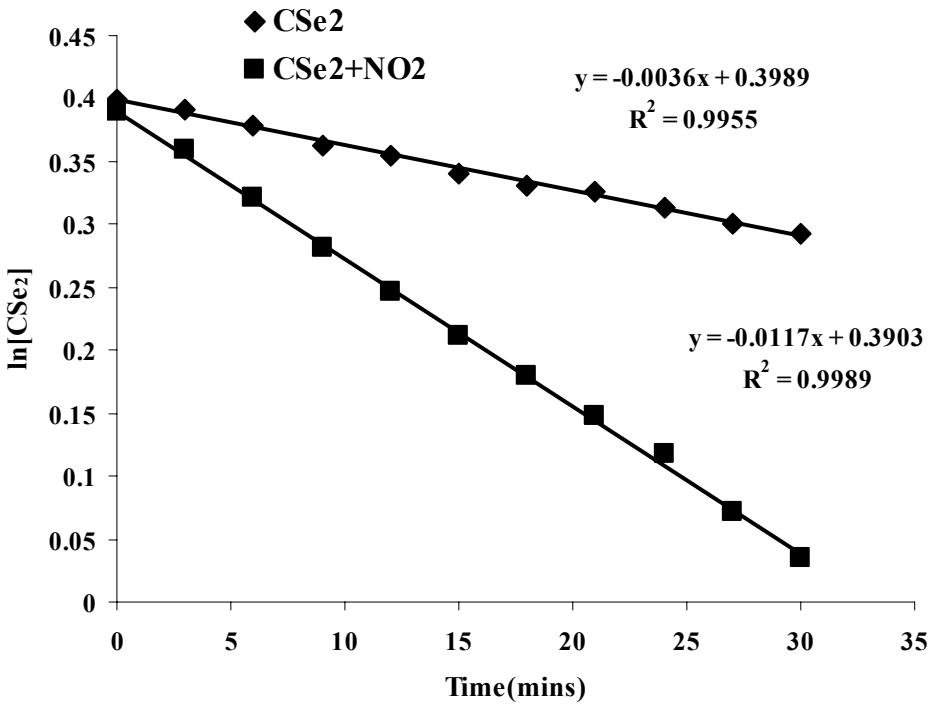

Figure 2.6 (a) Plot of OCSe and CO productions vs CSe_2 loss during early stages (5-10 minutes) of 254 nm uv lamp photolysis of O/CSe_2; (b) Plot of the decay of CSe_2

For the reaction of CSe with O_2, about 1 bar dry air was mixed with 5 torr CSe_2. With photolysis time goes on, the signal of CO and OCSe became bigger and bigger. The observation indicates that CSe can react with O_2 to form O atoms and then the O atoms will react with CSe_2 further to form CO and OCSe. The linear plot of the formation of CO and OCSe versus CSe_2 decay was shown in Figure 2.7. The branching ratio of CO to OCSe is about (3.59 ± 0.3) %: (12.2 ± 1.0) %. The ratio is slight lower than that in the reaction between CSe_2 with O atoms which may be due to the lower O atom concentration in the later system, so the reaction between OCSe with O atoms was slowed down.

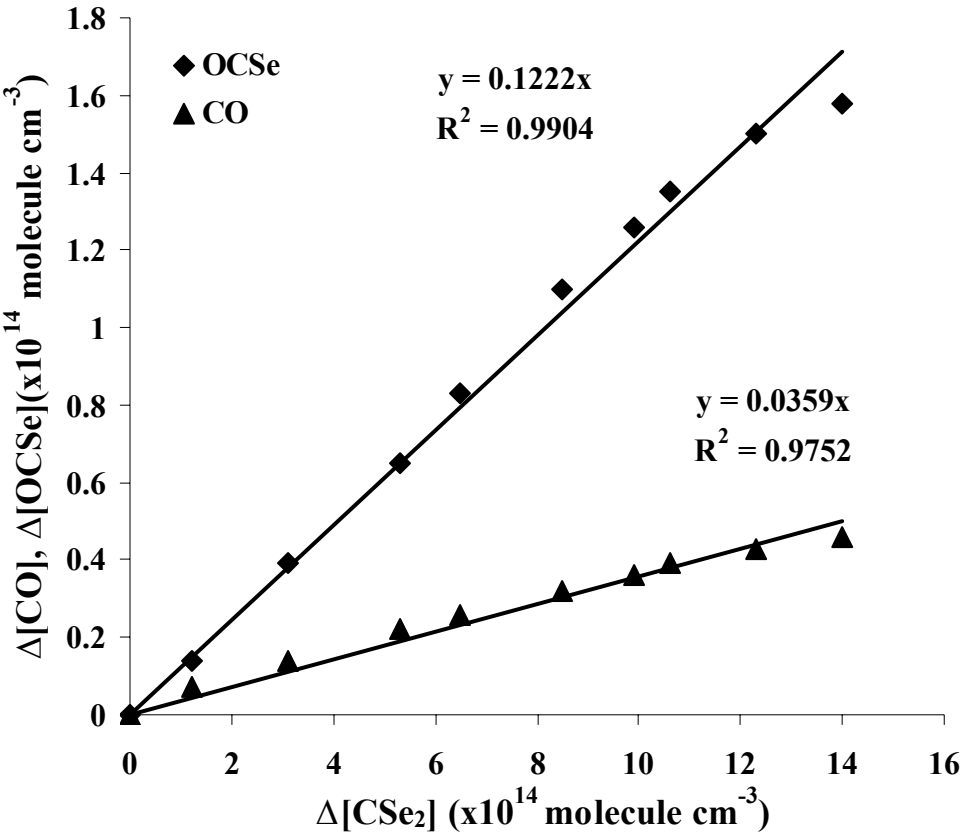

Figure 2.7 Plot of OCSe and CO productions vs CSe_2 loss during early stages (5-10 minutes) of 254 nm uv lamp photolysis of O_2/CSe_2

2.4 Discussion

The reaction rate coefficients k_{CSe2} ((1.4 ± 0.4) × 10^{-10} cm^3 $molecule^{-1}$ s^{-1}) and k_{SCSe} ((2.8 ± 0.3) × 10^{-11} cm^3 $molecule^{-1}s^{-1}$) have been measured to be 34 and 7 times larger than that of k_{CS2} (4.0 × 10^{-12} cm^3 $molecule^{-1}$ s^{-1}); this maybe a result of lower activation barriers for these reactions. Qualitatively, it is not surprising to observe increase in rates since the C=Se bond of CSe_2 or SCSe is weaker than the C=S bond of CS_2 and hence yielding relatively lower energy transition states as well. Because of the weaker C=Se bond, the O and OCSe (k_{OCSe} = (2.4 ± 0.3) × 10^{-11} cm^3 $molecule^{-1}s^{-1}$) reaction is also observed to proceed much faster than the corresponding O and OCS reaction (k < 1.0 x 10^{-16} cm^3 $molecule^{-1}s^{-1}$). Evidence gathered by the excellent match between the decay rate of OCSe with the appearance rate of CO up on O atom reactions suggests that only a single channel is open and the measured rate coefficient may be used to describe the single reaction, O + OCSe → CO + SeO.

Two products from the O/CSe_2 system were detected i.e. OCSe and CO with the former being more abundant with product yields of (23.0 ± 4)% compared to (9.0 ± 1.1)%. However, from the experimental data, the rate of change of the concentrations for CSe_2, OCSe and CO could be described by the ratio (100±3.0): (23.0 ± 4): (9.0 ± 1.1). The combined appearance rates of OCSe and CO are thus only a fraction i.e. 23.0 % + 9.0% = 32.0% of the CSe_2 decay rate. This certainly implies that at least another product channel is open for the O/CSe_2 system. By analogy to reaction 1(a) of the O/CS_2 system, the channel could be attributed to O (^{3}P) + CSe_2 → CSe + SeO. The large discrepancy in the above measured rates would suggest that the production of CSe and SeO is the main

reaction channel. The ratio of products generated by the O/CSe_2 system could then be expressed as CSe: OCSe: CO = (68 ± 5.0) %: (23.0 ± 4.0) %: (9.0 ± 1.1) %.

It is tempting at this stage to ascribe three reaction channels (represented by CSe, OCSe and CO products) for the O/CSe_2 system, similar to those observed for the O/CS_2 system. However OCSe continues to react further with O atoms to yield exclusively CO with a rather large rate coefficient. This is certainly unlike the O/CS_2 system where the slow reaction between O and OCS does not contribute significantly to the production of CO. For clarity sake, the possible reactions in the O/CSe_2 system may be written as;

$O(^3P) + CSe_2 \rightarrow CSe + SeO(^3\Sigma^-)$ 2(a)

$\rightarrow CO + Se_2(^3\Sigma^-_g)$ 2(b)

$\rightarrow OCSe + Se(^3P)$ 2(c)

$O(^3P) + OCSe \rightarrow CO + SeO$ 3

The CO production could come from reactions 2(b) and 3. In order to determined the relative importance of these two channels, the O atom concentrations need to be estimated first. This can be accomplished by examining the rate of decay of CSe_2 during the early stages of irradiation (see Figure 2.8) where;

$$d[CSe_2]/dt = -k_{CSe2}[O][CSe_2]$$

The concentration change of CSe_2 could be estimated by drawing a tangent to its decay curve at certain time intervals and since both k_{CSe2} and $[CSe_2]$ are known, the O atom concentration could then be determined. Calculations carried out at three different early times as indicated in Figure 2.8 gave an average value of [O] = (5.0 ± 0.5) x 10^7 cm^{-3}. As expected, the concentration is rather low because of the low power irradiation used for

the experiments. The CO contribution from the O/OCSe reaction could be approximated now that the O atom concentration is known. We first assume that all CO came from this reaction, thereby ignoring reaction 2(b);

$$d[CO]/dt = k_3[O][OCSe]$$

Since k_3 has been measured and both [OCSe] and d[CO]/dt can be evaluated directly from Figure 2.8, the values for the left hand and right hand sides of the equation can be compared at different times of the reaction. When comparisons were made for three different times as indicated in the graph, it turns out that the left and right hand side values were equal and thus the reaction of O with OCSe could fully account for the production of CO! If this were the case, reaction 2(b) is at most a minor channel based on this analysis. Since some OCSe have reacted further to generate all the CO detected in the system, the branching ratio of reaction 2(c) would have been underestimated and hence, it should be revised accordingly to include the CO contributions to 23.0%+9.0% = 32.0%.

Similar analysis could also be carried out on the O/SCSe system. The product ratio of [OCS]: [OCSe]: [CO] has been found to be (32.2 ± 4.5) %: (20.2 ±0.3) %: (10 ±1.0) %. The probability of direct CO production from O and SCSe reaction is again in doubt. As usual, the [O] concentration could be determined to be 4.5 x 10^7 cm^{-3} from the early stage of irradiation for a NO_2(15Torr)/SCSe(7 Torr)/CS_2 (9Torr) mixture. Indeed, for the given concentration of [O], it appears that the O + OCSe secondary reactions could fully account for the entire CO produced during the initial stages of photolysis. Thus, the ratio of [OCS]: [OCSe]: [CO] is revised to 1.6: 1.5: ≈ 0. However the total appearance rate of these species could only account for 62% of the decay rate of SCSe.

Similar to the O/CS_2 system, two other product channels could be assigned to the production of SeO and CS, and SO and CSe. Unfortunately the relative importance of the two channels could not be separately determined here; hence only one branching ratio of 38 ± 5% will be used to describe the contribution of these channels.

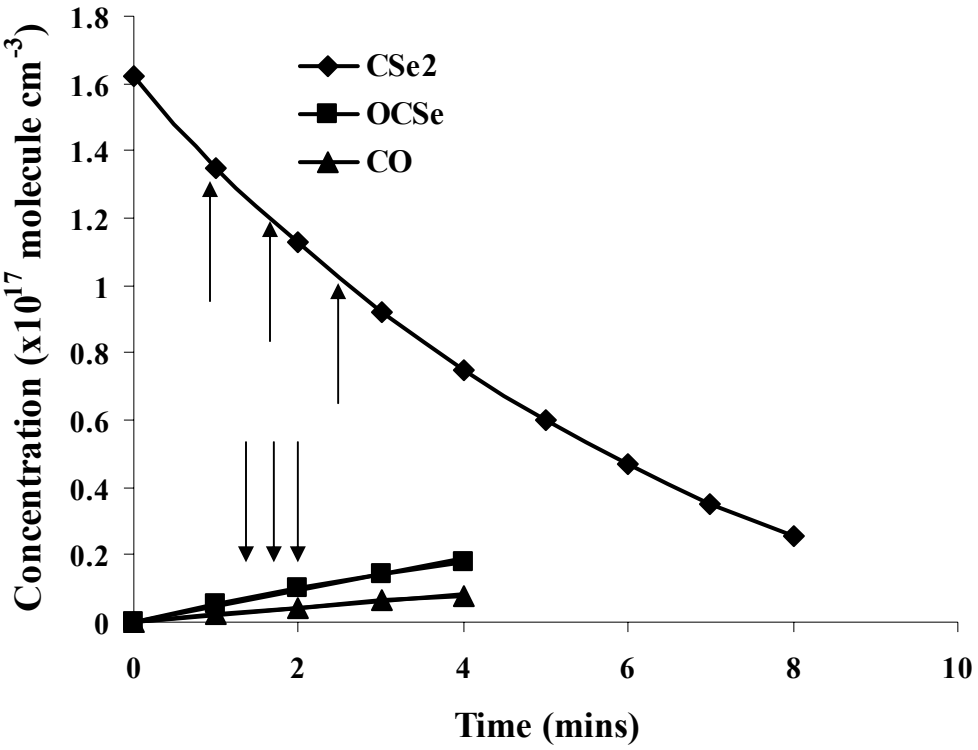

Figure 2.8 Plots of CSe_2, OCSe and CO concentrations as a function of photolysis time in a reaction mixture containing 5 Torr CSe_2, 10 Torr NO_2. Arrows pointing upwards indicate the tangents drawn for the estimation of O atom concentration. Arrows pointing downwards indicate the sampling of 3 different times for the estimation of the contribution of O/OCSe reaction to CO production

2.5 Computational studies

Ab initio computational studies have been performed using Gaussian 98 to further understand and substantiate the experimental findings. Since OCSe has been detected as the main observable product in this work, we place emphasis on the computation of the

1(c), 2(c) and related reaction pathways for the O/SCSe system. The density functional theory (DFT) method of UB3LYP with aug-cc-PVTZ basis sets has been used for the optimization of the structures and energies of reactive intermediates and transition states in all the reactions of O (^{3}P) with CS_2, CSe_2 and SCSe (Table 2.2) [16].

Comparisons with the experimental values of the enthalpies of formation of the three channels of the O/CS_2 system were first made to check the reliability of the calculations. As shown in Figure 2.9, the reaction pathway leading to OCS and S (channel 1c) has been calculated for the O/CS_2 system on a triplet potential energy surface. The calculated enthalpy of formation, ΔH_r of the overall reaction is -235 kJ mol^{-1} which puts it in very good agreement with previously determined experimental values [2]. Several intermediates or transition states were found along this pathway as well. The first optimized transition state **A** depicts the oxygen atom approaching CS_2 at an ∠OCS angle of about 79^o. Despite several attempts, we have been unable to find an optimized structure in which the O atom is directed perpendicularly (∠OCS=90^o) towards the C atom. Incidentally, a bent transition state rather than a collinear one was also found previously for the primary channel 1(a) [3]. An earlier study showed that the average kinetic energy of the O(^{3}P) atom following 355 nm photolysis corresponding to NO($X^2\Pi$, v=0) state was 1833 cm^{-1} [15]. As the calculated activation energy turns out to be about 23 kJ mol^{-1} (1922 cm^{-1}), it is just low enough for the reaction to take place at rates measurable over a short time under our experimental conditions. Not surprisingly, this value is higher than the activation energy of the primary channel 1(a), which was estimated to be about 420 cm^{-1} [16]. The transition state structure also shows that the two sulfur atoms of the CS_2 moiety have bent away from the incoming O atom and will

eventually lead to the intermediate COS_2 denoted as **B**. This intermediate **B** which sits in a relatively deep potential energy well (250 kJ mol^{-1}) with respect to structure **A** is also believed to be the precursor to channel 2(b) where CO and S_2 are produced [2]. The C=O bond distance of 1.19Å for **B** is only slightly longer than a typical carbonyl bond of organic molecules (1.15-1.17 Å). Further along the pathway, a second transition state **C** was found in which one of the C=S bond lengthens as the sulfur atom of that bond begins to pull away, leaving behind an OCS moiety which has a quasilinear structure with an obtuse angle of 154^o. The dissociative C-S bond distance at 2.28 Å is considered rather long but consistent with **C** being a late transition state and hence product-like in structure.

As expected, similar transition states and intermediates of the reaction pathway were also computed for the O/CSe_2 system with ΔH_r value of -323 kJ mol^{-1} (Figure 2.10). The first activation energy leading to structure **D** for this system is only 2.1 kJ mol^{-1}. This almost barrierless reaction explains the experimental data in which the production of OCSe from CSe2 is >37 times faster than the production of OCS from CS_2. The transition states, **D** and **F** also closely resemble their sulfur counterparts in structure. The intermediate $COSe_2$ denoted by **E** occupies a deep potential well relative to **D** and forms the lowest energy state of the reaction pathway for the O/CSe_2 system.

TABLE 2.2: Optimized structures and vibrational frequencies of the intermediates and transition states in the O/CS_2, O/SCSe and O/CSe_2 systems determined at UB3LYP/aug-cc-PVTZ level of theory. The imaginary frequencies of the transition states are denoted by i

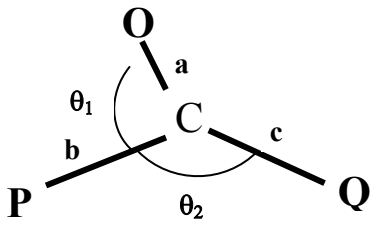

Structure	P, Q	a, b, c (Å)	θ_1, θ_2	Vibrational frequencies (cm^{-1})
A	S,S	1.95, 1.61,1.56	79°, 162°	431i, 247, 328, 402, 635, 1429
B	S,S	1.19, 1.78, 1.78	133°, 94°	289, 381, 508, 547, 606, 1798
C	S,S	1.16, 2.28, 1.64	119°, 87°	307i, 222, 394, 503, 750, 1992
D	Se,Se	2.07, 1.69, 1.75	76°, 165°	354i, 193, 242, 326, 378, 1240
E	Se,Se	1.18, 1.94,1.94	133°, 94°	178, 279, 450, 459, 495, 1812
F	Se,Se	1.16, 2.49, 1.79	118°,87°	228i, 137, 321, 450, 561, 1993
G	S,Se	1.98, 1.56, 1.72	97°,170°	473i, 177, 262, 334, 493, 1349
H	S,Se	1.18,1.72, 2.03	139°,93°	209, 261, 457, 489, 666, 1830
I	S,Se	1.17, 2.30, 1.65	121°, 90°	211i, 205, 374, 492, 727, 1945
J	Se,S	1.15, 2.43, 1.78	117°, 84°	265i, 164, 348, 457, 576, 2020
K	Se,O	2.03, 1.75, 1.16	57°, 179°	395i, 361, 469, 637, 690, 2106

For the O/SCSe system shown in Figure 2.11, the enthalpies of reaction for the production of OCSe and S and for the production of OCS and Se have been determined to be -238 kJ mol^{-1} and -318 kJ mol^{-1} respectively. Interestingly, these values are very close to the corresponding values for the O/CS_2 and O/CSe_2 systems, indicating that the strength of a particular C=S or C=Se bond is almost the same in any of the carbon chalcogenides. The calculated activation barrier leading to its first transition state **G** is 9.3 kJ mol^{-1}, which is in between the values for the O/CS_2 and O/CSe_2 systems. This again agrees with the experimental data in which decay of SCSe to OCS and OCSe is intermediate in rate compared to CS_2 and CSe_2. The transition state shows the O atom being located at almost right angle to the SCSe moiety. The intermediate COSeS denoted by **H** also possesses a relatively deep potential well although this time it is no longer the lowest energy state of the reaction pathway. Further along the pathway, we managed to locate two more transition states, **I** and **J** which correspond to either the cleavage of the C-S bond to produce OCSe or the cleavage of the C-Se bond to produce OCS. As expected, the latter transition state, **J** is energetically lower by 53 kJ mol^{-1} since cleavage of the weaker C=Se bond is easier to achieve. However both transition states **I** and **J** are still lower in energy compared to **G** and may not play a critical role in determining the OCS/OCSe branching ratios. Experimental observations showed that the appearance rate of OCS is only slightly higher than the corresponding rate for OCSe.

Rochford et al. has indicated from the transition state structure that an angular attack of the O atom on OCS has taken place with an activation barrier of 24 kJ mol^{-1} for the production of CO and SO [6]. We have also assumed similar reaction pathways for the reaction of O with OCSe. Unfortunately an optimized transition state structure could

not be found despite a few attempts. Nevertheless, it is not surprising to expect the barrier to be lower than the O/OCS case by virtue of the weaker C=Se bond. Hence the reaction of O with OCSe should proceed much faster and in fact account for CO production in the system. However, CO_2 and Se may also be generated from the reaction of O with OCSe with a large release of energy (ΔH_r = 375 kJ mol^{-1}, also computed using UB3LYP/aug-cc-PVTZ). By virtue of its exothermicity, this channel could be deemed important although CO_2 could not be observed in the experiment. Hence, the same UB3LYP/aug-cc-PVTZ computations were carried out to trace its reaction pathway and indeed, the transition state **K** was found to be located at about 85 kJ mol^{-1} higher than the reactants O and OCSe. The large value for the activation barrier appears to have hindered the formation of CO_2 under our experimental conditions.

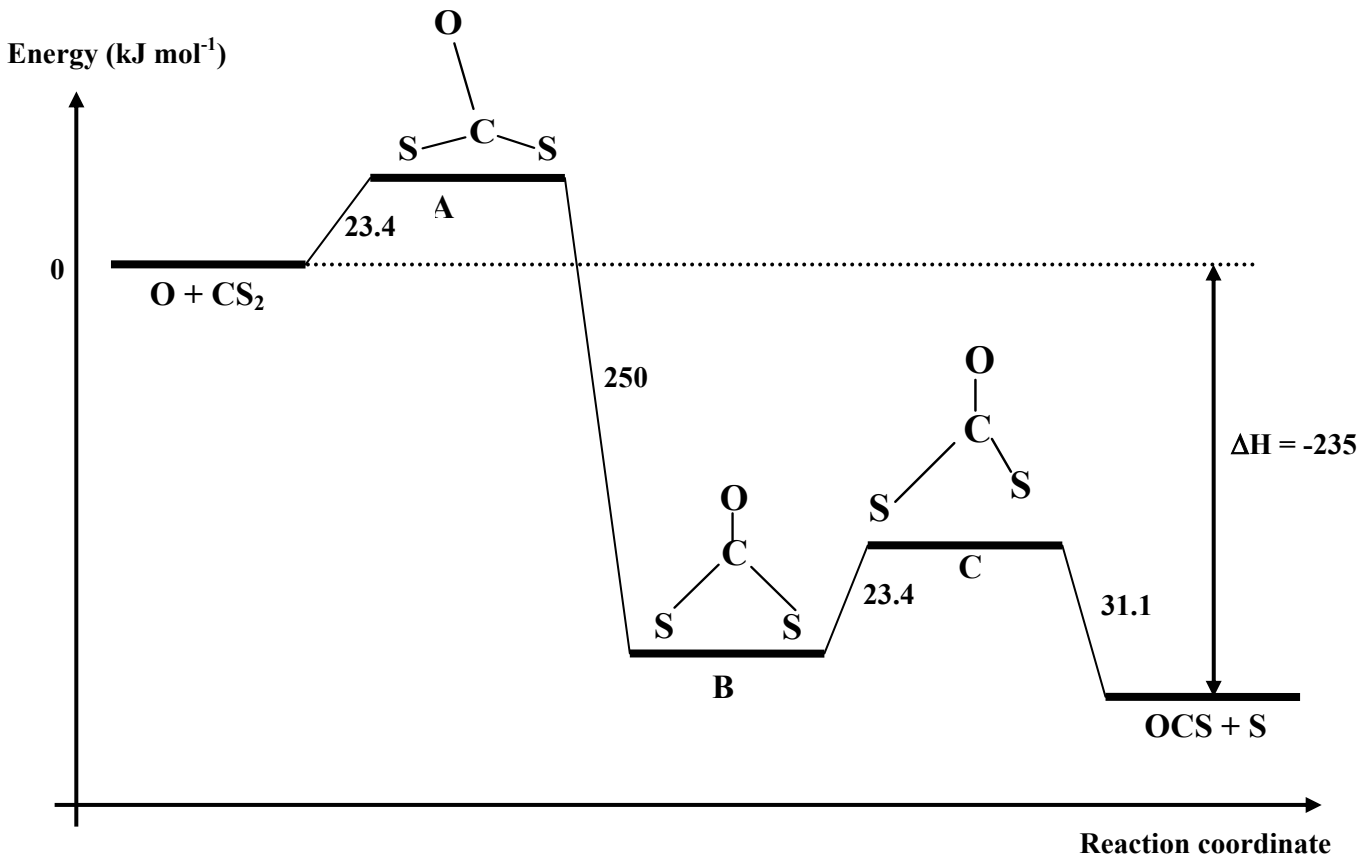

Figure 2.9 Energy level diagram for the O(^{3}P) + CS_2 → OCS + S(^{3}P) potential energy surface showing the intermediate and transition states computed at UB3LYP/aug-cc-PVTZ level of theory

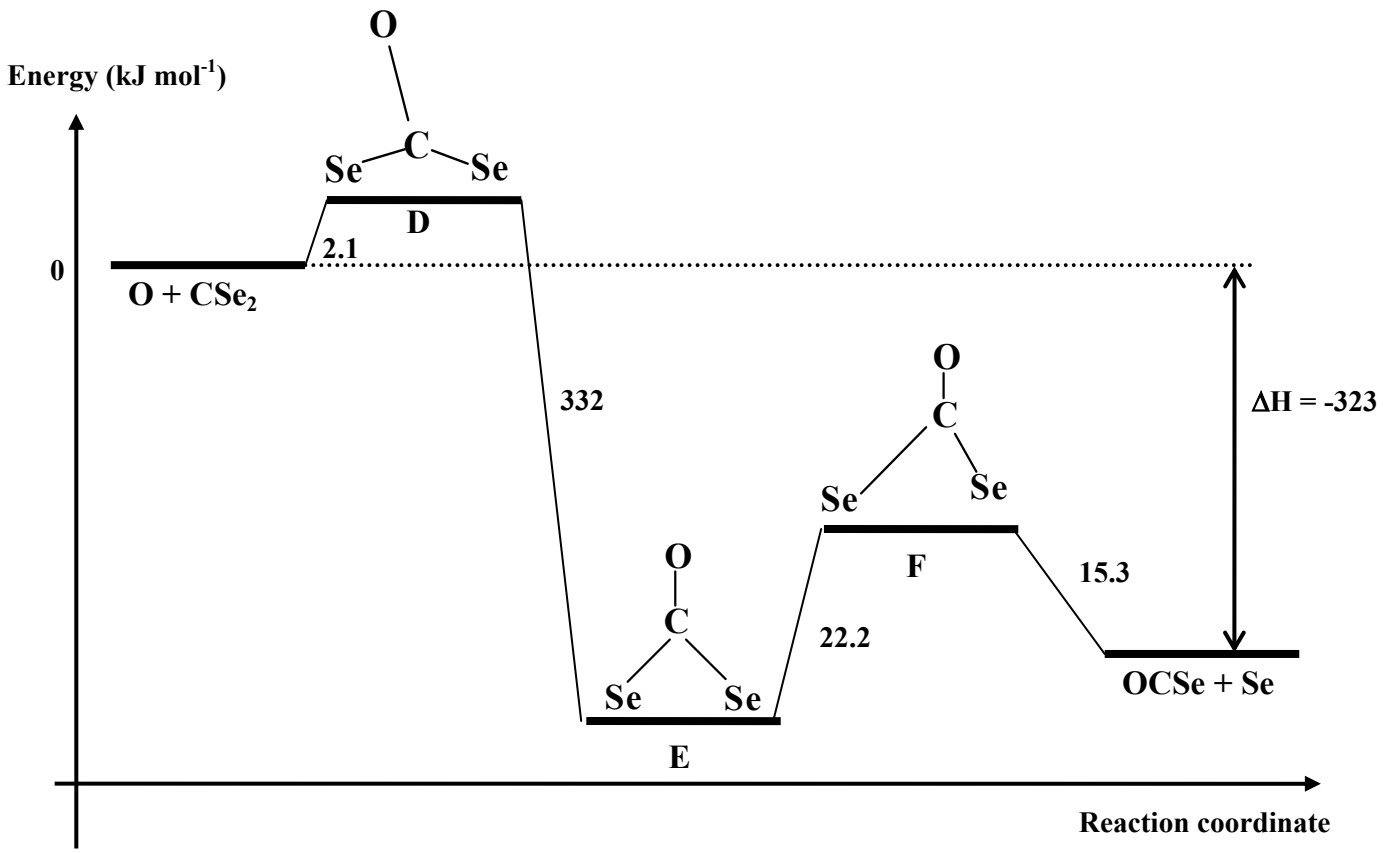

Figure 2.10 Energy level diagram for the O(^{3}P) + CSe_2 → OCSe + Se(^{3}P) potential energy surface showing the intermediate and transition states computed at UB3LYP/aug-cc-PVTZ level of theory

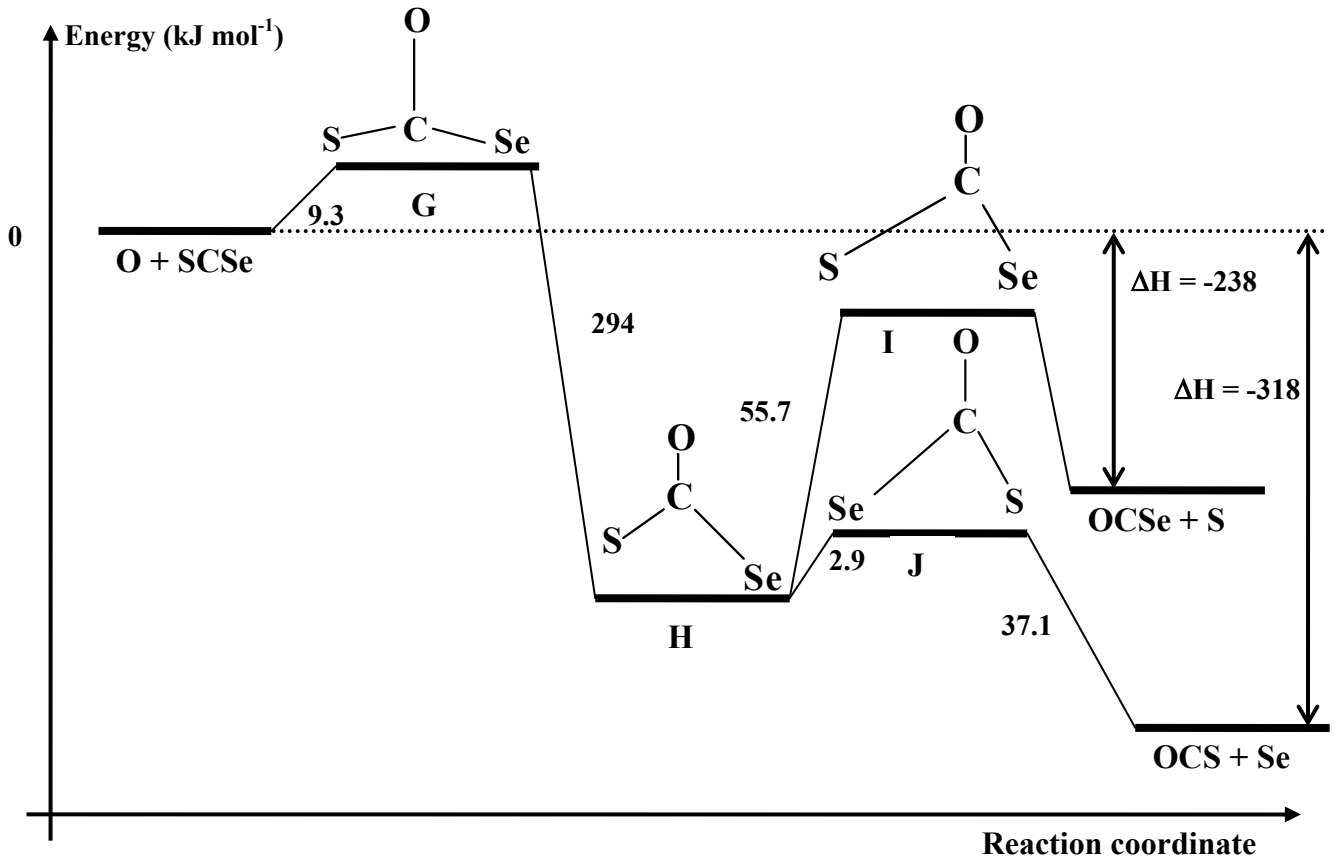

Figure 2.11 Energy level diagram for the O (^{3}P) + SCSe → OCS + Se (^{3}P) and OCSe + S(^{3}P) potential energy surfaces showing the intermediate and transition states computed at UB3LYP/aug-cc-PVTZ level of theory

2.6 Summary

We have determined the rate coefficients of the reactions of the carbon chalcogenides, CSe_2, SCSe and OCSe with O(^{3}P) atom to be $k_{CSe2} = (1.4 \pm 0.2) \times 10^{-10}$ cm^3 molecule^{-1} s^{-1}, $k_{SCSe} = (2.8 \pm 0.3) \times 10^{-11}$ cm^3 molecule^{-1} s^{-1} and $k_{OCSe} = (2.4 \pm 0.3) \times 10^{-11}$ cm^3 molecule^{-1} s^{-1} at 301-303K using the technique of Fourier-Transformed Infrared (FTIR) absorption spectroscopy. These measurements have been carried out by using the known value of the rate coefficient for O (^{3}P) with CS_2 (4 x 10^{-12} cm^3 molecule^{-1} s^{-1}) as the internal calibrant. Two main product channels yielding CSe and OCSe respectively have been found for the O + CSe_2 reaction, similar to the O/CS_2 system. CO was also observed in the O/CSe_2 system although its generation could be attributed to subsequent reactions of OCSe with O atoms. The corresponding reaction for O + SCSe gives roughly equal amount of OCS and OCSe as products. However the dominant channel is still inferred to be the one that produces CSe and SO, and CS and SeO with the branching ratios of CSe/CS: OCS: OCSe: CO = (38 ± 5.0) %: (32.2 ± 5.0) %: (20.2 ± 3.0) %: (10 ± 1.0) %. Density functional methods such as UB3LYP/aug-cc-PVTZ have been used to determine the reaction pathways for the channels in which OCS or OCSe is produced. The rate coefficients or product concentration ratios in their final are listed in Table 2.3 together with the previously determined rates from the O/CS_2 and O/OCS systems.

TABLE 2.3: Rate coefficients and branching ratios measured for the reactions of O (^{3}P) atoms with CS_2, CSe_2, SCSe, OCSe, CSe and CSe with O_2

No	Reaction	Rate coefficient ($cm^3molecule^{-1}s^{-1}$)	Ratio of products[#]
1	$O(^3P) + CS_2 \rightarrow$ products*	4.0×10^{-12}	[OCS]/[CO] = 2.8
2	$O(^3P) + OCS \rightarrow CO + SO$**	$<1.0 \times 10^{-16}$	-
3	$O(^3P) + CSe_2 \rightarrow$ products	$(1.4 \pm 0.2) \times 10^{-10}$	[CSe]:[OCSe]:[CO] = (68.0 ± 5.0)%: (23.0 ± 4.0)%: (9.0± 1.1)%
4	$O(^3P) + SCSe \rightarrow$ products	$(2.8 \pm 0.3) \times 10^{-11}$	[CSe/CS]:[OCS]:[OCSe]:[CO] = (38.0 ±5)%: (32.2 ± 4.0)%: (20.2 ± 3.0)% : (10.0± 1.0)%
5	$O(^3P) + OCSe \rightarrow CO + SeO$	$(2.4 \pm 0.3) \times 10^{-11}$	[CO] ≈ 100%
6	$CSe + O(^3P)$	-	[CSe]: [OCSe]:[CO] = (58.9 ± 6)%: (24.7 ± 2)%: (16.4 ± 2)%
7	$CSe + O_2$	-	[CO]: [OCSe] = (3.59 ± 0.3)%: (12.2 ± 1.0)%

[#]The ratios quoted here are the ones where the effects of secondary reactions have been taken into account. Thus they are not necessarily the raw experimental values.

*Reference 2

**Reference 12

Reference

1. G. S. Tyndall and A. R. Ravishankara, Int. J. Chem. Kinet., 23, 483, 1991

2. W. F. Cooper and J. F. Hershberger, J. Phys. Chem., 96, 5405, 1992

3. Y. Cheng, J. Han, X. Chen, Y. Ishikawa and B. R. Weiner, J. Phys. Chem. A., 105, 3693, 2001

4. Y. Murakami, M. Kosugi, K. Susa, T. Kobayashi and N. Fujii, Bull. Chem. Soc. Japan 74, 1233, 2001

5. C. N. Wei and R.B. Timmons, J. Chem. Phys., 62, 3240, 1975

6. J. J. Rochford, L. J. Powell and R. Grice, J. Phys. Chem., 99, 15369, 1995

7. P. D. Naik, U. B. Pavanaja, A. V. Sapre, K. V. S. Ramarao and J. P. Mittal, Chem. Phys. Lett., 186, 565, 1991

8. I.W.M. Smith, Faraday Soc. Discuss., 43-44, 194, 1967

9. C. Morley, B. A. Ridley and I. W. M. Smith, J. Chem. Soc. Faraday Trans 2, 68, 2127, 1972

10. W. H. Pan and J. P. Jr. Fackler, Inorg. Synth., 21, 6, 1982

11. L. Henriksen, Synth., 2, 204, 1985

12. NIST Standard Reference Database No 69, March, 2003 Release at http://webbook.nist.gov/chemistry

13. A. B. Callear and W. J. R. Tyerman, Trans. Faraday Soc., 61, 2395, 1965

14. "Molecular Spectroscopy: Modern research", Eds. K. N. Rao and C. W. Mathews, NY Academic Press, Vol.2. p179, 1972-1985

15. M. J. Frisch, G. W. Trucks, H. B. Schlegel, G. E. Scuseria, M. A. Robb, J. R. Cheeseman, V. G. Zakrzewski, Jr. J. A. Montgomery, R. E. Stratmann, J. C. Burant, S. Dapprich, J. M. Millam, A. D. Daniels, K. N. Kudin, M. C. Strain, O. Farkas, J. Tomasi, V. Barone, M. Cossi, R. Cammi, B. Mennucci, C. Pomelli, C. Adamo, S. Clifford, J. Ochterski, G. A. Petersson, P. Y. Ayala, Q. Cui, K. Morokuma, D. K. Malick, A. D. Rabuck, K. Raghavachari, J. B. Foresman, J. Cioslowski, J. V. Ortiz, A. G. Baboul, B. B. Stefanov, G. Liu, A. Liashenko, P. Piskorz, I. Komaromi, R. Gomperts, R. L. Martin, D. J. Fox, T. Keith, M. A. Al-Laham, C. Y. Peng, A. Nanayakkara, C. Gonzalez, M. Challacombe, P. M. W. Gill, B. Johnson, W. Chen, M. W. Wong, J. L. Andres, C. Gonzalez, M. Head-Gordon, E. S. Replogle and J. A. Pople, *GAUSSIAN 98*, Gaussian Inc., Pittsburgh, PA, 1998

16. D. S. Y. Hsu, W. M. Shaub, T. L. Burks and M. C. Lin, Chem. Phys., 44, 143, 1974

– CHAPTER 3 –

Laser-induced decomposition of fluoronitrites

3.1 Introduction

The harmful effect due to the presence of chlorofluorocarbons (CFCs) in the atmosphere has led to an extensive search for their replacement by more environmentally-acceptable compounds such as hydrofluorocarbons (HFCs) and hydrochlorofluorocarbons (HCFCs) [1]. Although they have similar physical properties to CFCs, their significantly shorter atmospheric lifetimes make them suitable as alternatives. Among the main HFCs under consideration are molecules containing CF_3 groups with the general formula CF_3CHXY (X, Y = H, F or Cl) such as CF_3CFH_2 (HFC-134a). The removal process of these compounds in the atmosphere is controlled by a series of reactions [2];

$$CF_3CHXY + OH \rightarrow CF_3CXY + H_2O \quad (1)$$

$$CF_3CXY + O_2 + M \rightarrow CF_3CXYO_2 + M \quad (2)$$

$$CF_3CXYO_2 + NO \rightarrow CF_3CXYO + NO_2 \quad (3)$$

The fate of the reactive alkoxy radicals, CF_3CXYO in the atmosphere is thus of importance if HFCs were to be viable alternatives. The atmospheric chemistry of CF_3CH_3 (HFC-143a) was investigated in which one of the main radicals generated was CF_3CH_2O and they were found to react with O_2 to form mostly CF_3CHO [3]. Subsequently the reaction of $CF_3CH_2CF_3$ (HFC-236fa) with oxygen was also investigated where the

corresponding $(CF_3)_2CHO$ radicals were eventually converted to $(CF_3)_2CO$ during the process [4]. Later, both ground state and vibrationally excited CF_3CFHO radicals were also produced in reactions involving CF_3CFHO_2 and NO species during the oxidation of HFC-134a [5, 6]. Apart from oxidation, a competitive channel for the destruction of CF_3CXYO radicals is its unimolecular decomposition. Extensive computational work have been reported on the unimolecular process of radicals such as CF_3CFHO and CF_3CF_2O where their C-C bonds break preferentially to form CF_3 and HFCO or CF_2O[2, 7]. However there were also contrasting reports on the thermal decomposition of CF_3CH_2O radicals where depending on the methods and basis sets used, the calculations could favour either the C-H bond or C-C bond dissociation [2, 7]. Under conditions where CF_3CH_2O radicals were produced from irradiating a mixture of $F_2/O_2/CF_3CH_3$(HFC-143a), O. J. Nielsen *et al* found that the C-H dissociation channel was favoured in which CF_3CHO was produced although many secondary reactions involving CF_3CHO also occurred and effectively reduced the yield of the aldehyde [3]. Calculations concerning the unimolecular dissociation of CH_2XCHFO (X=H,F) radicals have also been reported together with extensive data on the thermochemical properties of stable and free radical hydrofluorocarbon species [8].

In this Chapter, we have explored further the study of the unimolecular reactions of alkoxy radicals, in particular the CF_3CH_2O radical. It is well-known that alkoxy radicals could be cleanly generated by photolysis of their parent nitrite compounds in the gas phase [9-11]. Fourier Transform Infrared (FTIR) absorption spectroscopy of the nitrite itself was recorded with the assignment of its vibrational bands based on literature and density functional theory (DFT) calculations. A 355 nm pulsed Nd-YAG laser was

used to produce the alkoxy radical upon cleavage of the O-NO bond of the nitrite and FTIR Spectroscopy was utilized to probe the major products in particular the aldehydes of the C-C and C-H dissociation channels in a static gas cell. The effect of adding additional NO gas into the cell was investigated as it was known that under certain conditions, NO could abstract a hydrogen atom from the radical to form HNO and the same aldehyde produced from the C-H dissociation channel [9]. The relative importance of these two channels was also studied by photolysing the deuterated species, CF_3CD_2ONO where kinetic isotope effects could affect the outcome of the decomposition. UMP2 method with a large basis set such as aug-cc-PVTZ has been used for calculations of the C-C and C-H bond cleavage pathways, which includes the energies and geometries of transition states. A comparison with two other trifluoroalkoxy species and some alkyl nitrites were also made to explore how the branching ratios depended on different substituents. Lastly the effect of molecular oxygen on the photodissociation of trifluoromethyl nitrite and its various products were also explored where many more products were observed. A brief discussion about the reaction pathways of the nitrite in the presence of O_2 will be given as well.

3.2 Experimental section

3.2.1 Synthesis of nitrites

The radical precursor 2,2,2-trifluoroethyl nitrite, CF_3CH_2ONO was prepared by dropwise addition of about 1 cm^3 concentrated sulfuric acid (Merck, 95-97%) into an aqueous solution containing $NaNO_2$ (0.7g, Aldrich, 97%) and CF_3CH_2OH (1g, Chemical Research Ltd, 99%) or its deuterated form, CF_3CD_2OH (1g, Aldrich, 97%). A slow

nitrogen gas flow was used to carry the nitrite vapour to a dry ice-acetone trap for collection. Methyl, ethyl nitrite and fluoronitrites such as $(CF_3)_2CHONO$ and CF_2HCH_2ONO were also similarly prepared from the corresponding alcohols [11, 12]. For C_3-C_5 alkyl nitrites and 1, 2-Bis-nitrosoxyethane, they were obtained by the action of nitrous acid upon alkyl alcohols (99%, sigma-aldrich) and ethylene glycol (sigma-aldrich, 99%) [13]. A cold diluted concentrated sulfuric acid with alkyl alcohol solution was added to the cold sodium nitrite solution during five to ten minutes. The nitrite solution is cooled in ice and the contents kept thoroughly mixed by a rapid, whirling motion. Stop stirring and allow it to stand for a few minutes until the contents separate in two layers, nitrite above and sodium sulfate solution below. Separate sharply in a separatory funnel and wash with salt and acid sodium carbonate solution. The yellow-green liquids were subjected to a series of freeze-pump-thaw for air removal. The liquids were then warmed to room temperature and about 10 to 15 Torr of the vapors was flowed into a 15 cm long static gas cell previously evacuated by a rotary pump to a background pressure of 10^{-2} Torr. The nitrite vapors were stable and could be stored for a week with very little decomposition under reduced ambient light conditions.

3.2.2 UV spectrum of CF_3CH_2ONO

In order to select the appropriate laser for photolysis and comparing with the UV spectrum of alkyl nitrite in literature, a UV/VIS spectrum of CF_3CH_2ONO was recorded. Figure 3.1 shows several bands in the UV-VIS absorption spectrum of about 100 Torr of CF_3CH_2ONO recorded at a resolution of 0.2 nm. The well-resolved vibrational progress is similar to the other nitrite which correspondsto the $\pi^* \leftarrow n$ transition in the near ultra-

violet region. The peaks are thought to be members of a progression caused by excitation of the –N=O stretching vibration (ν_3) in the trans isomer of the excited state [14].

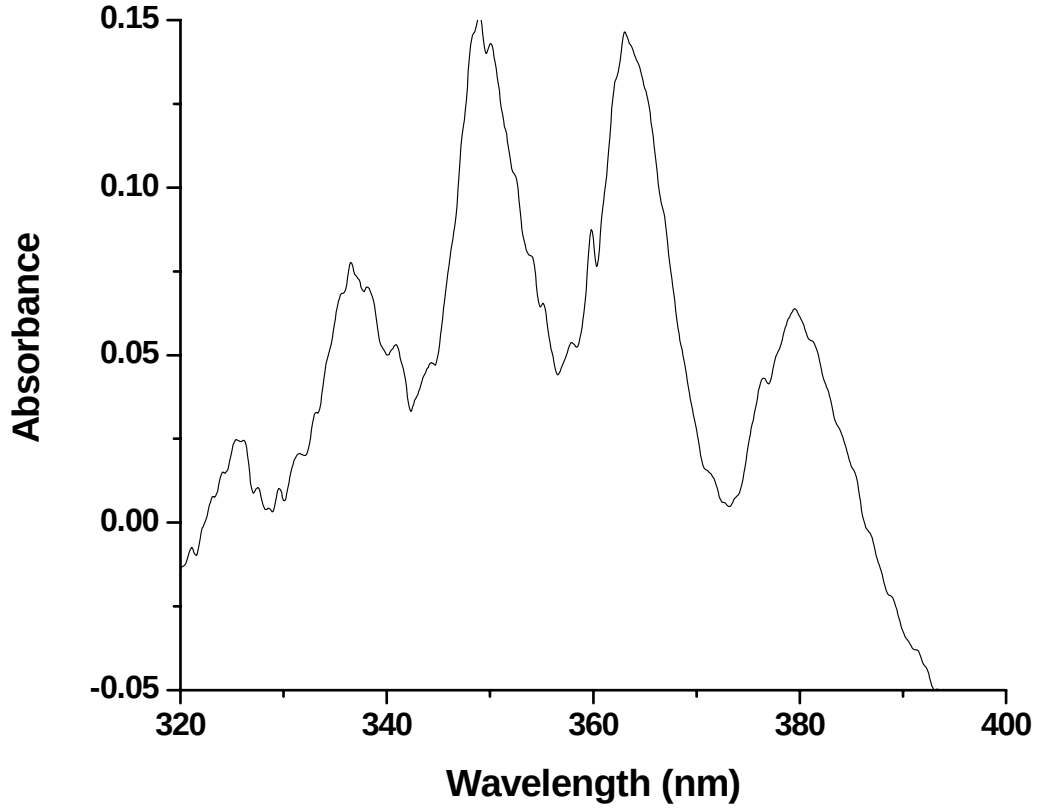

Figure 3.1 The UV/VIS absorption spectrum of purified CF_3CH_2ONO (~100 Torr) in a 1 cm quartz cell recorded with a resolution of 0.2 nm

3.2.3 FTIR setup

A glass cell with perpendicularly cross arms terminated by KBr and quartz windows was used as the photolysis chamber. It could be fitted inside the sample compartment of the Nicolet Nexus 870 FTIR spectrometer with the FTIR beam entering and exiting the cell through the KBr windows. On the other hand, the frequency-tripled 355 nm Nd-YAG laser (Continuum Surelite III-10, 10 Hz, and 10 ns pulse) was propagated through the quartz windows at right angles to the FTIR beam. The infrared

spectrum was then scanned at appropriate intervals of a few minutes from 600 to 4000 cm^{-1} with a resolution of 0.5 cm^{-1}. The relative rate of IR signal changes of the precursors and products were subsequently monitored with respect to the irradiation time of the Nd-YAG laser. The peak height of the N=O band of the nitrite species was kept to less than 20% absorption to ensure that its absorption (area under the curve) was directly proportional to the concentration as dictated by Beer-Lambert's law. Since only relative rates of decay or appearance of molecules in the gas cell were required for analysis, it was not necessary to convert the molecular absorptions to absolute concentrations. For the photolytic study of CF_3CH_2ONO in the presence of molecular oxygen, the gas cell which has already been filled with 10 Torr of nitrite was quickly exposed to compressed air (99.95%) of 1 bar. The valve of the gas cell was then closed and 355 nm photolysis was initiated and FTIR spectra collected as described earlier.

As we anticipated the production of formaldehyde as one of the products of trifluoroethylnitrite photolysis, it was useful to have an FTIR spectrum for pure formaldehyde vapour for comparison purposes. Thus the vapour was generated simply by heating solid paraformaldehyde to 250^{o}C-300^{o}C and collected into the static gas cell via a vacuum line. The absorption spectrum of CH_2O was similarly obtained using the Nicolet FTIR spectrometer. We have also recorded an IR spectrum for CF_3CHO vapour generated from its liquid form. Experiments involving NO (Linde, 99%) and NO_2 (Linde, 99%) gases were carried out without further gas purification. For broadband irradiation studies, a 200W Xenon lamp (300 nm - 800 nm) was used to replace the laser as the photodissociation source. The light was focused (diameter ≈ 5mm) into the gas cell and FTIR spectra were collected at regular intervals.

3.3 Photolysis of trifluoroethylnitrite

3.3.1 IR band of CF_3CH_2ONO

The infrared spectrum of trifluoroethylnitrite was first obtained at a resolution of 0.5 cm^{-1} and its vibrational band assignment and relative intensity for CF_3CH_2ONO are given in Table 3.1. Computed vibrational frequencies using density functional theory B3LYP/6-31G(d) (scaling factor = 0.9613) in Gaussian 98 and comparisons with the recently obtained spectrum of $(CF_3)_2CHONO$ were used as a guide for spectral assignment [12, 15]. Previously, only a partial assignment in particular the N=O stretch of this species was made [16]. The trans-nitrite form turns out to be dominant as observed by the N=O stretch at 1726 cm^{-1} while a much weaker peak at 1685 cm^{-1} is assigned to the N=O stretch of the cis-nitrite. Because of the much higher concentration of the trans-nitrite, most of the intense infrared peaks could be assigned to this species only.

Table 3.1 IR band assignments for CF_3CH_2ONO. The calculations of the vibrational frequencies (scaling factor 0.9613) were performed using B3LYP/6-31G(d) In Gaussian 98 and displayed under calc column. Both the experimentally observed frequency and relative band intensity are also shown in columns 1 and 3

υ_{obs}	υ_{calc}	Rel. intensity$_{obs}$	Band assignment
508	504	0.13	C-F bend
575	574	0.15	N-O str
671	648	0.25	C-O-N bend
781	786	0.51	O-N-O bend
840	816	0.08	CF_3 str
970	958	0.28	C-H rocking
1040	1065	0.06	C-O str
1095	1116	0.17	C-F str
1183	1176	1.00	C-Fstr
1290	1254	0.46	C-F str
1401	1381	0.03	C-H bend
1440	1436	0.027	C-H wag
1726	1746	0.63	N=O str
2965	2970	0.04	C-H str
3416	(1746 x 2)	0.01	N=O str overtone

3.3.2 Photolysis of CF_3CH_2ONO

Upon 355 nm photolysis, the CF_3CH_2O radical was generated from trifluoroethylnitrite and the subsequent decay of this radical into stable products was followed by FTIR spectroscopy via its N=O stretching band. Two main decomposition pathways are expected i.e. C-H bond cleavage to form CF_3CHO and H atom and C-C bond cleavage to form CF_3 and CH_2O. Thus the most intense bands of CF_3CHO (v = 1787 cm^{-1}) and CH_2O (v = 1746 cm^{-1}) were searched for in order to estimate the

branching ratio for these two channels [20]. Surprisingly we found that only CF_3CHO signals could be detected during and after all the nitrite have decomposed under approximately two hours of photolysis (Figure 3.2). Although the photolysis time could be shorter, a low power laser beam (5 mJ/pulse, 1 cm diameter) was used to avoid the occurrence of multiphoton dissociation process. When the absorption intensity of formaldehyde was calibrated against its vapour pressure, we found that the minimum detectable formaldehyde pressure was about 0.3 Torr. Since CH_2O could not be detected in a photolysis of 15 Torr of CF_3CH_2ONO, a yield of not more than 2% of formaldehyde can then be determined. We have also studied the effect of buffer gas on the outcome of the photolysis but the addition of argon or nitrogen (10 Torr to 1 bar) into the gas cell has little effect i.e. CF_3CHO was still the only major product detected.

The unimolecular reaction is only slightly pressure-dependent as the decay rate of the nitrite is very similar with and without the presence of argon gas (10 Torr to 1 bar Torr) in the cell (Figure 3.3). However the important information gathered here is that the decay rate of nitrite is determined to be almost the same as the appearance rate of CF_3CHO, indicating that the C-H bond cleavage is the main and perhaps only channel of decomposition of the CF_3CH_2O radical. If the C-C bond dissociation is a significant channel, the value of the measured appearance rate of CF_3CHO should only be a fraction of the decay rate of the nitrite. However, our photolysis results seem to have supported earlier studies on the dissociation pathway of CF_3CH_2O radical in which CF_3CHO was the detected product when a mixture of F_2 /O_2 /CF_3CH_3 was irradiated, although no mention was made whether there was a simultaneous production of formaldehyde as well

[6]. In order to check the validity of the dominance of the C-H bond cleavage channel, the production or rather the absence of formaldehyde is further investigated.

(a)

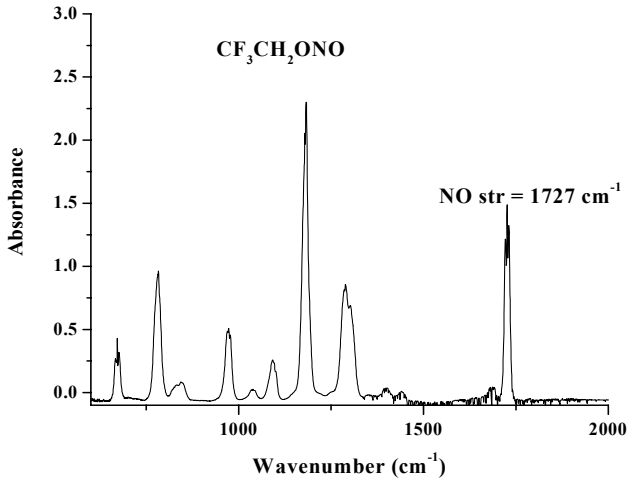

(b)

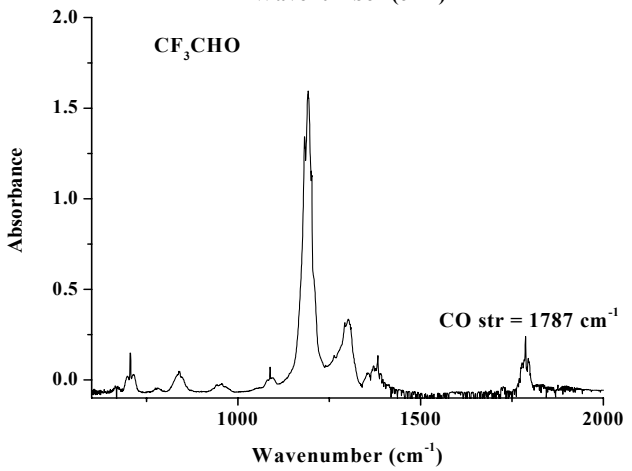

(c) 10 Torr CF_3CHO

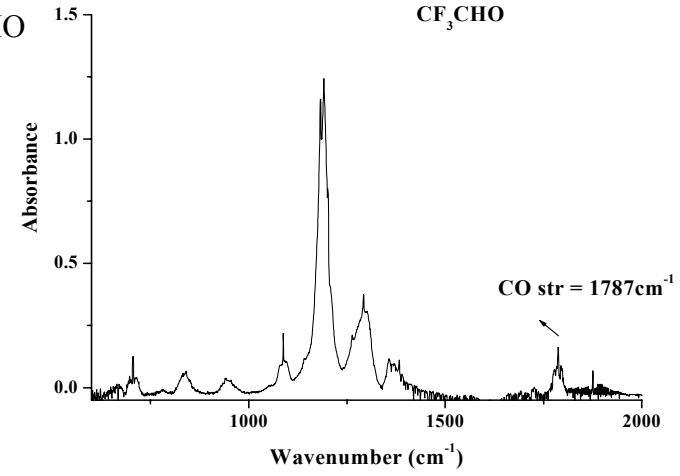

Figure 3.2: (a) IR spectrum of CF_3CH_2ONO before photolysis. (b) IR spectrum of the product, CF_3CHO after 2 hours of 355 nm laser photolysis (10 mJ/pulse). (c) IR spectrum of a pure sample of CF_3CHO

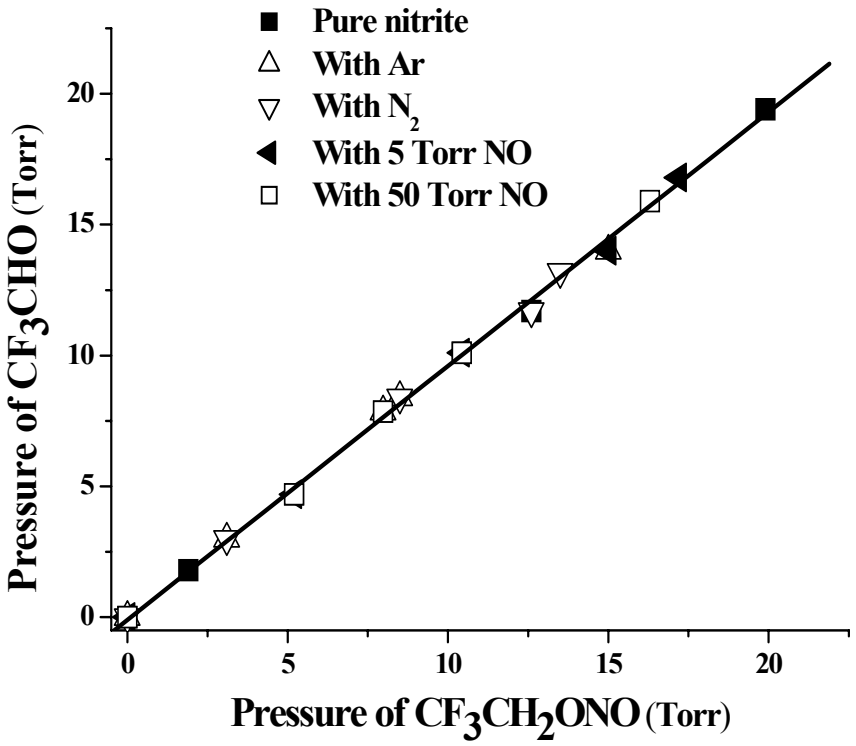

Figure 3.3 Plot of CF_3CHO generation vs CF_3CH_2ONO consumption in the presence of Ar, N_2, NO or in pure form

When formaldehyde vapour prepared from the pyrolysis of paraformaldehyde was photolysed with the 355 nm laser, no decomposition was seen even after a long irradiation period of a few hours. It suggested that if formaldehyde had been formed during the irradiation period of trifluoroethylnitrite, it could not be severely depleted by photodecomposition. Besides, one of the final products from the self-decomposition of formaldehyde or from its reactions with many molecules is carbon monoxide but no production of CO (v = 2143 cm^{-1}) was observed here. The relative vibrational band intensity of ν_{CO} of CF_3CHO to CH_2O was also considered and it turned out that from our experiments and literature values, the former intensity could be about 10 higher than the latter [17]. However the sharp Q-branch of the ν_{CO} band of CH_2O is itself very intense

and sharp such that given the same vapour pressures of CH_2O and CF_3CHO, the former peak intensity is in fact higher than the peak intensity of the broader vibrational band of CF_3CHO. Based on the sensitivity of our spectrometer, the formaldehyde signals should have been observed if it were the product of a significant channel of dissociation. This sensitivity factor was tested when we studied the photodissociation of methyl nitrite, CH_3ONO which is known to produce formaldehyde as its main product upon 355 nm photolysis. Indeed, the v_{CO} band of formaldehyde at 1743 cm^{-1} was easily identified even when the methyl nitrite pressure was gradually reduced from 10 Torr to 0.5 Torr in a series of experiments. The reaction of formaldehyde with NO (v = 1875 cm^{-1}) was then studied as a possible depletion process since NO is always produced upon 355 nm nitrite photodissociation. However, we failed to observe any changes in the formaldehyde signals even when excess NO ([NO] / [CH_3ONO] = 10:1) was added to the gas cell.

Two other experiments i.e. thermal heating and broadband irradiation of the trifluoroethylnitrite were performed for comparison studies with the laser photolysis results. About 10 Torr of CF_3CH_2ONO was heated in the gas cell using a heating tape wrapped uniformly around the external gas cell wall. Surprisingly, heating the cell between 250-300^oC for one hour not only produced CF_3CHO as the major product but there was again no trace of formaldehyde production. Thus even under thermal conditions, the trifluoroethoxy radical appears to dissociate preferentially via C-H bond cleavage. It is unlikely that the pulsed laser might have induced significant secondary chemical reactions or further photodissociation in the gas cell since the actual power used was small (5 mJ/pulse, 10 Hz, 1 cm diameter beam). Nevertheless, we still subjected the nitrite to a weaker broadband irradiation source such as a Xenon lamp (200 W, 300 nm -

800 nm). The irradiation was carried out for a longer period (5 hours) than the laser photolysis but CF_3CHO and NO remained the only products detected during and at the end of the reaction when all the nitrites have decomposed.

We have also considered the contributions from electronically excited state alkoxy radicals since such species have been considered to play an important role in the atmosphere [5]. In the case of the methoxy radical, the (0, 0) A-X transition is located around 305 nm, hence it is not possible to use the 355 nm laser for excitation [18]. Furthermore, C-O bond cleavage is the main channel of its excited state dissociation so it could not have produced the trifluoroaldehyde. Since ethoxy, propoxy and t-butoxy radicals exhibit rather similar electronic structure to methoxy [18], it is also expected that the bandcenter of the equivalent A-X transition of trifluoroethoxy radical would be rather close to that of CH_3O. Hence the excited state trifluoroalkoxy species could not be accessed and thus it is not expected to play a significant role under our conditions here.

3.3.3 Effect of NO

The effect of NO on the fate of the CF_3CH_2O radical was also investigated since NO is always produced together with the radical upon photodissociation of the nitrite. It is known that NO might abstract the H atom from alkoxy radicals or combine with the radical to regenerate the nitrite [9];

$$CF_3CH_2O + NO + M \rightarrow CF_3CH_2ONO + M \quad (4)$$

$$CF_3CH_2O + NO \rightarrow HNO + CF_3CHO \quad (5)$$

Thus if reaction (5) were dominant under our experimental conditions, it might explain the formation of CF_3CHO in the gas cell. For every NO pressure, the decay and

appearance rates of the nitrite and aldehyde respectively were determined in the same way as shown in Figure 3.4. It appears that as the NO pressure increases in the cell, less CF_3CHO is produced and more CF_3CH_2ONO remains unreacted. This observation supported the dominance of the first channel instead where the recombination of the fluoroalkoxy radical with NO takes place preferentially. It is interesting to note that the magnitude of the decay rate of nitrite and the appearance rate of the aldehyde remains very similar to each other regardless of the NO pressure.

3.3.4 Photolysis of CF_3CD_2ONO

We have also studied the 355 nm unimolecular decomposition of the deuterated nitrite species, CF_3CD_2ONO (ν_{NO} = 1727 cm^{-1}). The efficiency of the C-H bond dissociation ought to decrease by the kinetic isotope effect which in principle could lower the C-H dissociation rate several times. The decrease in rate is not unexpected since it can be seen later that the transition state of the unimolecular decomposition of the trifluoroalkoxy radical to CF_3CHO and H atom involves mainly the C-H bond as the reaction coordinate. Despite this, CF_3CDO (ν_{CO} = 1768 cm^{-1}) remains the main product of the unimolecular dissociation while CD_2O (ν_{CO} = 1700 cm^{-1}) could not be detected [17].

a)

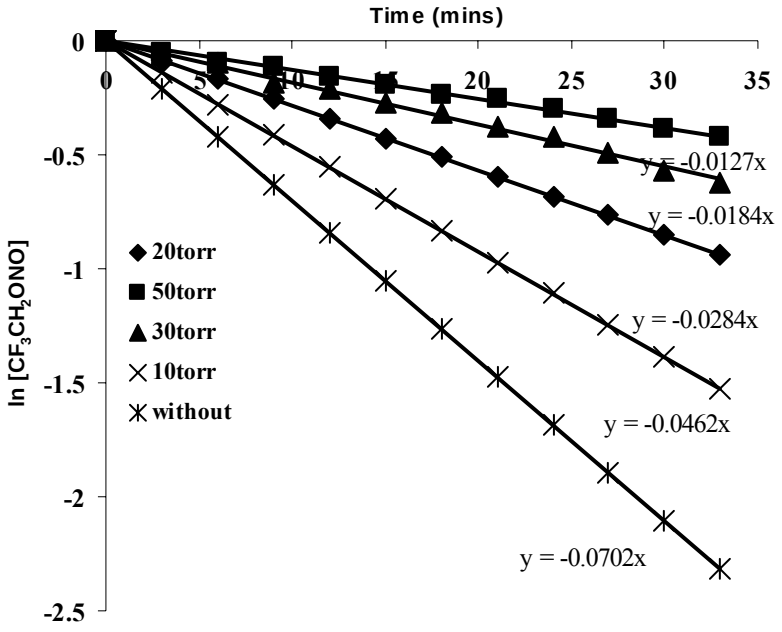

b)

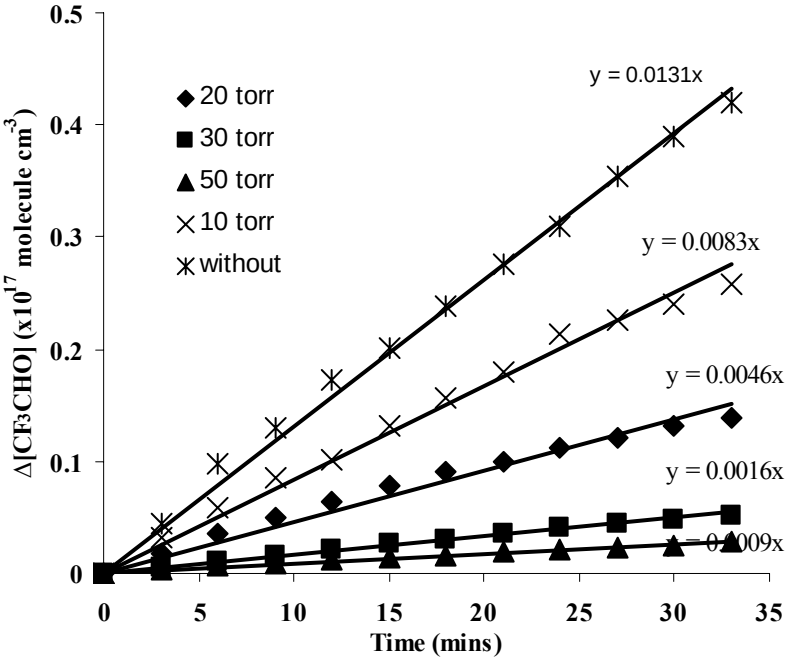

Figure 3.4 NO effect to the decay of CF_3CH_2ONO and the appearance of CF_3CHO

3.3.5 Computational work

Due to some contrasting reports on the dissociation channels of fluoroalkoxy radicals in the literature, some calculations on the C-C and C-H bond dissociation pathways were carried out using UMP2/aug-cc-PVTZ level of theory in Gaussian 98, as shown in Figure 3.5. The activation energy calculated for the C-H bond cleavage pathway was almost 100 kJ mol^{-1}, which was 25 kJ mol^{-1} higher than the corresponding activation energy for the C-C bond dissociation. A long C-H bond of 1.98Å in the transition state was calculated for the C-H dissociation channel. The C-O bond is also becoming shorter (1.20 Å) while the C-C bond remains almost unchanged with a length of 1.55 Å. For the transition state in which the C-C bond dissociates, an extended C-C bond of 2.20 Å was determined and similarly, a shorter C-O bond of 1.23 Å and an unchanged C-H bond length of 1.10 Å were computed. These dimensions agreed very well with the transition state structures calculated previously for the same decomposition processes [2, 7]. Calculations of the energies of the final products also revealed that CF_3 and CH_2O are lying at a lower energy (about 38 kJ mol^{-1}) than CF_3CHO and H. It appears from these calculations that both the activation barrier and energies of the final products favour the C-C bond dissociation channel. A comparison with previous computational work on the CF_3CH_2O radical is also presented here. Using PMP4SDQ/6-31G(d)//UHF/6-31G(d)+DZPE level of theory, Francisco *et al* [2] found that the final products CF_3CHO + H were more stable than CF_3 + CH_2O by 8.8 kJ/mol. However the activation energy for the C-C bond dissociation channel was lower still, by 5.9 kJ mol^{-1}. In Somnitz and Zellner's work [7], the C-C cleavage activation barrier of CF_3CH_2O was computed using a modified G3(MP2) theory to be very large, 100 kJ mol^{-1} hence

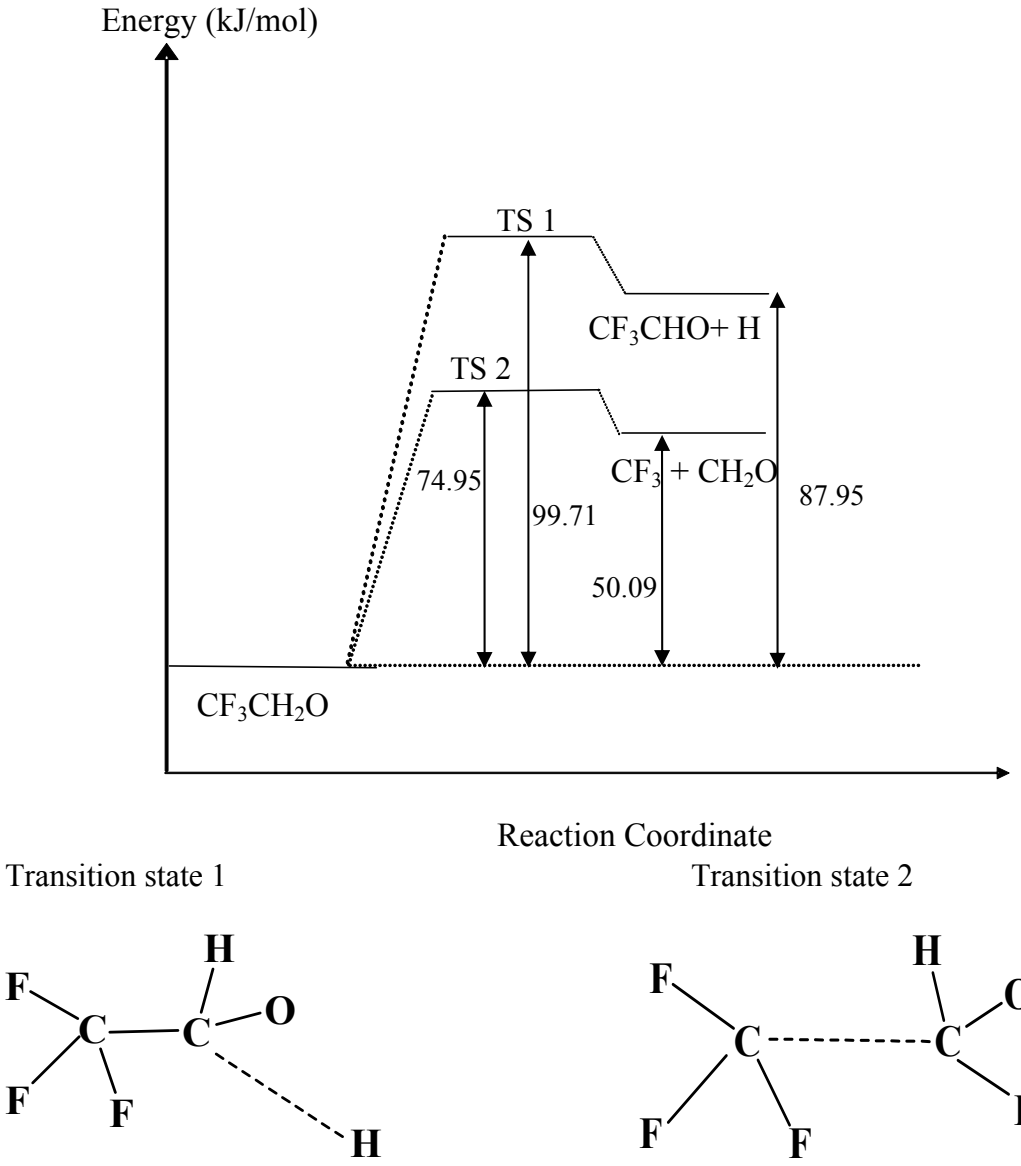

Figure 3.5: The energies of the molecules and transition states involved in the photodissociation of 2, 2, 2-trifluoroethylnitrite using UMP2/cc-pVTZ level of theory in Gaussian 98. T.S.1 represents the C-H bond dissociation pathway (C---H 1.98 Å) and T.S.2 represents the C-C bond dissociation pathway (C----C, 2.20 Å)

rendering this channel less probable. Although the energetics of the C-H cleavage channel was not determined, they compared it to the corresponding channel in the dissociation of CH_3CHFO and CH_2FCHFO radicals [16]. A range of values from 62 to 67

kJ/mol were computed so if these values were also valid for the CF_3CH_2O case, the C-H dissociation channel would then be more favourable. Disappointingly, our computational results only agreed partially with this previous work and did not match our experimental observations. The data collected here tend to favour Sonitz and Zellner's calculations where the C-H bond dissociation products are expected to be dominant. However the interesting aspect of the experimental results is that when CF_3CH_2ONO is photolysed using a 355 nm laser, CF_3CHO is the only product detected with no trace of formaldehye being formed. This is also a little surprising since the energetics of both channels are not very different and one might expect the fluoroalkoxy radical to acquire enough excess energy from the laser to undergo dissociation via both channels. It turns out that C-H dissociation being the exclusive channel is not restricted to only the CF_3CH_2O radical but to two other fluoroalkoxy radicals studied here.

3.3.6 Reaction of CF_3CH_2ONO with O_2

The reactions of CF_3CH_2ONO or CF_3CH_2O with molecular oxygen were also briefly explored here. Previously, numerous products were obtained when such species were oxidized and reactions involving excited state radicals were also suggested to have contributed to the process [5, 6]. In this work, our main objectives are to determine whether CF_3CHO is still the main product of decomposition in the presence of oxygen in the gas cell and to determine via FTIR spectroscopy, as many products of CF_3CH_2O oxidation as possible. Indeed when a mixture of 10 Torr CF_3CH_2ONO and 1 bar of air in the gas cell was photolysed by 355 nm laser, the IR bands of many products such as CF_3CHO, CF_3CH_2OH, CF_2O, NO_2, NO and CO were detected. Figure 3.6 shows the evolution of the main products with respect to the duration of photolysis.

The dominant product turns out to be trifluoroethylnitrate, $CF_3CH_2ONO_2$ generated from the reaction of CF_3CH_2O with NO_2 [10]. The nitrate production could be explained as a result of the presence of NO_2 in the gas cell from the reaction of O_2 with NO which comes directly from the photodissociation of the nitrite. NO_2 would then combine efficiently with the alkoxy radical to form the nitrate species. Since most nitrates such as ethylnitrate, $C_2H_5ONO_2$ have electronic absorptions shorter than 310 nm, $CF_3CH_2ONO_2$ is also not expected to decompose further upon 355 nm photolysis. As the infrared spectrum of $CF_3CH_2ONO_2$ has not been recorded before, we have tabulated the observed vibrational bands and their assignments with the help of similar calculations performed for the CF_3CH_2ONO species as well as comparisons with the IR spectrum of ethylnitrate [18] (Table 3.2). Although the nitrate species is the main product detected, many other interesting products that appeared need to be accounted for as well. The reaction scheme is indeed complicated and because of overlaps of infrared peaks of different molecules, it was not possible to detect all the species of the reaction. Many reaction schemes have been proposed for the oxidation of HFC compounds and here we list some of the more important ones based on previous work and the observations of the main products of 355 nm photolysis in Figure 3.7 [5,7,9].

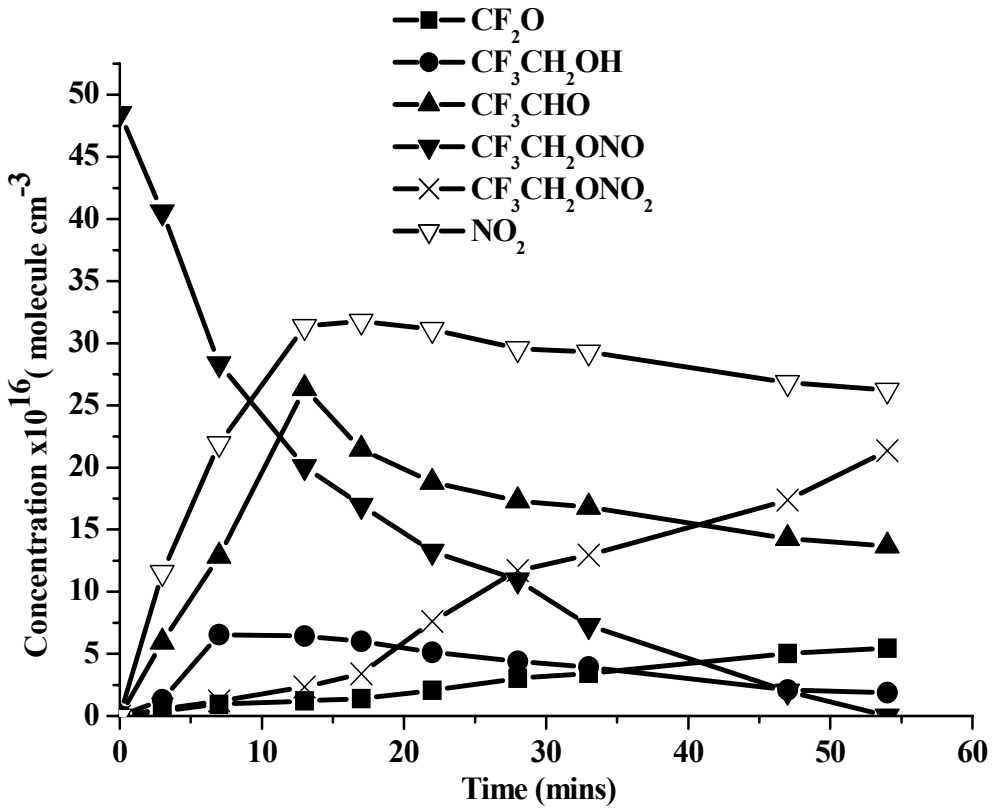

Figure 3.6 The variation of concentration of the major molecular species when 10 Torr of CF_3CH_2ONO was 355 nm photolysed (5 mJ/pulse) in the presence of 1 bar of air

In the presence of O_2, only a small infrared signal of CF_3CHO was seen in the final mixture which indicates that the reaction of trifluoroethoxy radical with NO_2 proceeds at a higher rate than its unimolecular decomposition. It can be seen that the CF_3CHO signal reached a maximum before it decayed further via secondary chemical reactions. Oxygen atoms are also generated along with NO_2 when NO reacts with O_2. Hence CF_3CHO could react with O atoms to yield OH and CF_3CO in which the latter species decomposed to give CF_3 and CO. Since a little amount of CF_2O (ν_{CO} = 1948 cm^{-1}) was seen, it was presumably generated from further reactions of O_2 or O atoms with CF_3 radicals. We have also detected the presence of CF_3CH_2OH, which might have come

from the reaction of the fluoroalkoxy radical with a hydrogen atom source. Initially, it was thought that the radical abstracted H atom from its parent nitrite, CF_3CH_2ONO or CF_3CHO but the infrared signal of the alcohol was not observed when oxygen was absent.

Table 3.2 IR band assignments for $CF_3CH_2ONO_2$. The calculations of the vibrational frequencies were performed using B3LYP/6-31G(d) (scaling factor 0.9613) In Gaussian 98 and displayed under υ_{calc} column. Both the experimentally observed frequency and relative band intensity are also shown in columns 1 and 3

υ_{obs}	υ_{calc}	Rel. intensity$_{obs}$	Band assignment
625	607	0.08	H-C-O bend
678	658	0.08	C-F bend
714	721	0.07	C-N-O bend
826	810	0.32	O-N-O_2 bend
961	942	0.15	C-H str
1049	1027	0.16	C-O str
1188	1164	1.00	C-F str
1267	1247	0.43	C-H wag
1306	1298	0.48	C-H bend
1352	1304	0.57	NO_2 str
1398	1382	0.21	C-H bend
1428	1429	0.13	C-H wag
1694	1722	0.78	NO_2 str
2956	3000	0.05	C-H str
2989	3058	0.05	C-H str

Hence the H atom source must have originated from reactions with O_2 or O atoms. A likely source of H atoms could be HO_2 radicals, produced from the reaction of CF_3CH_2O and O_2. This channel appears to be of minor importance especially in the presence of NO_2 otherwise more CF_3CHO would have been produced instead. Nevertheless the

concentration of the trifluoroalcohol is small hence it is possible that the reaction of HO_2 with CF_3CH_2O contributes partially to its production. Obviously the products detected here do not necessarily mirror the actual process occurring in the atmosphere. Since a static cell is used where the molecular species could not be flowed out of the reaction region, the reactive products will also take part in secondary reactions. In this case, the reaction of NO_2 with the flouroalkoxy radical is a good example where given sufficient concentration of NO_2, the fluoroethylnitrate species could become dominant and remain undecomposed in the absence of light of wavelengths shorter than 200 nm.

$$CF_3CH_2ONO \rightarrow CF_3CH_2O + NO$$

$$NO + O_2 \rightarrow NO_2 + O$$

$$CF_3CH_2O + NO_2 \rightarrow CF_3CH_2ONO_2$$

$$CF_3CH_2O + O_2 \rightarrow CF_3CHO + HO_2$$

$$O + CF_3CHO \rightarrow OH + CF_3CO$$

$$CF_3CO \rightarrow CF_3 + CO$$

$$CF_3 + O_2 \rightarrow CF_3O_2$$

$$CF_3O_2 + NO \rightarrow CF_3O + NO_2$$

$$CF_3O \rightarrow CF_2O + F$$

Figure 3.7 Reactions occurring in the 355nm photolysis of CF_3CH_2ONO in the presence of 1 bar of air in a static gas cell

3.4 Photolysis of other fluoronitrites

Besides CF_3CH_2ONO, two other fluoronitrites, $(CF_3)_2CHONO$ (ν_{NO} = 1767 cm^{-1}) and CF_2HCH_2ONO (ν_{NO} = 1710 cm^{-1}) were synthesized for comparison purposes [7]. In both cases, 355 nm photolysis of the nitrites also induced C-H bond dissociation of the

fluoroalkoxy radicals. CF_2HCHO (ν_{CO} = 1770 cm^{-1}) and $(CF_3)_2CO$ (ν_{CO} = 1809 cm^{-1}) were the main products of the dissociation process of CF_2HCH_2ONO and $(CF_3)_2CHONO$ respectively [12, 19]. Similar to the CF_3CH_2O case, the C-C bond dissociation products, formaldehyde (from CF_2HCH_2ONO) and CF_3CHO (from $(CF_3)_2CHONO$) were not detected. The magnitude of the rate of decay of the nitrite was almost the same as the appearance rate of the corresponding C-H bond dissociation product. In a review by Atkinson [20], the thermal decomposition pathways of alkoxy radicals (C1-C5 species) were discussed. Depending on the nature of the substituent groups, either C-C or C-H dissociation pathways would be favoured. In the fluoroalkoxy cases, it is possible that the electron-withdrawing nature of the fluorosubstituents could also have influenced the outcome of the dissociation pathway. At this point, more computational studies are required in order to better understand such dissociation processes.

3.5 Conclusion

The synthesis and photolysis of nitrites and the exchange reactions were investigated in this chapter. All the nitrites have significant N=O stretch in the range of 1600-1800 cm^{-1}. The final products of the photolysis of nitrites were detected using FTIR spectroscopy. *Ab initio* studies using density functional methods such as UB3LYP/aug-cc-PVTZ have been used particularly to determine the different reaction pathways for the decomposition of alkoxy radicals produced in the dissociation of nitrites. The decomposition products of all nitrites are summarized in Table 3.3.

Table 3.3 The products of the decomposition of alkyl nitrites

Nitrites	Radical	Pathways	Main products
CF_3CH_2ONO	CF_3CH_2O	C-H	CF_3CHO
CF_3CD_2ONO	CF_3CD_2O	C-H	CF_3CDO
$CF_3CH(ONO)CF_3$	$CF_3CH(O)CF_3$	C-H	CF_3COCF_3
CF_2HCH_2ONO	CF_2HCH_2O	C-H	CF_2HCHO
CH_3ONO	CH_3O	C-H	CH_2O
CH_3CH_2ONO	CH_3CH_2O	C-H	CH_3CHO
$CH_3CH_2CH_2ONO$	$CH_3CH_2CH_2O$	C-H& C-C	CH_3CH_2CHO,CH_2O
$CH_3CH(ONO)CH_3$	$CH_3CH(O)CH_3$	C-H & C-C	CH_3CHO, CH_3COCH_3
$CH_3(CH_2)_3ONO$	$CH_3(CH_2)_3O$	C-H & C-C	$CH_3CH_2CH_2CHO$
$CH_3CH(ONO)CH_2CH_3$	$CH_3CH(O)CH_2CH_3$	C-C	CH_3CHO
$(CH_3)_3CONO$	$(CH_3)_3CO$	C-C	CH_3COCH_3
$CH_3(CH_2)_4ONO$	$CH_3(CH_2)_4O$	C-C	$CH_3(CH_2)_3CHO$

Reference

1. R. Zellner, Global Aspects of Atmospheric Chemistry, Steinkopff, Darmstadt, 1999

2. J. S. Francisco, Z. Li, A. Bradley and A. E. W. Knight, Chem. Phys. Lett., 214, 77, 1993

3. O. J. Nielsen, E. Gamborg, J. Sehested, T. J. Wallington and M. D. Hurley, J. Phys. Chem., 98, 9518, 1994

4. T. E. Mogelberg, J. Platz, O. J. Nielsen, J. Sehested and T. J. Wallington, J. Phys. Chem., 99, 5373, 1995

5. T. J. Wallington, M. D. Hurley, J. M. Fracheboud, J. J. Orlando, G. S. Tyndall, J. Sehested, T. E. Mogelberg and O. J. Nielsen, J. Phys. Chem., 100, 18116, 1996

6. T. E. Mogelberg, J. Sehested, T. J. Wallington and O. J. Nielsen, Int. J. Chem. Kinet., 29, 209, 1997

7. H. Somnitz and R. Zellner, Phys. Chem. Chem. Phys., 3, 2352, 2001

8. H. Hou, B. Wang and Y. Gu, Phys.Chem.Chem.Phys., 2, 61, 1999

9. W. Deng, A. J. Davis, L. Zhang, D. R. Katz and T. Dibble, J. Phys. Chem. A, 105, 8985, 2001

10. L. Batt, Int. J. Chem. Kinet., 11, 977, 1979

11. H. W. Thompson and F. Dainton, Trans.Far.Soc., 33, 1546, 1937

12. M. P. Sulbaek Anderson, M. D. Hurley, J. C. Ball, W. F. Schneider, T. J. Wallington and O. J. Nielsen, Int. J. Chem. Kinet., 35, 159, 2003

13. A. N. Williams, J. Am. Chem. Soc., 55, 3888, 1933

14. A. F. Tuck, J. Chem. Soc. Faraday Trans 2, 73, 689, 1977

15. M. W. Wong, Chem Phys.Lett., 256, 391, 1996

16. R. N. Haszeldine and B. J. H. Mattinson, J. Chem. Soc., 4172, 1955

17. C. V .Berney, Spectrochim. Acta. Part A, 25, 793, 1969

18. C. C. Carter, J. R. Atwell, S. Gopalakrishnan and T. A. Miller, J. Phys. Chem. A, 104, 9165,

19. 2000V. A. Bataev, E. K. Dolgov, A. V. Abramenkov, V. I. Pupyshev and I. A. Godunov, Int. J. Quant. Chem., 88, 414, 2002

20. R. Atkinson, Int. J. Chem. Kinet., 29, 99, 1997

– CHAPTER 4 –

Hydrogen atom abstraction kinetics by t-butoxy radical

4.1 Introduction

Alkoxy radicals, RO· are key intermediates in the oxidation of hydrocarbons in the atmosphere [1, 2]. The reaction pathways for alkoxy radicals vary according to their structure and much effort has been devoted to establishing the relative importance of its unimolecular decomposition. In addition, these radicals are favored for abstracting H atom from a hydrocarbon because the formation of a strong O-H bond allows the process to have appreciable rate coefficients. In particular, the t-butoxy radical generated from di-butyl peroxide has been used for H-atom abstraction reactions in the liquid phase [3-6]. Since its unimolecular reaction rate has been measured over a range of temperatures, the rate of the abstraction reaction represented by (2) below could be determined by measuring the ratio of acetone to t-butanol which are the products of (1) and (2) respectively.

$$(CH_3)_3CO + (M) \rightarrow (CH_3)_2CO + CH_3 + (M) \qquad (1)$$

$$(CH_3)_3CO + RH \rightarrow (CH_3)_3COH + R \qquad (2)$$

In the gas phase, the rate coefficient and Arrhenius parameters of the decomposition of t-butoxy radical relative to the alkoxy radical combination with NO

have been investigated [7-9]. These important parameters have also been obtained by Choo [10-12] and Sway [13, 14] by using uv photolysis or by thermal decomposition of di-t-butyl peroxide. However the substrates, RH studied were primarily limited to a few alkanes and alkenes.

In this Chapter, we have substantially explored further the H-atom abstraction reactions of t-butoxy radicals with amines, halogenated organic compounds and nitriles at room temperature. FTIR spectroscopy was utilized to probe the two main products from unimolecular decomposition and hydrogen atom abstraction in a static cell [15]. The kinetic isotope effect and Arrhenius parameters for some substrates were also explored in order to determine activation barriers. Computational calculations using Gaussian 03 were performed to provide a correlation between the experimental data with the various thermodynamic and kinetic parameters [16].

4.2 Experimental section

The radical precursors, t-butyl nitrite, di-t-butyl peroxide and the hydrogen-containing substrates were purchased from Sigma-Aldrich. Distillation and free-pump-thaw cycles were carried out to remove impurities before these compounds were used in the kinetic runs. A static Pyrex cell (15 cm pathlength) with a temperature controller was used as the reaction vessel initially evacuated by a rotary pump to a background pressure of 2×10^{-3} Torr. The pressures used for the t-butyl nitrite and the substrates were 1-2 Torr and 10-20 Torr respectively. About 100-760 Torr SF_6 buffer gas was flowed into the cell from its gas cylinder (Linde gas, 99.9%) without purification.

The t-butoxy radical was generated by 360-380nm broadband lamp photolysis of t-butyl nitrite. The infrared spectrum (Nicolet Nexus 870) was scanned every 3 minutes from 1000 to 4000 cm^{-1} with a resolution of 1 cm^{-1}. The relative rate of the IR signal changes of acetone (1738cm^{-1}) and t-butanol (1140cm^{-1}) were monitored with respect to the irradiation time. Initial rate measurements were used to minimize contributions from secondary reactions caused by product buildup. During the first few minutes of irradiation, there were little formation of acetone and t-butanol (absorbances < 20%) so the Beer-Lambert's Law could be used to form a linear relationship between the absorbance and concentration. For experiments using di-t-butyl peroxide as the precursor, a 254 nm mercury lamp was used as the photodissociation source in a quartz cell of similar size (15 cm long, 2.5 cm diameter) while maintaining all other conditions. For the Arrhenius parameter measurements, a heating tape was used to increase uniformly the temperature of the reaction cell with a thermocouple installed inside the reaction chamber for recording the gas temperature. Throughout the irradiation, only minimal temperature rise was observed and hence the temperature range of the experiment was recorded as (299±1) K.

The structures of the reactants, products and transition states were optimized using density functional theory at UB3LYP/6-31+G(d) level in Gaussian 03 that the enthalpies, free energies and activation energies of the abstraction processes could be determined. Harmonic frequencies were calculated at the optimized geometries to characterize stationary points as equilibrium structures, with all real frequencies, or transition states, with one imaginary frequency, and to evaluate zero-point energy (ZPE) correction.

4.3 Results and discussion

4.3.1 Concentration Analysis

The Beer-Lambert's Law, Abs = ε c l where Abs = measured Absorbance; l = path length (cm), c is the partial pressure of the absorbing species (Torr) and ε is the molar absorptivity (cm^{-1} $Torr^{-1}$), has been used towards determining the ratio of the products. The absorptivity of the vibrational bands of the products was estimated by calibrating known pressures of pure samples of acetone and t-butanol. The pressures of the two products formed in the abstraction reaction can then be determined. The linear plots for the calibration are shown in Figure 4.1. From the slopes, the concentrations of the two products formed in the reaction can be calculated.

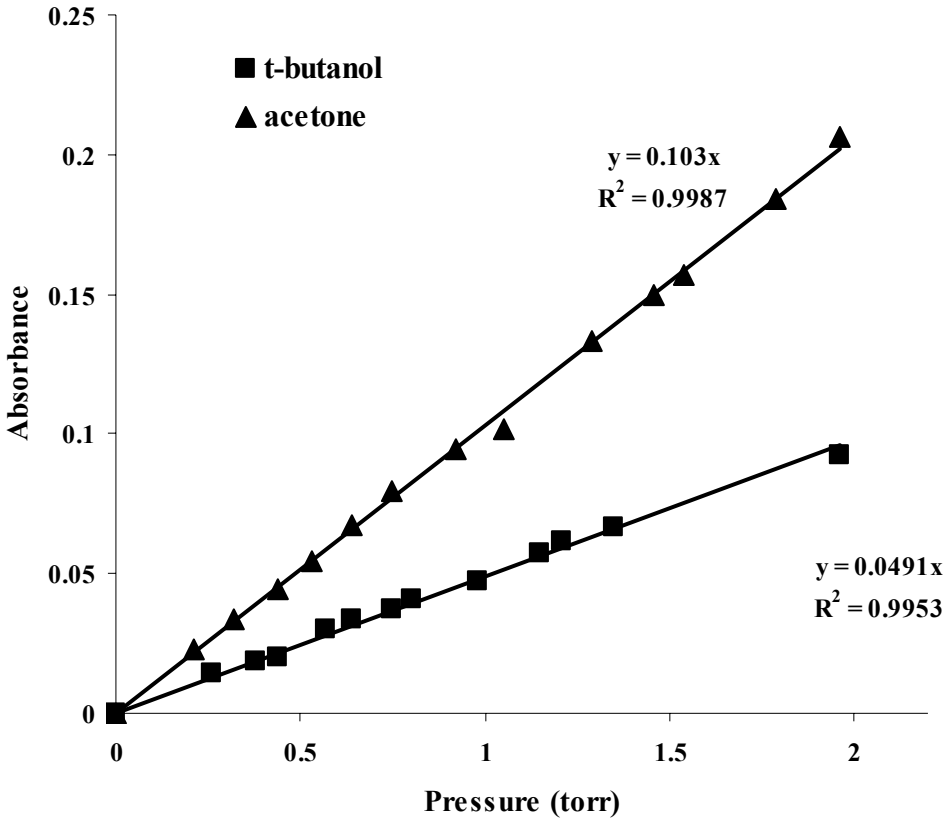

Figure 4.1 Linear plot of absorbance vs concentration of acetone and t-butanol

4.3.2 Reaction of t-butoxy radical with hydrogen donors

A few control experiments were carried out initially. Firstly, upon uv photolysis of a sample containing t-butyl nitrite, the production of only acetone was observed, indicating that unimolecular decomposition of the t-butoxy radical is dominant in the absence of any substrates. Secondly, it was only upon uv lamp photolysis in the presence of both t-butyl nitrite and the substrate that IR signals of acetone and t-butanol began to appear and increased in intensity with respect to the irradiation time.

Based on the simple reaction scheme below and assuming a constant photolysis rate of t-butyl nitrite, the relationship between t-butanol and acetone formation over the irradiation period (Δt) is given by equations 1a-1f [17,18].

$$(CH_3)_3CONO \xrightarrow{h\nu} (CH_3)_3CO + NO \qquad (3)$$

$$(CH_3)_3CO + M \xrightarrow{k_d} CH_3COCH_3 + CH_3 \qquad (4)$$

$$(CH_3)_3CO + RH \xrightarrow{k_a} (CH_3)_3COH + R \qquad (5)$$

$$\frac{d[t-BuOH]}{dt} = k_a[(CH_3)_3CO][donor] \qquad (1a)$$

$$\frac{d[acetone]}{dt} = k_d[(CH_3)_3CO] \qquad (1b)$$

$$[t-BuOH] = k_a[(CH_3)_3CO][donor]\Delta t \qquad (1c)$$

$$[acetone] = k_d[(CH_3)_3CO]\Delta t \qquad (1d)$$

$$\frac{[t-BuOH]}{[acetone]} = \frac{k_a[donor]}{k_d} \qquad (1e)$$

$$k_a = \frac{k_d[t-BuOH]}{[donor][acetone]} \qquad (1f)$$

Under conditions where the t-butoxy radical and substrate concentrations are constant which would occur during the initial stages of irradiation, equations 1a and 1b may be integrated to give 1c and 1d which upon rearrangement lead to an expression for the rate coefficient shown in 1(f). Equations 1a and 1b predict linear productions of t-butanol and acetone and indeed this is shown by the results obtained for the reactions as shown in Figure 4.2. The linear plot demonstrates constant rate of production of t-butoxy radical concentration at low substrate consumption. From the ratio of acetone to t-butanol, the absolute rate coefficients of the H-atom abstraction reactions can be determined since k_d has already been well-documented [7-9]. As nitric oxide is the other product from nitrite photolysis, it may have some effect on the abstraction reactions. Hence another precursor (di-t-butylperoxide) was used to produce t-butoxy radical but essentially the same H-atom abstraction reaction rate coefficients were obtained. From these results, the presence of NO has essentially no effect or at least negligible within the experimental error of the rate coefficients.

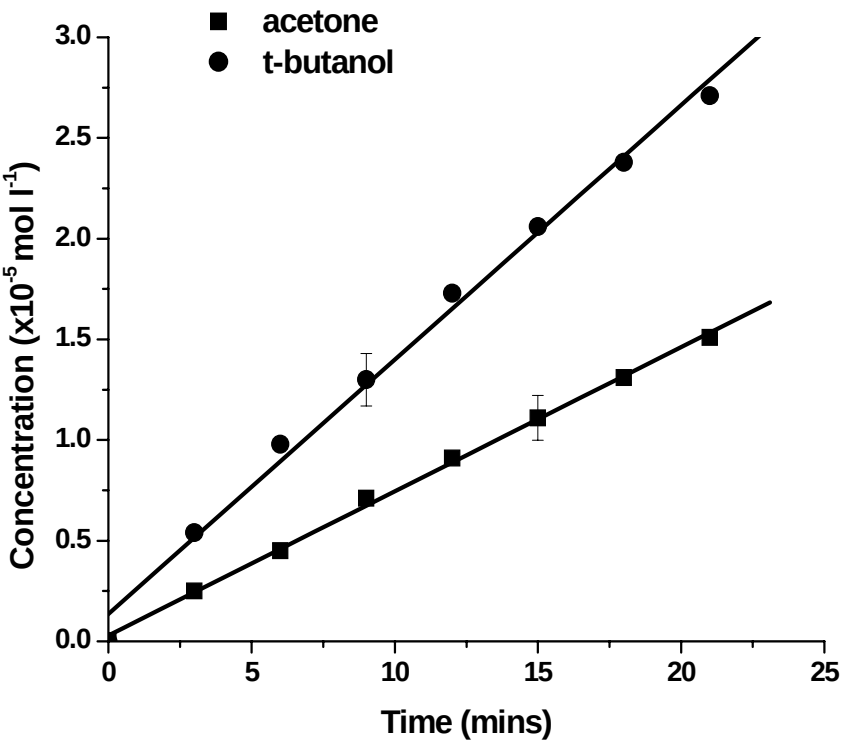

Figure 4.2 Linear production of t-butanol and acetone during the photolysis of t-butyl nitrite (2 Torr) and triethylamine (10 Torr) at 299K. Experimental error is denoted by a vertical bar

The rate coefficients for the abstraction rate of various substrates are shown in Table 4.1. The relative rates depend on the number and type of hydrogen atoms of the substrates in the following order; CH- > -CH_2- > CH_3 which can be explained as due to the generation of the more stable tertiary carbon radicals after abstraction. As expected the rate coefficients for reactions involving halogenated substrates are slightly lower than those for the alkanes because the halogen atoms tend to be electron-withdrawing rendering the radicals less stable. In the case of amines which are electron-donating groups, their reactions with t-butoxy are much faster, in good agreement with the liquid phase values [6]. Although it could not be inferred in our experiments, hydrogen

abstraction reactions from amine preferably take place at the α-carbon attached to the nitrogen atom. Once formed, the α-aminoalkyl radical can be stabilised by the conjugation between the unpaired electron of the α-aminoalkyl radical and the lone paired electron of nitrogen [4, 6].

The kinetic isotopic effect for H/D atoms was also examined for a few of the substrates here. However, when $CDCl_3$ and CD_3CN were used as substrates, the signal of deuterated t-butanol (O-D, 1042 cm^{-1}) was not observed during the irradiation. This indicates that the isotope effect has rendered the abstraction process too slow to be observable using our experimental setup. Since the smallest measurable rate coefficient is about 6 x 10^{-16} $cm^3molecule^{-1}s^{-1}$ for CH_3CN (see Table 4.1), the corresponding rate coefficients for the deuterated substrates would be smaller than this value. In addition, the abstraction rate coefficient values which range from 10^{-16} to 10^{-14} $cm^3molecule^{-1}s^{-1}$ for all the substrates studied here indicate an activation barrier to reaction; otherwise values in the region of 10^{-10} and 10^{-11} $cm^3molecule^{-1}s^{-1}$ would be expected based on simple collision rates. Hence a temperature-dependence study was carried out for a few selected substrates in order to determine their activation barriers.

Table 4.1 Rate coefficients of H-atom abstraction by t-butoxy radical

Precursor	Rate constant (cm^3 $molec^{-1}$ s^{-1})	Precursor	Rate constant (cm^3 $molec^{-1}$ s^{-1})
$(CH_3)_2CHCN$	5.6×10^{-15}	Triethylamine	4.9×10^{-14}
$CHCl_3$	3.8×10^{-15}	$(CH_3)_2NCH_2CH_2NH_2$	4.5×10^{-14}
Hexane	2.7×10^{-15}	Cyclohexyl amine	2.5×10^{-14}
$CHBr_3$	2.7×10^{-15}	$CH_3(CH_2)_4NH_2$	7.8×10^{-15}
CH_2Cl_2	2.5×10^{-15}	$CH_3(CH_2)_3NH_2$	7.8×10^{-15}
$CH_3(CH_2)_2CN$	2.1×10^{-15}	Phenylacetylene	1.4×10^{-15}
1-hexene	1.6×10^{-15}	HNCO	1.4×10^{-15}
Toluene	1.6×10^{-15}	CH_3CN	6.2×10^{-16}
C_2H_2	1.4×10^{-15}		

The Arrhenius plots for the abstraction reaction rate coefficient ratios of triethylamine, chloroform, isobutyronitrile and hexane are shown in Figure 4.3. Based on the measured slopes and the accepted Arrhenius parameters for k_d (log A = 14.1 s^{-1} and E_a = 64.0 kJ mol^{-1}) [9], the activation energies E_a (kJ mol^{-1}) and the pre-exponential factors log A (L mol^{-1} s^{-1}) of these reactions could be calculated and shown in Table 4.2. The activation energy for hexane is in good agreement with previously reported literature values [12-14]. As expected the reaction involving an amine has the lowest barrier while those with electron-withdrawing groups such as Cl and CN tend to have more substantial barriers.

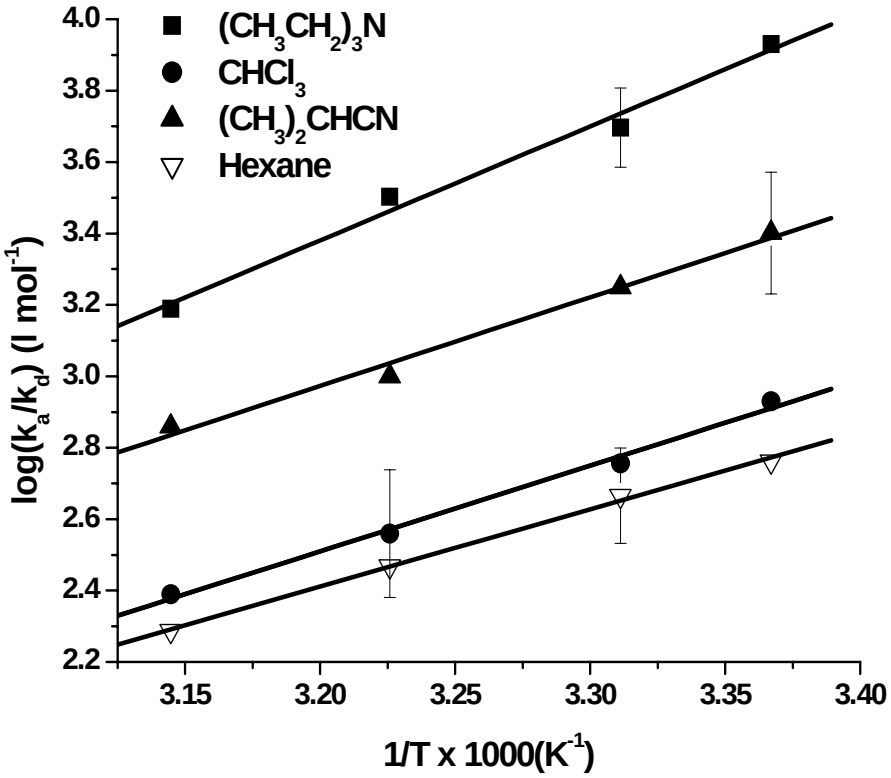

Figure 4.3 Arrhenius plots of k_a / k_d for the reaction of t-butyl nitrite with triethylamine, chloroform, isobutyronitrile and hexane

Table 4.2 Arrhenius parameters for t-butoxy radical

Precursor	Activation energy (kJ mol^{-1})	Log A (L mol^{-1} s^{-1})
$CHCl_3$	18.0 ± 2.5	9.0 ± 0.5
$(CH_3)_2CHCN$	16.5 ± 2.3	8.9 ± 0.3
Triethylamine	2.78 ± 0.6	7.7 ± 0.2
Hexane	21.7 ± 3.4	10.0 ± 0.5

4.3.3 Computational work

Computational studies were performed in order to further understand and substantiate the experimental findings. The calculated enthalpies and Gibbs free energies of selected abstraction reactions at 298K are shown in Table 4.3. A relationship between ΔG and the rate coefficients could be clearly seen from the plot of the rate coefficients versus absolute ΔG (which carry negative signs) in Figure 4.4. Highly exogernic reactions tend to have larger rate coefficients as well. Hence this correlation appears to serve well in predicting rate coefficients for the abstraction reaction. We are also interested in finding out whether these abstraction processes proceed via an elementary step or through a series of reactions. Hence, the energy and geometry of the transition states for the reactions between butoxy radical with $CHCl_3$ and $CDCl_3$ has been computed and compare with the experimental values. These reactions are ideal since the isotopic effect on the reaction rates can also be examined. Figure 4.5 shows such as a transition state (for $CHCl_3$ case) in which the main features lie in the reaction coordinate (1861*i* cm^{-1}) which shows a gradual formation of the O-H (1.22Å) bond and cleavage of the C-H (1.31 Å) bond. These values could be compared to O-H (0.97 Å) and C-H (1.09 Å) values of stable organic molecules. The calculated activation barrier (20.7 kJ mol^{-1}) is just outside the error associated with the experimentally observed barrier (18 ± 2.5 kJ mol^{-1}). Although the transition state geometry for the $CDCl_3$ case is similar, its activation barrier shows a slightly higher value of 25.9 kJ mol^{-1}. The difference of 5.2 kJ mol^{-1}can be loosely translated as a lowering of the rate coefficient by about 8 times assuming the pre-exponential factors of the reactions remain the same over a small temperature range. So both experimental and computational data appear to favour a large kinetic isotope

effect operating during the abstraction reactions. In addition, the computed activation energy of 13.1 kJ mol^{-1} for the reaction between t-butoxy and $(CH_3)_2CHCN$ reactions also agrees well with the experimental value of 16.5±2.3 $kJmol^{-1}$. However similar computation could not be performed for the triethylamine case presumably due to the very low barrier as suggested by experiments hence rendering the location of the transition state uncertain. Nevertheless, it appears that it is sufficient to consider these abstraction reactions as elementary based on the good agreement between the experimental and computed parameters.

Table 4.3 Enthalpies and Gibbs free energies of hydrogen abstraction reactions

Reaction	ΔH(kJ mol^{-1})	ΔG(kJ mol^{-1})
$CHCl_3$	-49.9459	-48.5048
$CHBr_3$	-48.2685	-46.7224
CH_2Cl_2	-19.4355	-20.1259
Hexane	-47.9693	-54.9281
$(CH_3)_2CHCN$	-87.2498	-94.4002
$CH_3CH_2CH_2CH_2NH_2$	-73.4344(from α carbon)	-75.831
$CH_3CH_2CH_2CH_2NH_2$	-183.574(from nitrogen)	-184.986
HNCO	5.305125	2.75625

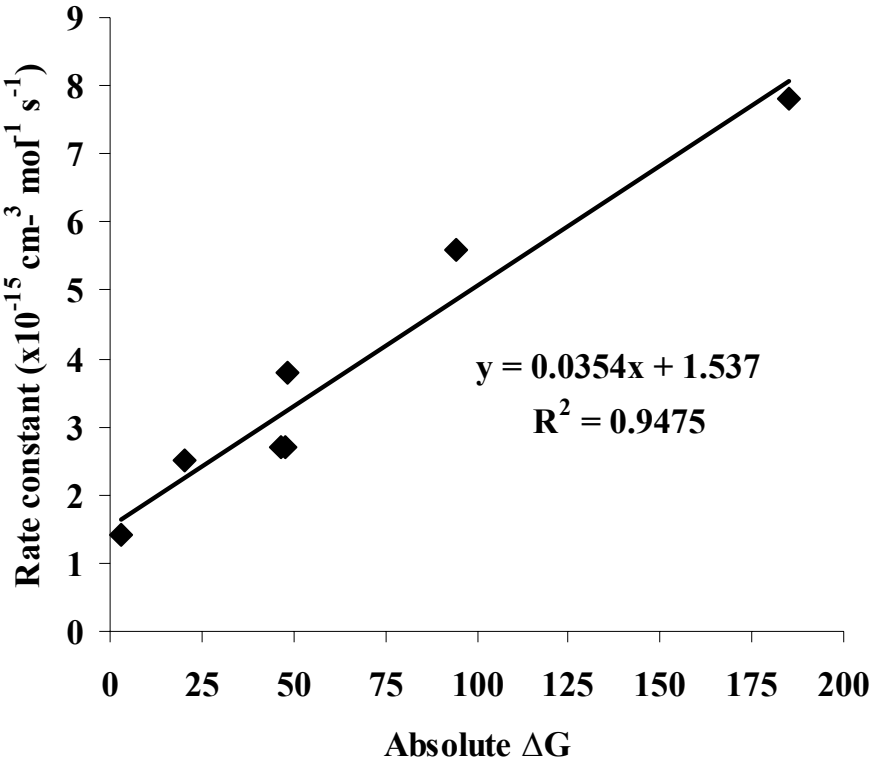

Figure 4.4 Plot of selected hydrogen abstraction rate coefficient vs absolute ΔG

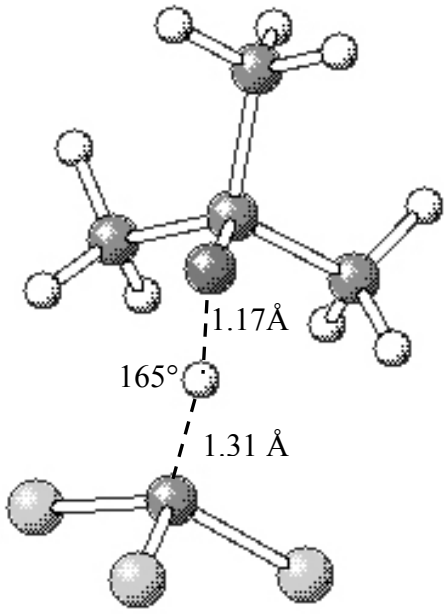

Figure 4.5 Transition state structure for the reaction of t-butoxy radical with $CHCl_3$

4.4 Conclusion

The hydrogen abstraction reactions were investigated for some amines, halogenated organic compounds, nitriles and some unsaturated organic compounds. The rate constants were determined using relative rate method. The kinetic isotopic effect was also evaluated and the possible reasons for the different reactivity of different types of hydrogen donors were also discussed. The Arrhenius parameters for some species such as hexane, chloform, triethylamine and isobutylnitrile are detected.

Reference

1. W. P. L. Carter, K. R. Dornall, A. C. Lloyd, A. M. Winer and J. N. Pitts, Jr., Chem. Phys. Lett., 42, 22, 1976

2. C. T. Pate, B. J. Finlayson and J. N. Pitts, Jr., J. Am. Chem. Soc., 96, 6554, 1974

3. E. A. Lissi and J. Collados, Int. J. Chem. Kinet., 17, 265, 1985

4. D. Griller, J. A. Howard, P. R. Marriott and J. C. Scaiano, J. Am. Chem. Soc., 103, 619, 1981

5. V. Paul, B. P. Roberts and C. R. Willis, J. Chem. Soc. Perkin Trans. II, 1953, 1989

6. P. E. Elford and B. P. Roberts, J. Chem. Soc. Perkin Trans. 2, 1413, 1998

7. L. Batt, M. W. M. Hisham and M. Mackay, Int. J. Chem. Kinet., 21, 535, 1989

8. L. Batt and G. N. Robinson, Int. J. Chem. Kinet., 19, 391, 1987

9. K. Y. Choo and S. W. Benson, Int. J. Chem. Kinet., 13, 833, 1981

10. S. A. Song and K. Y. Choo, Bull. Kor. Chem. Soc., 5, 16, 1984

11. C. R. Park, S. A. Song, Y. E. Lee and K. Y. Choo, J. Am. Chem. Soc., 104, 6445, 1982

12. Y. E. Lee and K. Y. Choo, Int. J. Chem. Kinet., 18, 267, 1986

13. M. I. Sway and D. J. Waddington, J. Chem. Soc. Perkin Tran., II, 63, 1984

14. M. I. Sway, J. Chem. Soc. Faraday Trans., 87, 2157, 1991

15. W. Deng, A. J. Davis, L.Zhang, D. R. Katz and T.Dibble, J. Phys. Chem. A 105, 8985, 2001

16. Frisch et al, Gaussian 03, Gaussian Inc., Wallingford CT, 2004

17. J. A. Franz, D. S. Kolwaite, J. C. Linehan and E. Rosenberg, Organomet., 23, 441, 2004

18. J. A. Franz, J. C. Linehan, J. C. Birnbaum, K. W. Hicks and M. S. Alnajjar, J. Am. Chem. Soc., 121, 9824, 1999

– CHAPTER 5 –

Reaction of O (^{3}P) and Cl ($^2P_{3/2}$) atoms with $CF_3CHOHCF_3$ and CF_3CH_2OH

5.1 Introduction

According to the Montreal Protocol and Amendments, hydrofluorocarbons (HFC) and hydrochlorofluorocarbons (HCFC) have been recommended to replace chlorofluorocarbons (CFC) because of their much less harmful effect on the ozone layer [1-2]. In addition, fluoroalcohols (FA) have also been proposed as a new generation of CFC alternatives in certain industrial applications [3-4] since they contain neither a chlorine or bromine atom. In order to determine the impact of FAs in the atmosphere, their atmospheric lifetimes and the nature and fate of the resulting oxidation products need to be documented. This will depend on the chemical kinetic data for the oxidation processes and information regarding the degradation mechanism. Although tropospheric degradation of fluoroalcohols is expected to occur via reaction with OH radicals [5], significant contributions from reactions with the less abundant but possibly more reactive Cl ($^2P_{3/2}$) and O (^{3}P) atoms cannot be ruled out. Thus, the reactivity of FAs towards these atoms should be examined in order to more fully review their potential impact on the atmosphere.

So far limited information of direct relevance to the environment is available for the Cl($^2P_{3/2}$) or O(^{3}P) atom reactions with 2,2,2-trifluoroethanol (CF_3CH_2OH) and 1,1,1-3,3,3-hexafluoropropanol ($(CF_3)_2CHOH$). Only the rate coefficient for the Cl ($^2P_{3/2}$) atom reaction with CF_3CH_2OH is available [6-7]. The aim of this study is thus to expand the study of these atomic reactions with the two fluoroalcohols. Rate coefficients for the primary reaction will be determined by using broadband uv irradiation to produce the reactive atoms from various sources, coupled with FTIR absorption spectroscopy for detection of both reactants and products. We are also interested in determining secondary products of the reactions and in doing so allow us to explore the mechanism in a semiquantitative manner using both experimental and computational methods (Gaussian 03 software). In particular, the reaction between Cl ($^2P_{3/2}$) and CF_3CH_2OH will be explored in more detail as this is by far the more complicated of the four chemical systems studied here. Most of the reaction pathways relating to this reaction could in fact be applied to the other systems as well.

5.2 Experimental section

The experimental setup has been described in Chapter 2, hence only a brief account of it will be presented here. $(CF_3)_2CHOH$ (99.5%) and CF_3CH_2OH (99.5%) were purchased from Sigma-Aldrich. The freeze-pump-thaw method was carried out on these compounds three times before they were used in subsequent experiments. $(CF_3)_2CHOD$ and CF_3CH_2OD were generated by mixing heavy water (D_2O) and $(CF_3)_2CHOH$ with a ratio of more than 10: 1. Chlorine gas was generated from the reaction of concentrated hydrochloric acid (HCl) with potassium permanganate ($KMnO_4$) solid and the vapour

was then trapped in dry ice-acetone. Nitrogen dioxide (NO_2) (Linde, 99%) gas was available from a gas cylinder and used without further purification. Sulfur dioxide (SO_2) was formed from the reaction of concentrated H_2SO_4 with solid sodium sulfite (Na_2SO_3) solid. The acetylene reference gas, C_2H_2 was synthesized by dropwise addition of distilled water into calcium carbide (CaC_2) solid. Two other references gases, acetone ($(CH_3)_2CO$) and carbon disulfide (CS_2) were purchased from Sigma-Aldrich and freeze-pump-thaw before use.

Cl($^2P_{3/2}$) atoms were produced by photolysing Cl_2 at wavelengths from 300 to 350 nm whereas O (^{3}P) atoms were generated by photolysing either NO_2(> 300 nm) or SO_2 (254 nm). A typical photolysis experiment would begin with the addition of the alcohol (2-5 Torr), one of the precursors for Cl($^2P_{3/2}$) or O(^{3}P) atoms (10-20 Torr), a reference gas (acetone, CS_2 or C_2H_2 (2-4 Torr)) and 1 bar of a buffer gas, Ar (99.99%) or N_2 (99.9%) into a 15cm long Pyrex gas cell placed in the sample compartment of a Nicolet Nexus 870 FTIR spectrometer. For experiments that required a mercury (Hg) lamp (254 nm, 20Watt), a quartz cell of similar size (15 cm long, 2.5 cm diameter) was used instead while maintaining all other conditions. Otherwise a xenon lamp (300-800 nm, 100W) was used for irradiation. Although it is unlikely that the temperature of the cell would increase significantly due to irradiation, a thermocouple was attached on the outer wall of the gas cell in order to record any temperature rise. As expected, the readings suggested an almost constant temperature range of 295 ± 2K throughout the irradiation.

FTIR spectroscopy was used to record the decay and appearance of vibrational bands of the reactants and products upon photolysis [8, 9]. Typically, an IR spectrum (range 500 to 4000 cm^{-1}; resolution 1 cm^{-1}; average 16 scans) was collected at one minute

interval. Whenever possible, we used initial rate measurements to determine the rate coefficients during the early stages of irradiation in order to minimize contributions from secondary reactions caused by product buildup. However the reactants were allowed to decay to completion when the study of the kinetics of secondary products in the reaction cell was carried out.

5.3 Computational studies

All calculations were performed using the Gaussian 03 suite of program. The reaction profiles for the atom reactions with the alcohols were studied using the B3LYP density functional method together with 6-31G(d) basis sets. Spin-restricted calculations were used for closed-shell systems and spin-unrestricted ones (i.e. UB3LYP) for open-shell species. The structures of the reactants, products and transition states were fully optimized at the B3LYP/6-31G(d) level. Harmonic frequencies were calculated at the optimized geometries to characterize stationary points as equilibrium structures, with all real frequencies, or transition states, with one imaginary frequency, and to evaluate zero-point energy (ZPE) correction. The computed vibrational frequencies and ZPE were scaled by 0.96 and 0.98 respectively

5.4 Results and discussion

5.4.1 Relative rate studies

The reaction rate coefficient for the compounds of interest is measured relative to a known rate coefficient of the atom reaction with a reference compound. The equations required for initial rate measurements are contained in the following scheme.

Scheme 1

$$\frac{\ln([A]_0/[A]_t)}{\ln([R]_0/[R]_t)} = k_A/k_R$$

$$\frac{\ln[(A_{0A}/\varepsilon_A l)/(A_{tA}/\varepsilon_A l)]}{\ln[(A_{0R}/\varepsilon_R l)/(A_{tR}/\varepsilon_R l)]} = k_A/k_R$$

$$\frac{\ln(A_{0A}/A_{tA})}{\ln(A_{0R}/A_{tR})} = k_A/k_R$$

where A is the compound of interest and R is the reference compound. $[A]_0$, $[R]_0$, $[A]_t$ and $[R]_t$ are the concentrations or partial pressures of A and R at time = 0 and t respectively. k_A and k_R are the reaction rate coefficients, ε and l are the extinction coefficients and pathlength. Partial pressures are usable as long as the resulting absorbances of the gas scale linearly according to the Beer-Lambert's law. Since this is valid for small absorbances (<0.3), it is desirable to keep the partial pressures of the reactants as low as possible. Finally, since the k_R value is known, the absolute value of the rate coefficient, k_A can easily be extracted.

The error in the rate coefficient measurements is estimated as follows. For example, the relationship between the errors is given by $(\Delta Z/Z)^2 = (\Delta A/A)^2 + (\Delta B/B)^2 + ...$, where ΔZ = overall error in the rate coefficient; Z = average value; $\Delta A/A$ could be for example, the experimental error resulted from two to three repeated measurements and $\Delta B/B$ could be the error carried forward from the literature rate coefficients of the atom reactions with the reference gases. In all cases here, the overall error associated with the rate coefficient measurements was about 10-15%.

Although O(^{3}P) atoms are usually generated upon NO_2 visible light photolysis, our preliminary observation shows that even in the absence of light, both the fluoroalcohols could react with NO_2 to form nitrite species. The nitrites further decompose under 300-400nm light irradiation into a ketone or aldehyde. Therefore, SO_2 was used to generate O(^{3}P) atoms instead by using a 254 nm Hg lamp [10]. The rate coefficients for the O(^{3}P) reactions with CS_2 (1520-1540 cm^{-1}) and C_2H_2 (3200-3400 cm^{-1}) have been measured, hence their use as reference compounds [11,12]. The decays of $(CF_3)_2CHOH$ and CF_3CH_2OH were monitored via their vibrational bands at 900-950 cm^{-1} and Figure 5.1 shows a typical IR spectrum taken of the reaction mixture before and after photolysis, showing the decay of $(CF_3)_2CHOH$ and the appearance of the final products upon atomic reactions. The plot of the decay of $(CF_3)_2CHOH$ vs C_2H_2 according to Scheme 1 in the presence of O(^{3}P) during the early stages of irradiation is shown in Figure 5.2. A linear relationship in the data series suggests the validity of Scheme 1 in which secondary (a) reactions can be considered to be negligible during the initial stages of reaction. Using k_{298K} for O(^{3}P) + C_2H_2 to be 1.5×10^{-13} $cm^3molecule^{-1}s^{-1}$ [12], the rate coefficient for the O(^{3}P) + $(CF_3)_2CHOH$ is determined to be $(5.6 \pm 0.4) \times 10^{-14}$ $cm^3molecule^{-1}s^{-1}$. It is expected that the first step for the reaction involves O(^{3}P) abstracting an H-atom from the carbon center of the alcohol. Because of that, we have also used the deuterated alcohol, $(CF_3)_2CHOD$ to react with O(^{3}P) atoms. Very little change in the rate coefficient is predicted and indeed the value is found to be essentially the same at $(5.5\pm0.5) \times 10^{-14}$ $cm^3molecule^{-1}s^{-1}$.

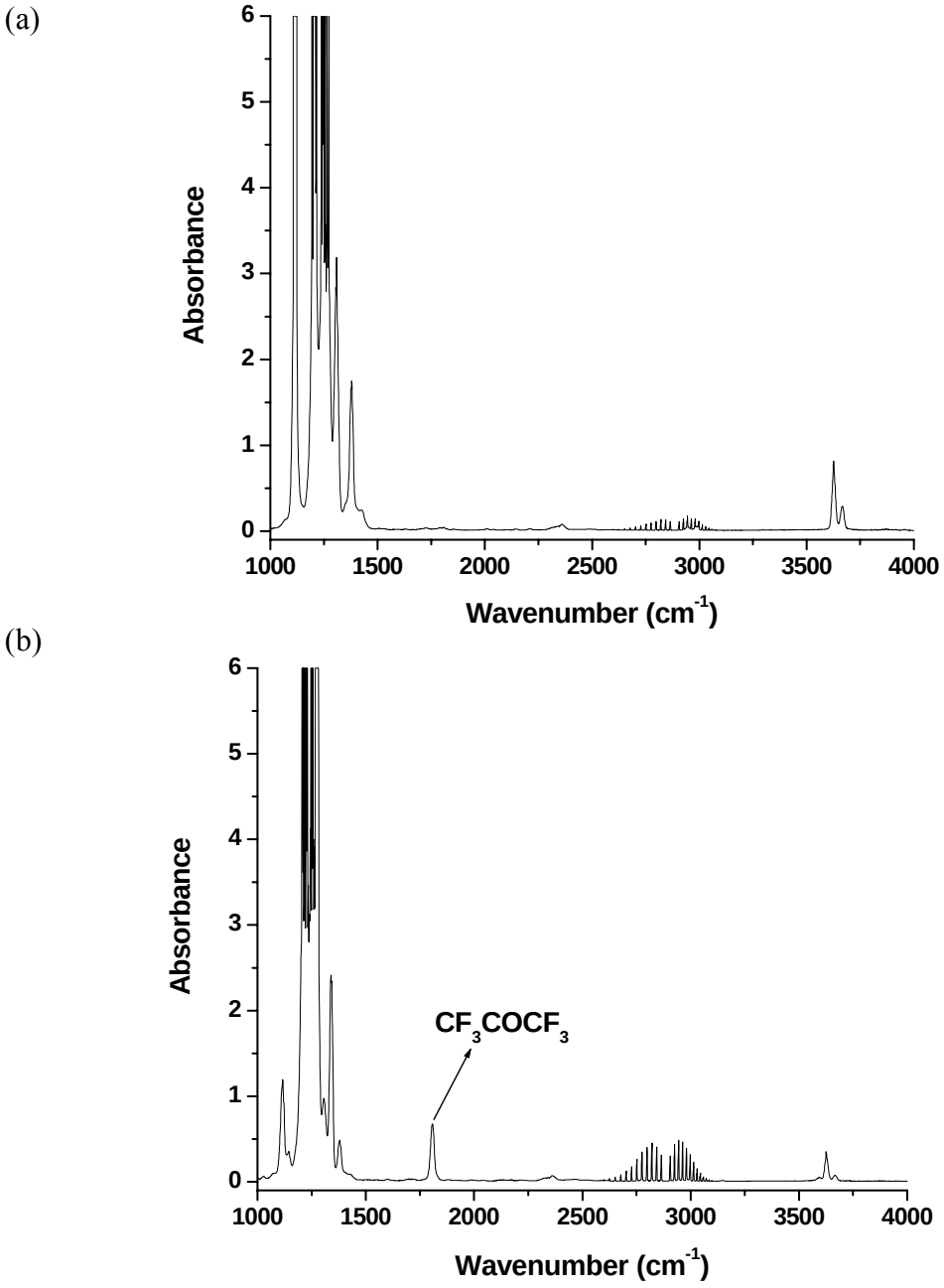

Figure 5.1 FTIR spectrum of $(CF_3)_2CHOH$ (4.0 Torr) + Cl_2 (15 Torr) in Ar buffer gas (≈1 bar) before photolysis (a) and after photolysis (b) The$(CF_3)_2CHOH$ infrared signal showed depletion while the appearance of small signal of main product ($(CF_3)_2CO$, υ_{co}=1806cm^{-1})

(a)

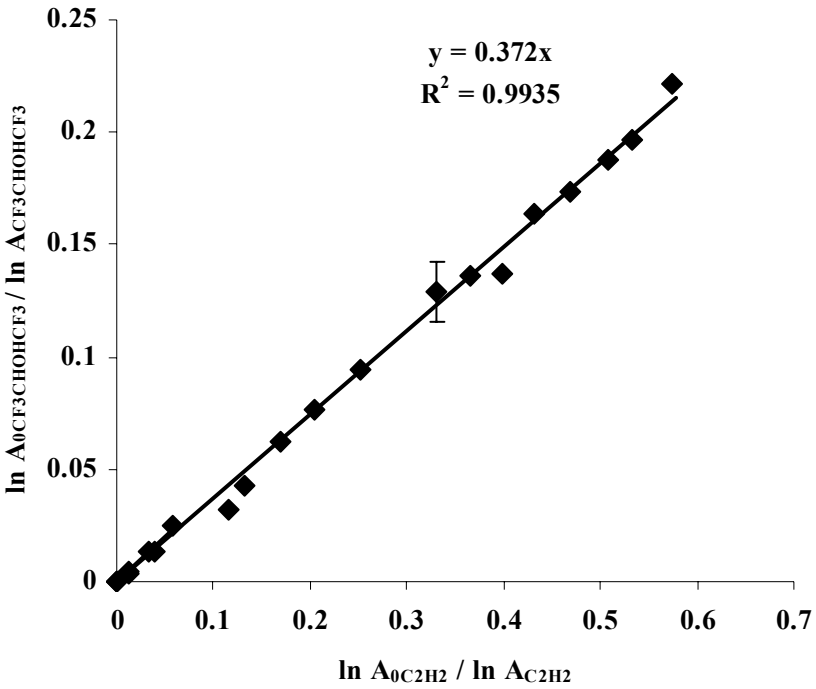

(b)

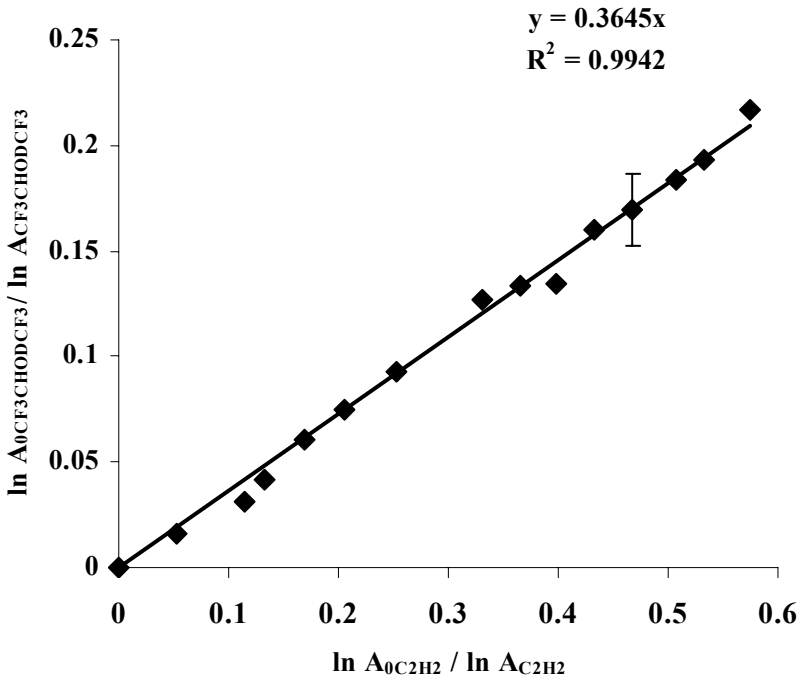

Figure 5.2 Plots of (a) ln A($(CF_3)_2CHOH$) versus ln A(C_2H_2) during uv lamp photolysis of $O(^3P)$/ $(CF_3)_2CHOH$ and (b) ln A($(CF_3)_2CHOD$) versus ln A(C_2H_2) during uv lamp photolysis of $O(^3P)$/ $(CF_3)_2CHOD$

Similarly, the linear plots of the kinetic data for the reaction of $O(^3P)$ with CF_3CH_2OH in the presence of either CS_2 or C_2H_2 reference gas are shown in Figure 5.3a. Again using k_{298K} for $O(^3P)+CS_2$ reaction to be 4.0×10^{-12} $cm^3molecule^{-1}s^{-1}$ [11] and k_{298K} for $O(^3P)+C_2H_2$ to be 1.5×10^{-13} $cm^3molecule^{-1}s^{-1}$ [12], the reaction rate coefficients for $O(^3P) + CF_3CH_2OH$ is determined to be $(6.6\pm0.5) \times 10^{-14}$ $cm^3molecule^{-1}s^{-1}$.

Since the reaction of Cl ($^2P_{3/2}$) atoms with CF_3CH_2OH has been investigated before, we have used this reaction as a standard for our system. The rate coefficient for this reaction was measured using acetone (1365 cm^{-1},527 cm^{-1}) as the reference compound while the decay of CF_3CH_2OH was as usual measured via its vibrational band in the 900-950 cm^{-1} region. A linear plot showing the decay of CF_3CH_2OH vs acetone is displayed in Figure 5.3b. By comparison to the well-known rate coefficient of Cl ($^2P_{3/2}$) reaction with acetone (4.0×10^{-12} cm^3 $molecule^{-1}$ s^{-1}) [13], the rate coefficient for (a) CF_3CH_2OH was determined to be $(7.5 \pm 0.6) \times 10^{-13}$ cm^3 $molecule^{-1}$ s^{-1}. This is in very good agreement with the previously reported value of 7.42×10^{-13} cm^3 $molecule^{-1}s^{-1}$ [6-7].

(a)

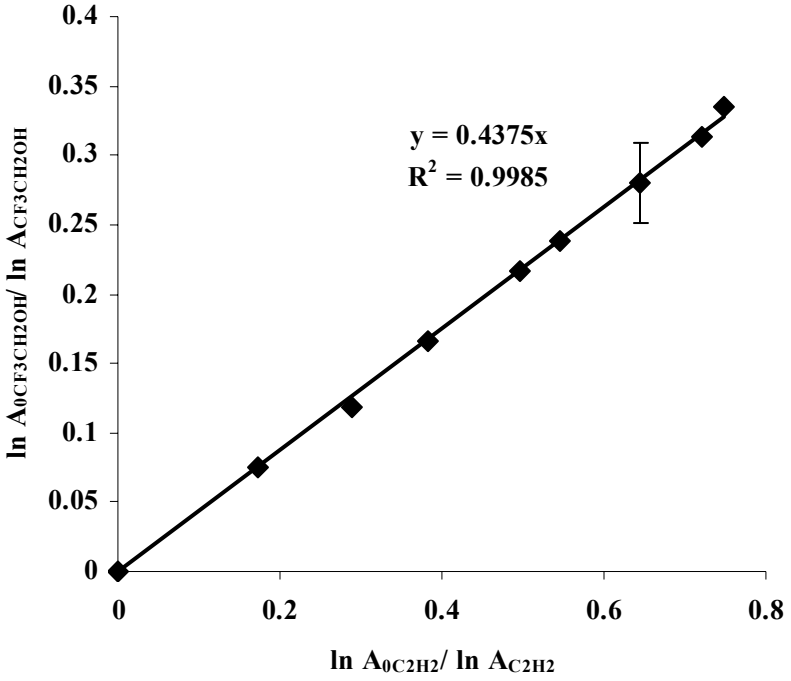

(b)

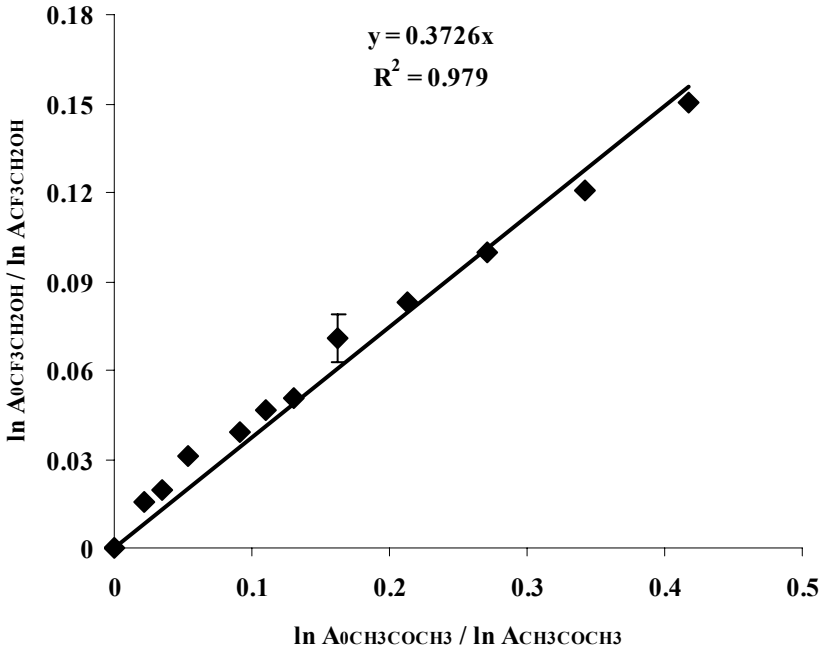

Figure 5.3 Plots of (a) ln $A(CF_3CH_2OH)$ versus ln $A(C_2H_2)$ during uv lamp photolysis of $O(^3P)/CF_3CH_2OH$ and (b) ln $A(CF_3CH_2OH)$ versus ln $A(CH_3COCH_3)$ during uv lamp photolysis of $Cl(^2P_{3/2})/CF_3CH_2OH$

The plots of the decay of $(CF_3)_2CHOH$ and $(CF_3)_2CHOD$ against acetone reference gas in the presence of Cl ($^2P_{3/2}$) atoms during the early irradiation period are shown in Figure 5.4. From the plots, the rate coefficients for the $(CF_3)_2CHOH$ and $(CF_3)_2CHOD$ cases are determined to be (4.9±0.2) x 10^{-13} $cm^3molecule^{-1}s^{-1}$ and (4.8±0.6) x 10^{-13} $cm^3molecule^{-1}s^{-1}$ respectively. Similar to the oxygen reactions, the rate coefficients do not differ significantly indicating that the H-atom is first abstracted from the C-atom of the alcohol.

5.4.2. Stable product analysis

The reaction between Cl ($^2P_{3/2}$) with CF_3CH_2OH is by far the most complicated in terms of the number of detected products. They include CF_3CClO (ν_{co} = 1810 cm^{-1}) [14], CCl_2O (ν_{co} = 1839cm^{-1}) [10], CO (ν_{co} = 2143 cm^{-1}) and HCl (2885 cm^{-1}). The decay of CF_3CH_2OH and the appearances of these products versus time are shown in Figure 5.5. The infrared signals of these stable products show a continuous increase in intensity throughout irradiation. On the other hand, species such as CF_3CHO (ν_{co} = 1787 cm^{-1}) and HCClO (ν_{co} = 1784 cm^{-1}) [10] show different kinetic profiles. Their concentrations tend to reach a maximum and then decrease towards the end of the irradiation.

(a)

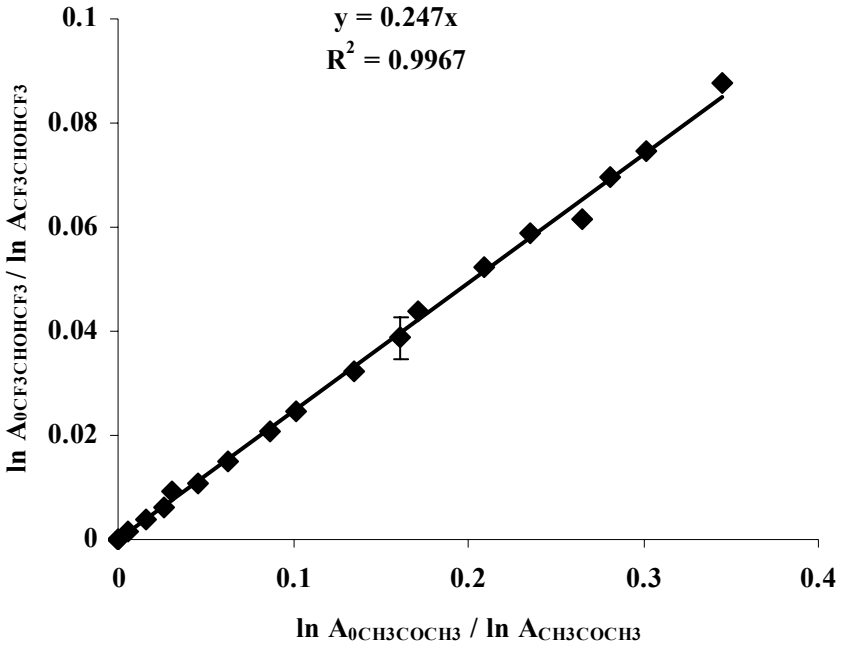

(b)

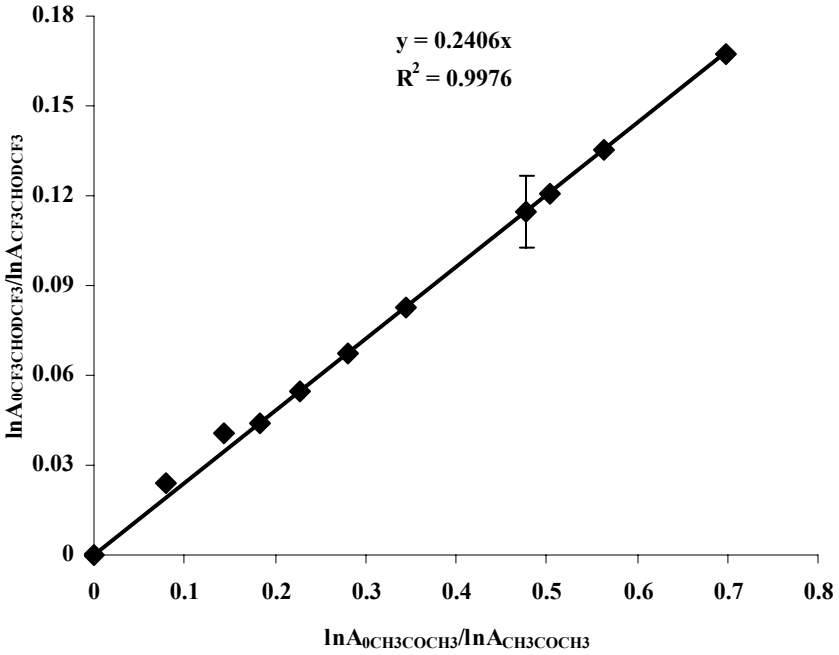

Figure 5.4 Plots of (a) ln A($(CF_3)_2CHOH$) versus ln A($(CH_3)_2CO$) during uv lamp photolysis of $Cl(^2P_{3/2})$/$(CF_3)_2CHOH$ and (b) ln A($(CF_3)_2CHOD$) versus ln A($(CH_3)_2CO$) during uv lamp photolysis of $Cl(^2P_{3/2})$/ $(CF_3)_2CHOH$

(a)

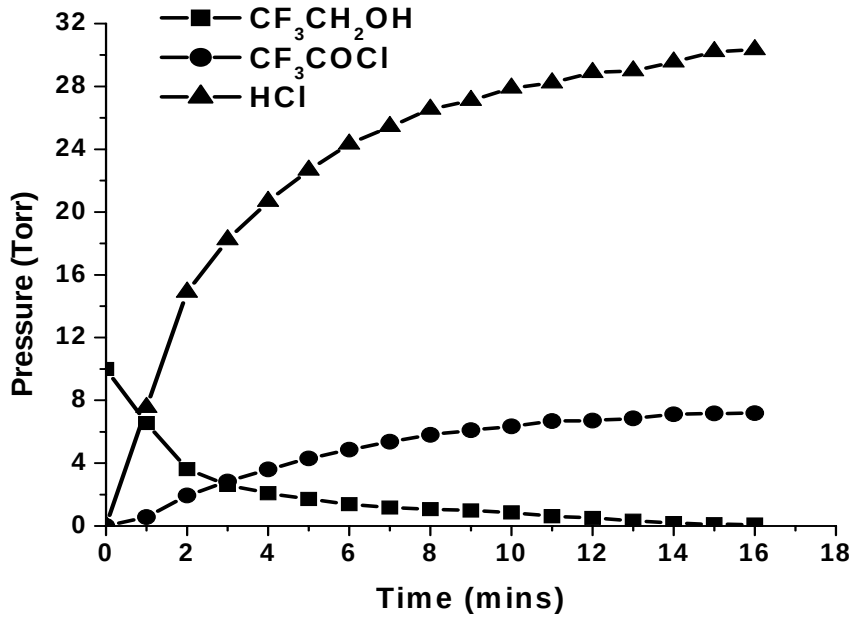

(b)

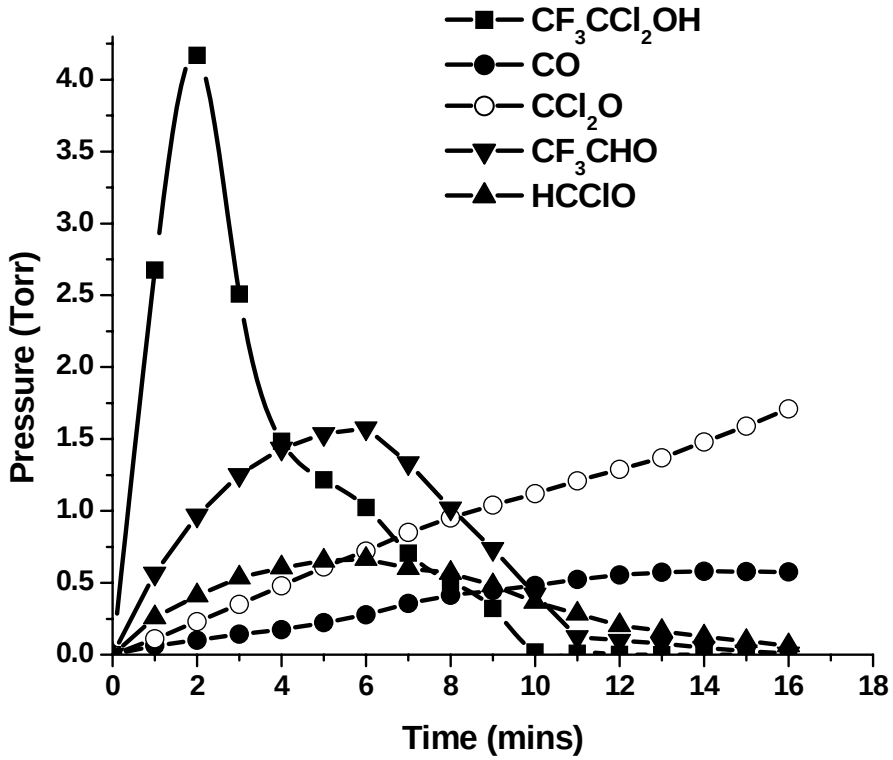

Figure 5.5 The decay of CF_3CH_2OH and the appearance of (a) the major products and (b) minor products against irradiation vs time in the presence of Cl ($^2P_{3/2}$). The pressure of CF_3CCl_2OH was obtained from mass balance and represents its maximum value

We have employed computational studies using Gaussian 03 software to further understand and substantiate the experimental findings of the above reaction. Density functional theory (DFT) method of UB3LYP and 6-31G(d) basis sets have been used for the optimization of the structures and energies of reactive intermediates and transition states. There are many reaction pathways involved in the computation and they are depicted in Figures 5.6 to 5.13. The choice of reaction pathways employed here are based on what are known about Cl($^2P_{3/2}$) reactions with alcohols. For example, an H-atom is preferentially abstracted from the weaker C-H bond rather than the O-H bond of the same alcohol. Radical-radical recombination reactions are generally not considered because of their low concentrations although such reactions have no activation barrier. On the other hand, radical reactions with the much more abundant Cl_2 molecules which also possess either zero or a small activation barrier are expected to be dominant. Only gas-phase reactions have been included in the calculations although surface processes have been known to play an important role. This is because the lack of surface kinetics data and the structural uncertainty of the surface transition state impede any reliable calculations from being conducted.

The reaction is initiated when Cl($^2P_{3/2}$) atom abstracts an H-atom attached to the C-atom of CF_3CH_2OH **[A]** to form the CF_3CHOH radical **[C]** (Figure 5.6). A transition state **[B]** showing the abstraction process along a quasilinear trajectory is found at an energy 8.3 kJ mol^{-1} lower than the reactants. The exothermicity of the reaction increases to 28.36 kJ mol^{-1} once the CF_3CHOH radical and HCl are fully formed. Two possible reactions involving CF_3CHOH are considered here; firstly with Cl_2 molecule and secondly its unimolecular isomerization where the H atom migrates from the O-atom to

the C-atom. The reaction with Cl_2 to form a chlorinated alcohol, $CF_3CH(Cl)OH$ **[G]** has been found with a transition state being 99.28 kJ mol^{-1} lower in energy compare to the immediate reactants. The overall exothermicity of the reaction is large (101 kJ mol^{-1}) upon complete formation of $CF_3CH(Cl)OH$ **[G]**. On the other hand, the activation energy for the gas-phase isomerization process is large (169.74 kJ mol^{-1}) and could not compete with the bimolecular reaction with Cl_2. Although a barrierless radical-radical recombination of CF_3CHOH with Cl atom is possible, we have ruled it out because of the expected low concentrations of radical species in the reaction cell. Furthermore, the reaction with the much more abundant Cl_2 molecule is also a barrierless reaction and would therefore have expected to possess a much larger reaction rate.

Figure 5.7 shows the reaction pathways originating from the $CF_3CH(Cl)OH$ **[G]** alcohol. Three pathways have been computed namely a gas-phase unimolecular elimination of HCl to form CF_3CHO **[K]**, and H-atom abstractions from either the C- or O- atom of the chloroalcohol by Cl($^2P_{3/2}$). While a purely gas-phase HCl elimination reaction has been computed to have a very high activation barrier at 162.14 kJ mol^{-1}, the activation energies for H-atom abstraction by Cl ($^2P_{3/2}$) from the C- and O-atom of the chloroalcohol are much lower at 11.66 kJ mol^{-1} and 27.72 kJ mol^{-1} respectively. It is interesting to note that these two Cl-atom abstraction processes possess activation barriers as compare previously to the barrierless case for the reaction of Cl($^2P_{3/2}$) with CF_3CH_2OH. This is attributed to the presence of the electron-withdrawing Cl-atom in the alcohol which renders the main radical product, CF_3CClOH **[M]** to be less stable than its non-chlorinated counterpart, CF_3CHOH **[C]**. The overall exothermicities of the three processes have been compared and found to favour the Cl($^2P_{3/2}$) abstraction reaction from

the C-atom also. However the unimolecular elimination of HCl process may not occur entirely in the gas phase. Previous reports have suggested that for some alcohols, the pathway is promoted or catalysed by surfaces. In fact this is considered a dominant pathway to account for certain products in the reaction chamber [15-16]. Unfortunately we have been unable to calculate the activation barrier for the surface-mediated case since the nature of the transition state on the surface is not known. Although the product of the elimination process, CF_3CHO **[K]**, has been detected in the reaction chamber, it could not be taken as convincing evidence of the occurrence of the elimination pathway because the aldehyde can also be generated through other pathways, as discussed later.

Figure 5.8 shows the reaction pathways originating from the CF_3CClOH **[M]** radical, species formed from the lowest energy process mentioned in the preceding paragraph. Its reaction with Cl_2 molecules is expected to be dominant and indeed a transition state of lower energy (-75.7 kJ mol^{-1} compare to reactants) has been found which eventually yield a dichloroalcohol, CF_3CCl_2OH **[S]** as the main product. Similar to the $CF_3CH(Cl)OH$ **[G]** case, the newly-formed dichloroalcohol may also undergo HCl elimination, either in the gas phase or through surface-mediated processes. Its further reaction with Cl atom is also possible in which the final H-atom of the OH bond undergoes abstraction. As expected the purely gas-phase elimination of HCl has been computed to possess a large barrier of 129.50 kJ mol^{-1}. However the abstraction reaction with Cl($^2P_{3/2}$) has a smaller barrier of 33.09 kJ mol^{-1} and hence would preferentially proceed to give a CF_3CCl_2O **[V]** radical species.

Figure 5.9 shows the various decomposition pathways of the CF_3CCl_2O **[V]** radical. Unlike other radicals that contain a C-H bond, the CF_3CCl_2O radical is not

expected to react with Cl_2 molecule to form an O-Cl bond. Such reaction has not been observed for alkoxy radicals before. Therefore only the unimolecular decomposition of the radical is considered here. There are two pathways by which the decomposition could take place; either the middle C-C bond or one of the C-Cl bonds dissociates. Calculations seem to favour the latter by a difference of 19.32 kJ mol^{-1} in the activation energy, hence yielding CF_3CClO **[Q]** as the stable product [17]. CF_3CClO does not react any further with Cl atoms.

Based on the analysis of the lowest energy pathways of the reaction scheme so far, only the formation of the main product, CF_3CClO could be accounted for. This itself matches quite well with the experimental data in which with the exception of HCl, it is by far the most abundant species in the reaction cell. In order to account for the remainder of the products, some of the more energetic pathways need to be considered.

We have already shown in Figure 5.7 that the production of the CF_3CHClO **[L]** radical from Cl($^2P_{3/2}$) abstraction of $CF_3CH(Cl)OH$ has the second lowest activation barrier at 27.72 kJ mol^{-1}. Assuming that this pathway is also open under our experimental conditions, the presence of the rest of the detected stable products can be accounted for. Among the three unimolecular decomposition pathways of the radical (Figure 5.10), it is found that HClCO **[R]** could be generated via its C-C bond dissociation pathway, which also happens to be the most exothermic one. This in fact, represents the only way within our reaction scheme to account for the presence of HClCO **[R]** without considering any surface-mediated reactions. The decomposition barrier of 48.52 kJ mol^{-1} is only about 8 kJ mol^{-1} higher than the lowest barrier for the process that produces CF_3CHO **[K]** as the main product. This has also been supported by a previous experimental report [17] which

showed that CF_3CHClO radical could undergo C-Cl and C-C fission to form CF_3CHO and HClCO respectively. The third decomposition pathway which requires a C-H bond cleavage has been computed to have a much higher barrier and therefore is unlikely to occur.

Reactions of Cl($^2P_{3/2}$) atoms with CF_3CHO and HClCO need to be considered as well because the experimental data have shown that these two species can undergo further decay during the irradiation period after reaching their respective optimal concentrations. The energetics and transition state structures for the reactions of Cl ($^2P_{3/2}$) atoms with these aldehydes are shown in Figures 5.11 and 5.12. As expected the H-atom of CF_3CHO is efficiently abstracted by Cl($^2P_{3/2}$) and eventually forming the CF_3CO **[AA]** radical. Further reactions with Cl_2 molecules forming CF_3CClO as the end product appear to be the more favourable loss pathway for CF_3CO compare to the gas-phase unimolecular decomposition to CF_3 and CO **[CC]**. As for HClCO, it is also subjected to H-atom abstraction by Cl atom forming the ClCO **[DD]** radical. In a similar manner, this radical can undergo two major reactions; its reactions with Cl_2 molecule to form CCl_2O **[Y]** being the preferred one. There is yet another source of CCl_2O which simply originates from the reaction between CO and Cl_2 molecules. In a separate experiment where a mixture of CO/Cl_2 was irradiated, the Cl atoms produced could also react with CO and form CCl_2O as the final product. The process proceeds through the formation of the reactive ClCO intermediate as previously reported [18-19]. Overall, the pathways discussed have been able to account for all the known products detected in the reaction cell.

Interestingly, we have also detected a new O-H stretching vibration at 3613 cm^{-1} which could not be assigned to the parent CF_3CH_2OH alcohol. Upon further investigation, a total of seven other vibrational bands across the IR spectrum have been observed to show the same time-dependence profile as the O-H band during irradiation (Figure 5.13). The concentration of the alcohol is observed to increase to a maximum and then decay slowly, unlike the profile of CF_3CHO and HClCO. The loss of the alcohol appears to follow first-order kinetics and k_{diss} equals to 3.6×10^{-3} s^{-1} under our experimental conditions. This value turns out to be very close to the one obtained for the decomposition of chloromethanol, $ClCH_2OH$ [15]. In our overall reaction scheme, two closed-shell alcohols, $CF_3CH(Cl)OH$ and CF_3CCl_2OH have been proposed as intermediates and hence they are the plausible candidates as the carrier of these unknown IR bands. The choice of the carrier also depends on the relative reactivities of the alcohols. The less reactive species will tend to possess a higher concentration and hence enhances its detectability within the sensitivity limits of the FTIR spectrometer. We believe that the dichloroalcohol should be more stable since it contains only one abstractable H-atom of its O-H bond and indeed from calculations, it has been shown to possess a higher activation barrier to reaction (33.09 kJ mol^{-1}) compare to the $CF_3CH(Cl)OH$ case (11.66 kJ mol^{-1}). Hence we have tentatively assigned the carrier of the IR bands to CF_3CCl_2OH.

Based on similar arguments, the stable product analysis for the other three systems can be carried out. The main product detected throughout the irradiation period for the O(^{3}P) + $(CF_3)_2CHOH$ or $(CF_3)_2CHOD$ reaction is hexafluoroacetone $(CF_3)_2CO$ (ν_{CO}=1806 cm^{-1}) [10]. A simple pathway accounting for the experimental observation as

observed in previous studies of $O(^3P)$ reaction with aliphatic alcohols [20-21] is given in Scheme 2.

Scheme 2

$(CF_3)_2CHOH + O \rightarrow (CF_3)_2COH$

$(CF_3)_2COH + O \rightarrow (CF_3)_2CO$

For the $O(^3P)$ + CF_3CH_2OH reaction, the major product detected is trifluoroaldehyde, CF_3CHO together with a small amount of carbonyl fluoride, CF_2O (ν_{CO}= 1948 cm^{-1}) [10] and carbon monoxide, CO (ν = 2143 cm^{-1}). The aldehyde is produced in essentially the same way as for the $(CF_3)_2CO$ case, namely through two sequential H atom abstractions of CF_3CH_2OH by O atoms. However the CF_3CHO species could still react further since it has available another H atom. Once the only H atom is abstracted from the aldehyde, the trifluoromethoxy (CF_3CO) radical will be formed. Collision-induced unimolecular decomposition of the radical will then generate CF_3 and CO. CF_2O and F are formed when the reactive CF_3 radical reacts with an O atom as shown in Scheme 3 below;

Scheme 3

$CF_3CH_2OH + O = CF_3CHOH + OH$

$CF_3CHOH + O = CF_3CHO + OH$

$CF_3CHO + O = CF_3CO + OH$

$CF_3CO + M = CF_3 + CO$

$CF_3 + O = CF_2O + F$

Finally for the $Cl(^2P_{3/2})$ reaction with $(CF_3)_2CHOH$ or $(CF_3)_2CHOD$, the hexafluoroacetone $(CF_3)_2CO$ is the main product for both reactions together with HCl or

DCl. Although the same final product was observed, the reaction pathways proposed for the Cl reactions somewhat differ from the corresponding O atom pathways, as shown in Scheme 4.

Scheme 4

$(CF_3)_2CHOH + Cl \rightarrow (CF_3)_2COH + HCl$

$(CF_3)_2COH + Cl_2 \rightarrow (CF_3)_2CClOH + Cl$

$(CF_3)_2CClOH \rightarrow (CF_3)_2CO + HCl$ (possibly surface-mediated)

$(CF_3)_2CClOH + Cl \rightarrow (CF_3)_2CClO + HCl;$

$(CF_3)_2CClO \rightarrow (CF_3)_2CO + Cl$

In this scheme, an intermediate chloroalcohol $(CF_3)_2CClOH$ is believed to have been formed upon reaction of Cl_2 molecule with the $(CF_3)_2COH$ radical made in the first step. The reaction can then progress either through a surface-mediated elimination of HCl from this intermediate to generate $(CF_3)_2CO$ immediately. This is the pathway that chloroalcohols are believed to take in order to account for the difficulty in their detection within the reaction cell [15-16]. However in the presence of Cl atoms, it is more likely that the chloroalcohol decays via further abstraction reactions with these reactive atoms. This time, the H-atom attached to its OH bond may be abstracted to form a chloroalkoxy radical. Unimolecular decomposition of the alkoxy radical via its C-Cl bond cleavage will then generate $(CF_3)_2CO$. Although the abstraction reaction at the O-center is certainly endothermic, it would still be favoured if the activation barrier is lower than the HCl elimination process, as we have laready discussed for the Cl ($^2P_{3/2}$) + CF_3CH_2OH reaction.

5.5 Conclusion

To our knowledge, there are no rate constant data available for the reactions of the title alcohol with O(^{3}P) and Cl ($^2P_{3/2}$) except the CF_3CH_2OH. There are two papers [6-7] reporting the rate coefficient for the reaction of Cl ($^2P_{3/2}$) with CF_3CH_2OH which can be compared with our reaction rates. The room-temperature rate constant of Cl atoms are faster than those of O (^{3}P) atoms. The kinetic results are collected in Table 5.1.

Table 5.1 Rate coefficients for the reaction of O (^{3}P) and Cl ($^2P_{3/2}$) atoms with the title alcohols at 298K

Molecule	k_{Cl}(cm^3 $molecule^{-1}$ s^{-1})	k_O(cm^3 $molecule^{-1}$ s^{-1})
$CF_3CHOHCF_3$	$(4.9 \pm 0.15) \times 10^{-13}$	$(5.6 \pm 0.4) \times 10^{-14}$
$CF_3CHODCF_3$	$(4.8 \pm 0.6) \times 10^{-13}$	$(5.5\pm 0.5) \times 10^{-14}$
CF_3CH_2OH	$(7.5 \pm 0.6) \times 10^{-13}$	$(6.6 \pm 0.5) \times 10^{-14}$
CCl_3CH_2OH	$(3.1 \pm 0.3) \times 10^{-12}$	$(1.6 \pm 0.2) \times 10^{-13}$

Environmental concerns from the release of FAs in the atmosphere may arise either from their global warming potential and/or from the possible negative environmental impact of their degradation products. The atmospheric degradation of the title alcohols will lead primarily to the formation of aldehyde or ketone (showing in Table 5.2) which in principle are benign to the environment.

Table 5.2 Final products for the title alcohol reactions with $Cl(^2P_{3/2})$ and $O(^3P)$ atoms

Atoms	Molecule	Products
$O(^3P)$	$CF_3CHOHCF_3$	CF_3COCF_3
	$CF_3CHODCF_3$	CF_3COCF_3
	CF_3CH_2OH	CF_3CHO, CF_2O, CO
$Cl\ (^2P_{3/2})$	$CF_3CHOHCF_3$	CF_3COCF_3, HCl
	$CF_3CHODCF_3$	CF_3COCF_3, DCl, HCl
	CF_3CH_2OH	CF_3CHO, CF_3CClO, HCClO, CF_3CCl_2OH, CCl_2O, CO, HCl

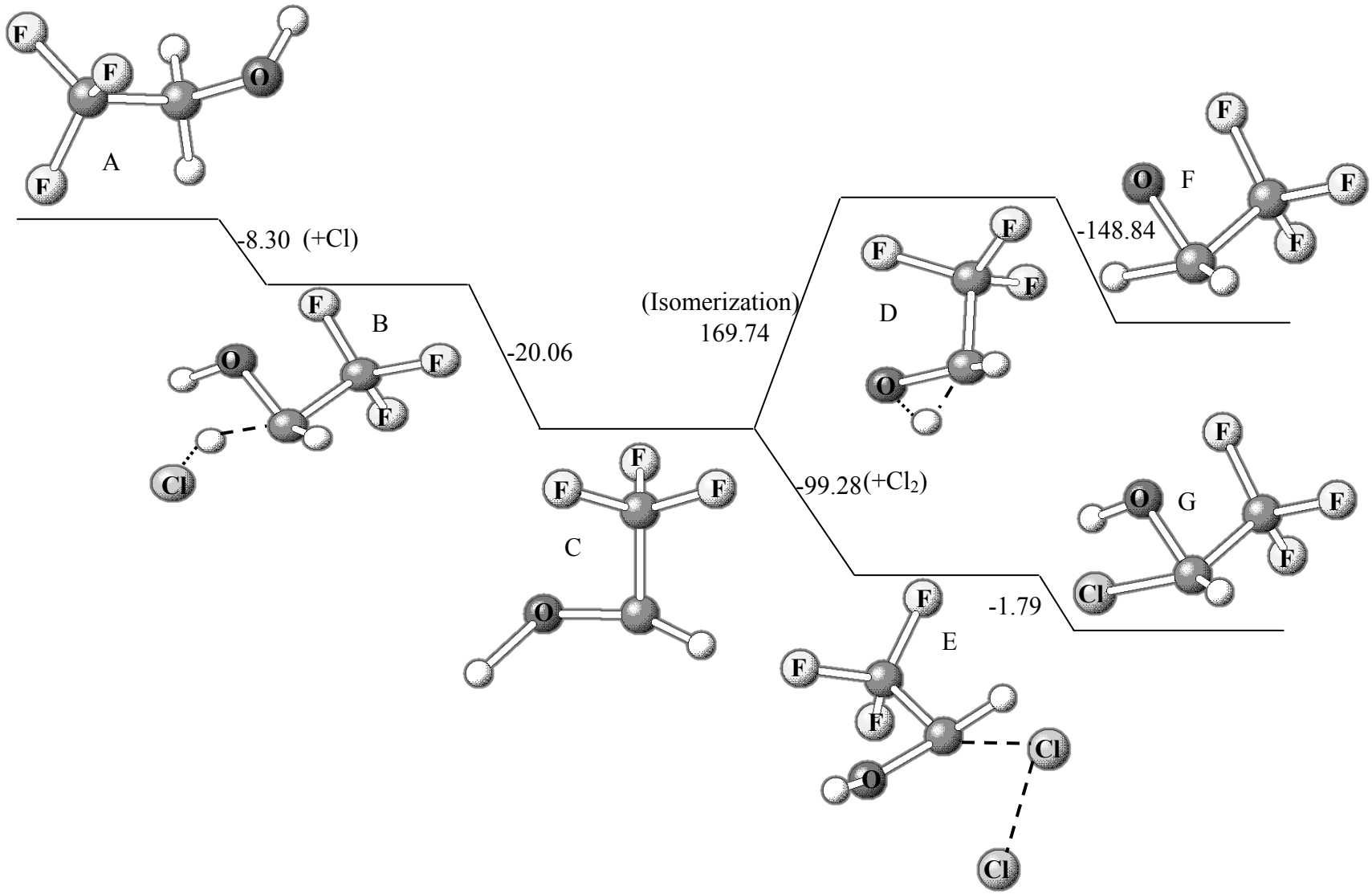

Figure 5.6 Reaction pathways, intermediates and transition states from CF_3CH_2OH to $CF_3CHClOH$ computed at UB3LYP/6-31G(d) level of theory. Energy values are in kJ mol^{-1}

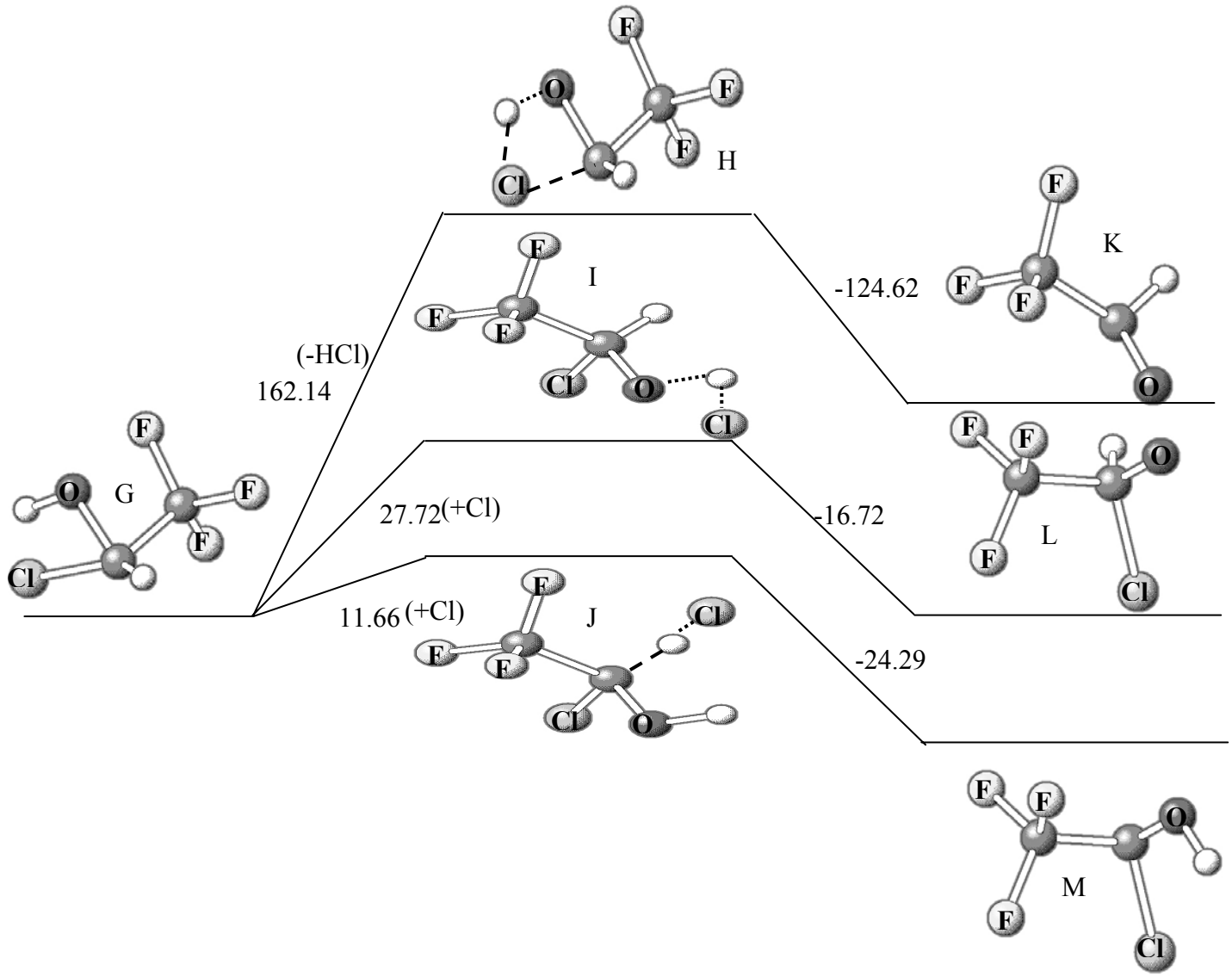

Figure 5.7 Reaction pathways, intermediates and transition states from $CF_3CHClOH$ to CF_3CClOH radical computed at UB3LYP/6-31G(d) level of theory. Energy values are in kJ mol^{-1}

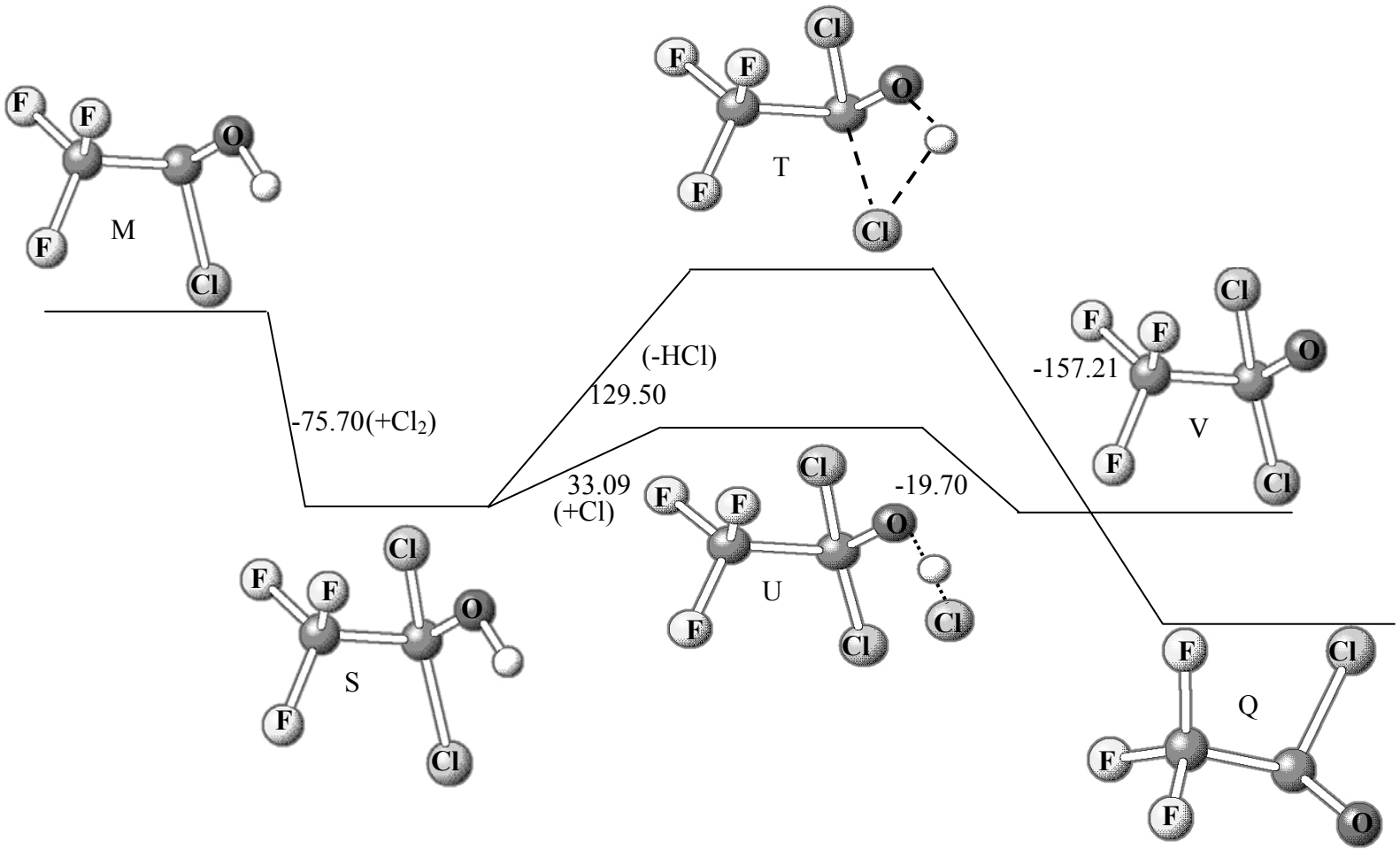

Figure 5.8 Reaction pathways, intermediates and transition states from CF_3CClOH radical to CF_3CCl_2O computed at UB3LYP/6-31G(d) level of theory. Energy values are in kJ mol^{-1}

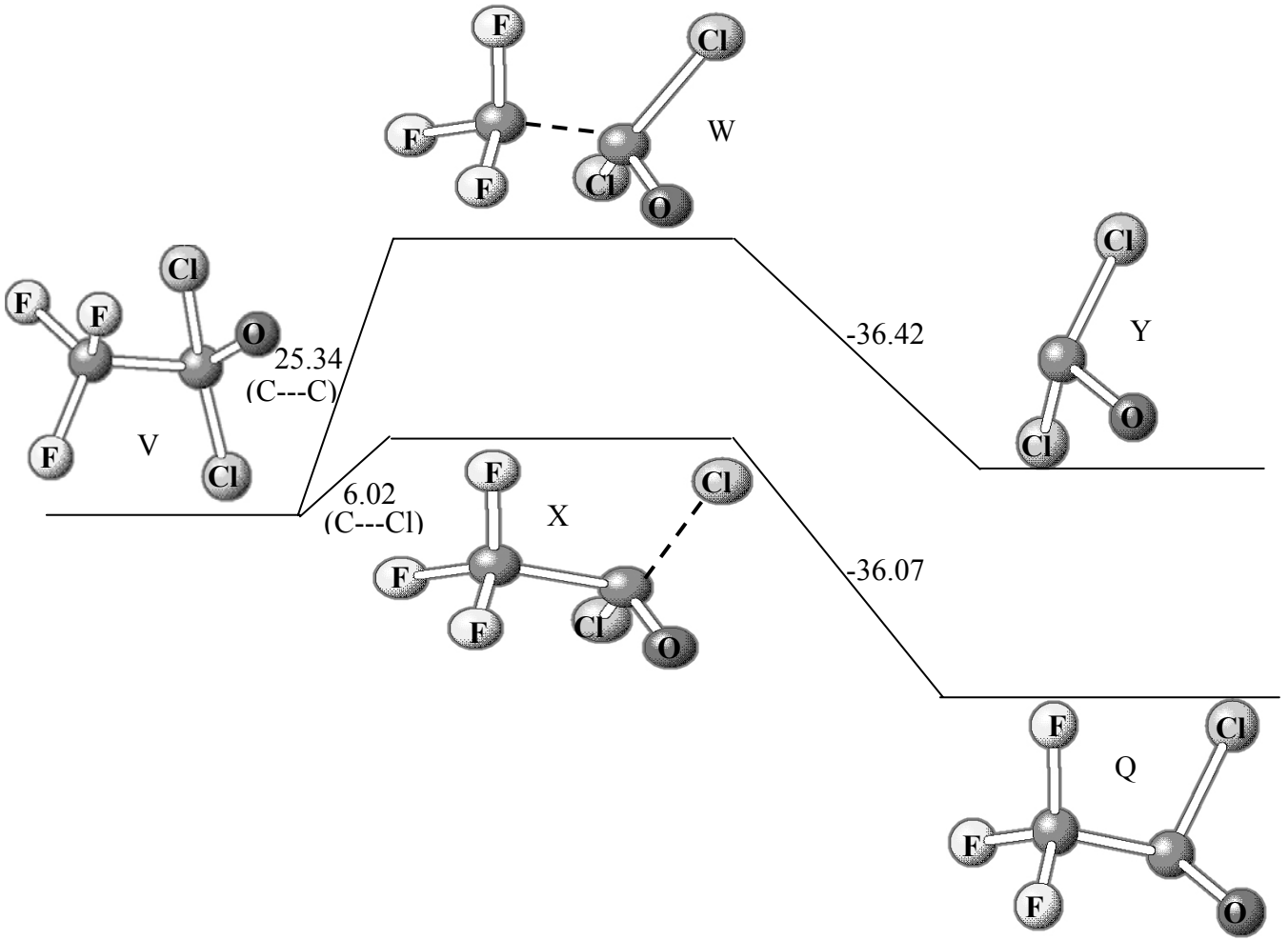

Figure 5.9 Reaction pathways, intermediates and transition states for unimolecular decomposition of CF_3CCl_2O radical computed at UB3LYP/6-31G(d) level of theory. Energy values are in kJ mol^{-1}

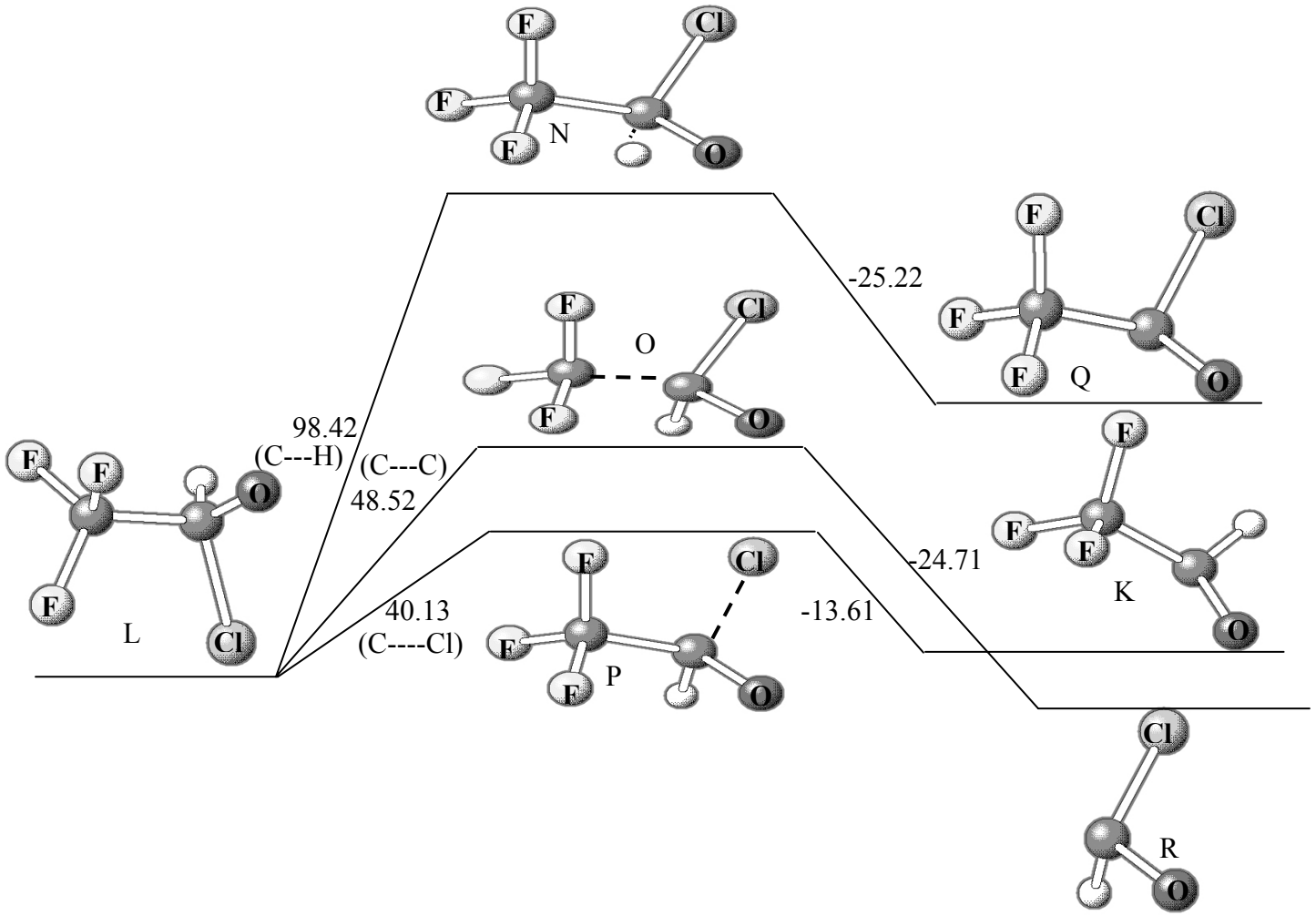

Figure 5.10 Reaction pathways, intermediates and transition states for the unimolecular decomposition of CF_3CHClO radical computed at UB3LYP/6-31G(d) level of theory. Energy values are in kJ mol^{-1}

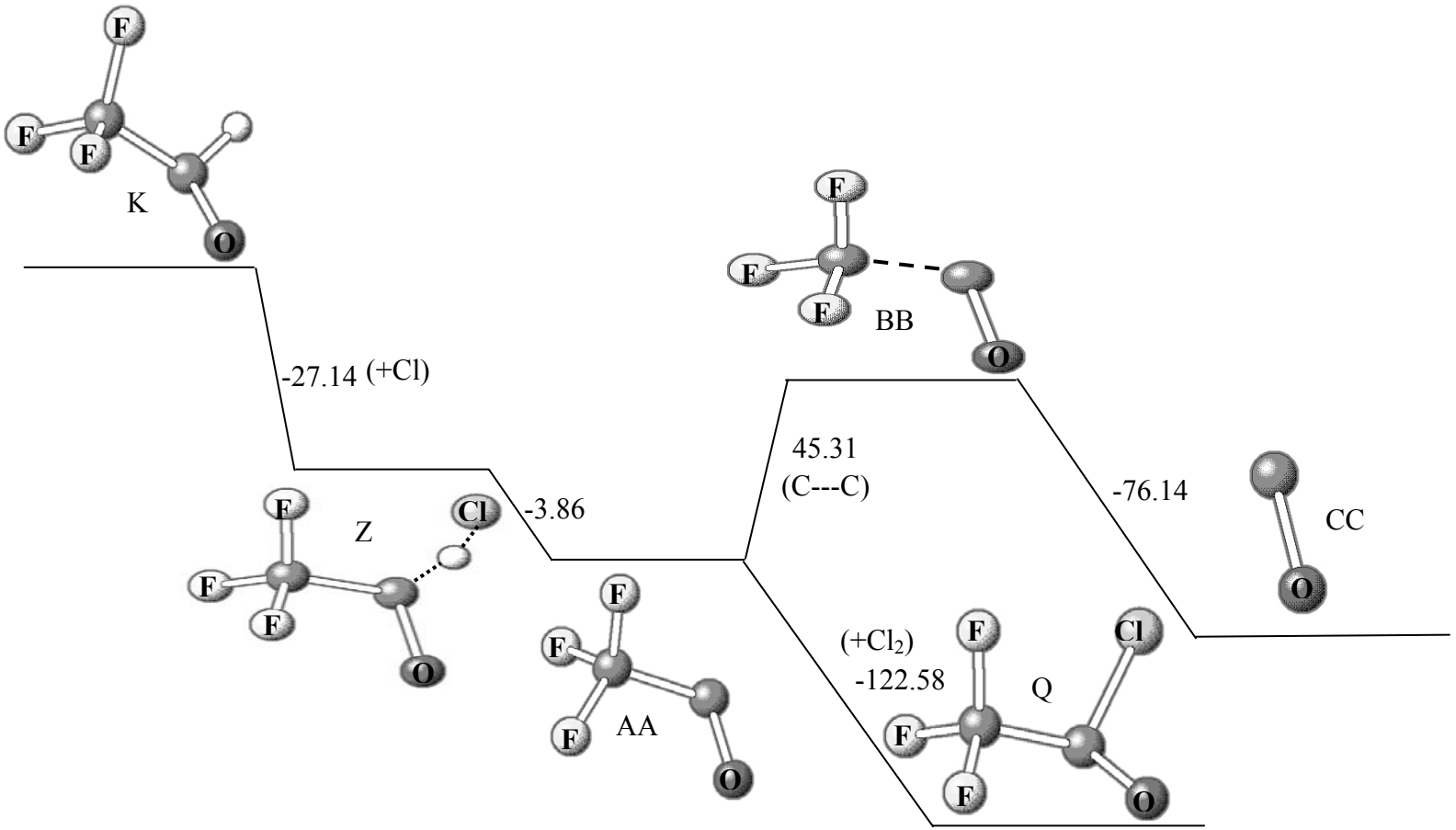

Figure 5.11 Reaction pathways, intermediates and transition states from CF_3CHO to CF_3CClO and CO computed at UB3LYP/6-31G(d) level of theory. Energy values are in kJ mol^{-1}

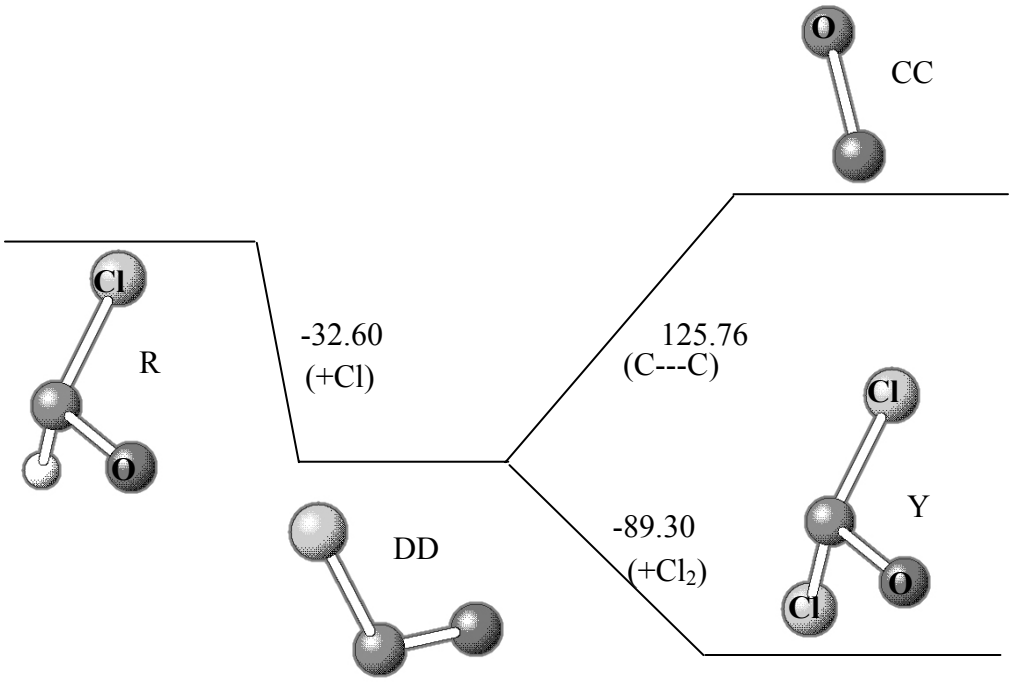

Figure 5.12 Reaction pathways, intermediates and transition states from HClCO to CCl_2O and CO computed at UB3LYP/6-31G(d) level of theory. Energy values are in kJ mol^{-1}

(a)

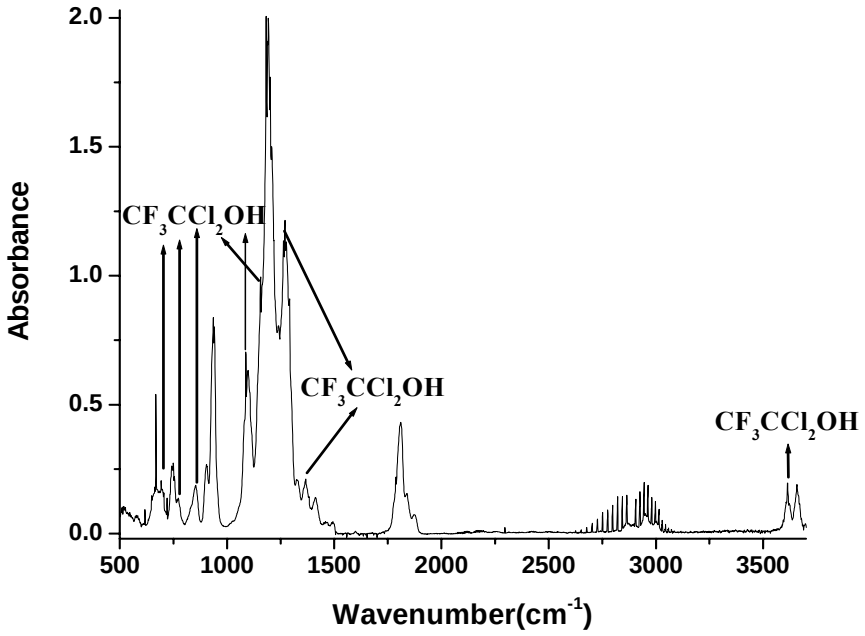

(b)

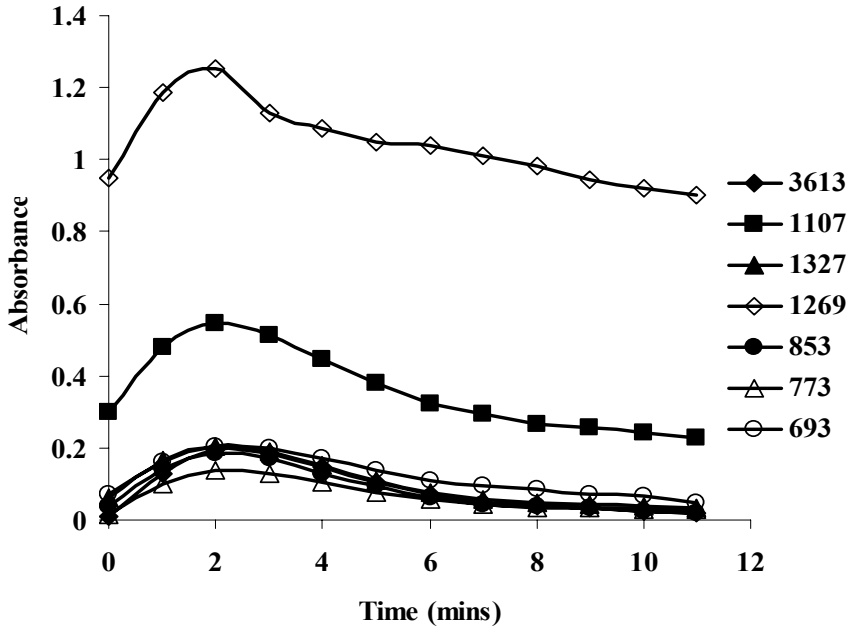

Figure 5.13 (a) IR spectrum of an intermediate alcohol species tentatively assigned to CF_3CCl_2OH. (b) Absorbance changes of the seven vibrational bands (cm^{-1}) against time

Reference

1. C. W. Spicer, E. G. Chapman, B. J. Finlayson-Pitts, R. A. Plastridge, J. M. Hubbe, J. D. Fast and C. M. Berkowitz, Nature, 394, 353, 1998

2. K. W. Oum, M. J. Lakin, D. O. Dehaan, T. Brauers and B. J. Finlayson-Pitts, Science, 279, 74, 1998

3. A. Sekiya and S. Misaki, Proceedings of the International Conference on Ozone Protection Technologies, Baltimore, Maryland, 12-13, Novermber, p26, 1997

4. K. G. Kambanis, Y. G. Lazarou and P. Papagiannakopoulos, Air Pollution research report 66, "Polar Stratospheric Ozone 1997"; European Commission: Belgium, p557, 1998

5. R. Atkinston, J. Phys. Chem. Reference data, Washington, DC, 1, 1994

6. V. C. Papadimitriou, A. V. Prosmitis, Y. G. Lazarou and P. Papagiannakopoulos, J. Phys. Chem. A, 107, 3733, 2003

7. S. R. Sellevåg, C. J. Nielsen, O. A. Søvde, G. Myhre, J. K. Sundet, F. Stordal and I. S. A. Isaksen, Atmos. Environ., 38, 6725, 2004

8. S. P. Li, T. S. Chwee, W.Y. Fan, J. Phys. Chem. A., 109, 11815, 2005

9. NIST Standard Reference Database No 69, March, 2003 Release at http://webbook.nist.gov/chemis

10. N. Washida, Bull. Chem. Soc. Jpn, 60, 3757, 1987

11. J. J. Rochford, L. J. Powell and R. Grice, J. Phys. Chem., 99, 15369, 1995

12. P. M. Sheaffer and P. F. Zittel, J. Phys. Chem. A, 104, 10194, 2000

13. S. R. Sellevåg, and C. J. Nielsen, Asian Chem. Lett., 7, 15, 2003

14. J. S. Francisco and I. H. Williams, Spectrochimi. Acta., 48A, 1115, 1992

15. G. S. Tyndall, T. J. Wallington, M. D. Harley and W. F. Schnelder, J. Phys. Chem., 97. 1576, 1993

16. P. W. Seakins, J. J. Orlando and G. S. Tyndall, Phys. Chem. Chem. Phys., 6, 2224, 2004

17. J. J. Orlando and G. S. Tyndall, Chem. Rev., 103, 4657, 2003

18. T. C. Clark, M. A. A. Clyne and D. H. Stedman, Trans. Faraday Soc., 62, 3354, 1966

19. G. K. Rollefson, J. Am. Chem. Soc., 55, 148, 1933

20. W. Lu, S. L. Chou, Y-P Lee, S. C. Xu, Z. F. Xu and M. C. Lin, J. Chem. Phys., 122, 244314, 2005

21. Horst-Henning Grotheer, F. L. Nesbitt and R. B. Klemm., J. Phys. Chem. 90, 2512, 1986

22. W. J. Debruyn, J. A. Shorter, P. Davidovits, D. R. Worsnop, M. S. Zahniser and C. E. Kolb, Environ. Sci. and Tech., 29, 1179, 1995